

---

# Development of a new method for the wave optical propagation of ultrashort pulses through linear optical systems

---

## Dissertation

for the acquisition of the academic title Doktor-Ingenieur (Dr.-Ing.)



---

seit 1558

Submitted to the Council of the Faculty of Physics and Astronomy of  
the Friedrich-Schiller-Universität Jena

**By: M.Sc. Norman Girma Worku**

Born in Waka, Ethiopia on 12.10.1989

**Gutachter:**

1. Prof. Dr. Herbert Gross, Friedrich–Schiller-Universität Jena
2. Prof. Dr. Alexander Szameit, Institute for Physics, University of Rostock
3. Dr. Francois Courvoisier, European Research Lab, Besancon, Femto-ST

Tag der Disputation: 10/12/2020

---

## Abstract

Many applications of ultrashort laser pulses require the manipulation and control of the pulse parameters by using pulse shaping systems. The design and simulation of such optical systems usually require pulse propagation methods which take the combined effects of dispersion, diffraction, and system aberrations into account. In the conventional pulse propagation methods based on the spectrum of plane wave (using the Fourier transform), usually large number of sampling points are needed for the correct Fourier transform operations due to the fast oscillating phase of the complex pulse field. In this work, I have developed an alternative pulse propagation method, based on the Gaussian pulsed beam decomposition, as an extension of the monochromatic Gaussian beam propagation method. Systematic methods for the decomposition of an input pulse, with arbitrary spatial and temporal (spectral) profiles, into a set of elementary Gaussian pulsed beams are proposed. Algorithms for computing the spatio-temporal and spatio-spectral profiles of the propagated pulse as the phase correct superposition of individual Gaussian pulsed beams are developed. The proposed decomposition method allows the elementary Gaussian pulsed beams to have different parameters depending on the local spatial and spectral phase of the given input pulse which reduces the number of Gaussian pulsed beams required to decompose an input pulsed beam with a given accuracy.

Accurate modeling of sharp edge diffraction of the field after hard aperture is not possible with the conventional Gaussian beam decomposition method. To overcome this limitation, a new kind of beam called the truncated Gaussian beam, is introduced and systematically combined with the conventional Gaussian beam decomposition method. The analytical propagation equation of the truncated Gaussian beam through any paraxial optical system is derived. Similarly, for an accurate decomposition and propagation of pulse fields after hard apertures, a new kind of pulsed beam called the spatially truncated Gaussian pulsed beam is defined and combined with the Gaussian pulsed beam decomposition method. Additionally, the application of the Gaussian beam decomposition method is extended to handle the propagation of vectorial fields through optical systems by combining with the three-dimensional polarization ray-tracing calculus. Several example calculations are presented to validate the proposed methods and show their application in propagating fields through optical systems which are rather complicated to model using the conventional methods.

This page is left blank intentionally.

## Zusammenfassung

Viele Anwendungen von ultrakurzen Laserpulsen erfordern die Manipulation und Steuerung der Pulsparameter unter Verwendung von Pulsformungssystemen. Der Entwurf und die Simulation solcher optischer Systeme erfordern üblicherweise Propagationmethoden für Pulse, die die kombinierten Effekte von Dispersion, Beugung und Systemaberrationen berücksichtigen. Bei den herkömmlichen Ausbreitungsverfahren für Pulse, die auf dem Spektrum der ebenen Welle basieren (unter Verwendung der Fourier-Transformation), wird aufgrund der schnell oszillierenden Phase des komplexen Impulsfeldes normalerweise eine große Anzahl von Abtastpunkten für die korrekten Fourier-Transformationsoperationen benötigt. In dieser Arbeit wird eine alternative Pulsausbreitungsmethode entwickelt, die auf der gepulsten Gaußstrahlzerlegung basiert, als Erweiterung der monochromatischen Gaußstrahlpropagationmethode. Es werden systematische Verfahren zur Zerlegung eines Eingangspulses mit beliebigen räumlichen und zeitlichen (spektralen) Profilen mit einem Satz elementarer gepulster Gaußstrahlen vorgestellt. Es werden Algorithmen zur Berechnung der räumlich-zeitlichen und räumlich-spektralen Profile des ausgebreiteten Impulses als phasenkorrekte Überlagerung einzelner gepulster Gaußstrahlen entwickelt. Das vorgeschlagene Zerlegungsverfahren ermöglicht es den elementaren gepulsten Gaußstrahlen, abhängig von der lokalen räumlichen und spektralen Phase des gegebenen Eingangsimpulses unterschiedliche Parameter zu haben, wodurch die erforderliche Anzahl der gepulsten Gaußstrahlen verringert wird, um ein Eingangsimpulsfeld mit einer gegebenen Genauigkeit zu zerlegen.

Eine genaue Modellierung der scharfen Kantenbeugung des Feldes nach einer harten Apertur ist mit der herkömmlichen Gaußstrahlzerlegungsmethode nicht möglich. Um diese Einschränkung zu überwinden, wird eine neue Art von Strahl eingeführt, der als abgeschnittener Gaußstrahl bezeichnet wird. Dieser wird systematisch mit der herkömmlichen Gaußstrahlzerlegungsmethode kombiniert. Die analytische Ausbreitungsgleichung des abgeschnittenen Gaußstrahls durch ein beliebiges paraxiales optisches System wird hergeleitet. In ähnlicher Weise wird für eine genaue Zerlegung und Ausbreitung von Impulsfeldern nach harten Aperturen eine neue Art von gepulsten Strahlen definiert, die als räumlich abgeschnittene gepulste Gaußstrahlen bezeichnet werden, und mit dem gepulsten Zerlegungsverfahren kombiniert. Zusätzlich wird die Anwendung des Gaußstrahlzerlegungsverfahrens durch Kombination mit der dreidimensionalen Rechnung für polarisierte Strahlen erweitert, um die Propagation von

Vektorfeldern durch optische Systeme zu ermöglichen. Es werden mehrere Beispielmrechnungen vorgestellt, um die vorgeschlagenen Methoden zu validieren und deren Anwendung bei der Ausbreitung von Feldern durch optische Systeme, deren Modellierung mit herkömmlichen Methoden kompliziert ist, zu zeigen.

# Contents

<b>Abstract</b>	<b>i</b>
<b>Zusammenfassung</b>	<b>iii</b>
<b>Contents</b>	<b>1</b>
<b>1 Motivation</b>	<b>3</b>
<b>2 Theory and State of the Art Methods</b>	<b>7</b>
2.1 Ultrashort pulse . . . . .	7
2.2 Pulsed beam . . . . .	10
2.3 Methods of propagating scalar pulse fields . . . . .	11
2.3.1 Ray tracing . . . . .	12
2.3.2 Generalized paraxial wave propagation . . . . .	13
2.3.3 Temporal Fourier transform based methods . . . . .	22
2.4 Propagation of vectorial fields . . . . .	29
2.4.1 Three dimensional (3D) polarization ray tracing . . . . .	29
2.4.2 Vectorial diffraction for high NA focusing . . . . .	31
<b>3 New Extensions to the Gaussian Beam Decomposition Method</b>	<b>33</b>
3.1 Curved wavefront decomposition . . . . .	33
3.2 Extension to ultrashort pulse propagation . . . . .	37
3.2.1 Decomposition of arbitrary spectral profile . . . . .	37
3.2.2 Gaussian pulsed beam decomposition . . . . .	39
3.2.3 The concept of group path length . . . . .	41
3.2.4 Modeling of ideal diffraction grating . . . . .	42
3.2.5 Spatio-temporal coupling in free space propagation . . . . .	44
3.2.6 Spatio-temporal and spatio-spectral detectors . . . . .	45
3.3 Propagation of field after hard aperture . . . . .	49
3.3.1 Truncated Gaussian beams . . . . .	49
3.3.2 Decomposition of a field after hard aperture . . . . .	51
3.3.3 Spatially truncated Gaussian pulsed beams . . . . .	53
3.4 Extension to vectorial field propagation . . . . .	55
<b>4 Validations and Application Examples</b>	<b>57</b>
4.1 Monochromatic beam propagation . . . . .	57
4.1.1 Propagation of single truncated Gaussian beam . . . . .	57
4.1.2 Fresnel diffraction of the field after a hard aperture . . . . .	59
4.1.3 Converging spherical wavefront after circular aperture . . . . .	62

---

4.1.4	Propagation of field with non-spherical wavefronts . . . . .	65
4.1.5	Vectorial field propagation in a high NA focusing . . . . .	69
4.2	Ultrashort pulse propagation . . . . .	70
4.2.1	Spatio-temporal coupling of Gaussian pulsed beam in free space	71
4.2.2	Propagation of spatially truncated Gaussian pulsed beam . . .	72
4.2.3	Gaussian pulse decomposition of spectral profile with a large TOD	74
4.2.4	Propagation of ultrashort pulse after circular aperture . . . . .	76
4.2.5	Pulse focusing using an aspheric lens . . . . .	78
4.2.6	Bessel-X pulse after an axicon . . . . .	81
4.2.7	Ultrashort pulse shaping using diffraction gratings . . . . .	84
4.3	Further discussions . . . . .	95
<b>5</b>	<b>Conclusion and Outlook</b>	<b>98</b>
	<b>Bibliography</b>	<b>101</b>
	<b>Appendices</b>	<b>111</b>
<b>A</b>	<b>Derivation of the generalized paraxial wave equation</b>	<b>111</b>
<b>B</b>	<b>Derivation of the generalized spatio-temporal Huygens integral</b>	<b>114</b>
<b>C</b>	<b>Propagation equations for full Gaussian (pulsed) beam</b>	<b>116</b>
C.1	Derivation of propagation formula for a monochromatic Gaussian beam	116
C.2	Derivation of the propagation formula of a Gaussian pulsed beam . . .	117
<b>D</b>	<b>Propagation equations for the truncated Gaussian (pulsed) beam</b>	<b>119</b>
D.1	Derivation of the propagation formula of a truncated Gaussian beam .	119
D.2	Derivation of the propagation formula of a spatially truncated Gaussian pulsed beam . . . . .	122
<b>E</b>	<b>Sampling schemes for the Gaussian beam centers</b>	<b>125</b>
	<b>List of Figures</b>	<b>126</b>
	<b>List of Abberevations</b>	<b>134</b>
	<b>Acknowledgment</b>	<b>135</b>
	<b>Ehrenwörtliche Erklärung</b>	<b>137</b>
	<b>Curriculum Vitae</b>	<b>139</b>
	<b>Publications</b>	<b>141</b>



# 1. Motivation

The history of studying the nature and applications of light by humans, which laid the foundation for modern optics, goes back to the era of Greeks in 5th B.C. to 3rd B.C based on the natural light sources [1]. Since then numerous artificial light sources, including the electrical ones in the beginning of 19<sup>th</sup> century [2], have been invented and their control mechanisms and application areas have been diversified. The development of Laser in the 20<sup>th</sup> century marked a decisive breakthrough in the field of optics and has led to the development of systems and mechanisms of using light for several scientific and industrial applications such as imaging, material processing, metrology and optical communication just to mention a few [3]. Nowadays there are commercially available ultrafast laser sources that produce ultrashort pulses having a duration in the ranges of femtosecond ( $10^{-15}sec$ ) to picoseconds ( $10^{-12}sec$ ) and hence have broad-frequency bandwidth. The extremely short duration of ultrashort pulse makes it very crucial for experiments that require high time resolution such as excitation and measurement of ultrafast processes in chemical and biological materials [4, 5]. The high-bandwidth feature of the ultrashort pulse makes it attractive in the areas of optical communications for high fiber-optic transmission rates, in the order of terabit/sec ( $10^{12}bit/sec$ ), and wavelength-division-multiplexing (WDM) systems [4]. With further amplification and focusing, the ultrashort pulses can be used to obtain ultrahigh peak power, up to the order of petawatt ( $10^{15}W$ ) and hence ultrahigh peak intensities up to the order of  $10^{30}W/cm^2$  at moderate energy levels. These extremely powerful and intense light bullets, which also have short interaction times, are used in high-quality material processing such as cutting and drilling in industrial applications [4, 6].

Different scientific and industrial applications of ultrashort laser pulses usually involve manipulation and control of the pulse properties by propagating through different optical components [6, 7]. The effect of a real optical system on the ultrashort pulse is usually complicated due to the combined effects of dispersion, diffraction, spatio-temporal distortions, and the system aberrations [8]. The design and simulation of such optical systems generally require numerical modeling tools, beyond the simple analytical formulas, which enable simulation of the propagation of a given ultrashort pulse through a real non-paraxial optical systems taking the effects of dispersion, diffraction, spatio-temporal distortion and the system aberrations into account.

Most previous studies in the numerical simulations of the wave optical propagation of ultrashort pulses through optical systems are based on the conventional concept of representing an optical pulse as a weighted superposition of its spectral components using the temporal Fourier transform (FT). Each spectral component is then propagated independently through the optical system to the target plane where an inverse Fourier transform (IFT) is used to get the temporal profile of the propagated pulse [8–11]. One of the main challenges for the practical application of this approach is the number of spectral components required for appropriate sampling of the ultrashort pulse [12]. For the correct computation of the temporal FT and its inverse, the number of spectral components used must be sufficient to sample the spectral amplitudes and phases both in the initial and final planes [13]. The spectral amplitude profile is usually a smooth function of frequency however, the spectral phase is a fast oscillating function as it is numerically stored in  $2\pi$  modulo [9, 13]. Therefore, a huge number of spectral samples are required if the input pulse has a strongly curved spectral phase or the optical system through which it propagates has large dispersion or spatio-temporal distortion.

For the wave optical propagation of each monochromatic spectral component through the given optical systems, a hybrid diffraction modeling is usually used [8,10,14]. In the hybrid diffraction modeling, ray tracing is used to compute the spectral complex fields at the exit pupil and a diffraction integral is used to propagate to the focal plane of an optical system [8]. However, the application of such a simple hybrid diffraction method is used to compute the final field only in the close vicinity of the focal plane and requires a well-defined exit pupil, negligible diffraction until the exit pupil and small phase aberration [8, 15]. The more general approach is to propagate the field through different components of the system using different techniques, such as the angular spectrum method for homogeneous medium and geometrical ray tracing for real curved optical surfaces [9,10]. However, this requires frequent switching between geometrical rays and the complex electric fields which is computationally intensive for systems with multiple components. In addition to that, a large number of sampling points are required for the spatial FT used in the angular spectrum method for propagating intermediate fields with large aberration. As most ultrashort pulse shaping systems have generally tilted and decentered components, the computation of the fields on the tilted planes is usually unavoidable which adds up on the computational complexity [16–18]. Hence, with the angular spectrum of plane-wave methods, the propagation of even the individual monochromatic component of the pulse becomes very challenging and numerical

intensive for systems with large aberration and systems containing components such as axicons, tilted prisms and gratings.

As an alternative method of the system diffraction calculation, the Gaussian beam decomposition (GBD) method has been proposed for the wave optical propagation of monochromatic fields through real optical systems [19, 20]. In the GBD method, Gaussian beams (GBs) are used as the elementary field for the decomposition instead of the plane waves in the angular spectrum method. Each elementary GB is propagated along its central ray paraxially using the analytical propagation methods. The combination of multiple spatially distributed and partially overlapping GBs allows modeling of the propagation of an electric field through non-paraxial optical systems with aberration [20, 21]. Unlike the angular spectrum of plane wave-based methods, the GBD method allows diffraction propagation through both homogenous medium and real curved interfaces, in an end-to-end manner, without switching to other methods. It also allows for the direct computation of the final complex field in any arbitrary point, including tilted and even curved analysis surfaces, throughout the system by superposition of individual GB contributions. Although the GBD method has been incorporated as the diffraction propagation method in some commercial optical system design computer programs [22–24], there are only a few published researches regarding the method. This has left room for several possible extensions of the conventional GBD method.

The first extension point is regarding the decomposition of the initial field with an arbitrarily curved wavefront. In the literature, the Gabor expansion method is widely used to decomposes the complex field in a given plane into a set of shifted and rotated GBs with flat wavefronts [25–27]. For the decomposition of a field with a curved wavefront, a large number of GBs are required in the Gabor expansion method to decompose the fast oscillating wrapped phase of the complex field in the initial plane. However, for the GBD method, it is not necessary to perform the decomposition on a single plane [19, 20]. The decomposition can be done directly on the curved wavefront surface without going to the complex field and hence avoiding the sampling of the fast oscillating wrapped phase. Although this possibility has been briefly mentioned in [20], the detailed methodology has not been worked out and published to the best of my knowledge. Secondly, although the spatial GBD appears in the literature, its temporal analog, the Gaussian pulse decomposition (GPD), is surprisingly rarely discussed [28, 29]. Even those few published studies use a set of elementary wave groups with no

initial chirp to propagate plane wave pulses in a homogeneous medium only in the spectral domain. Hence, they cannot be used to perform the complete spatio-temporal propagation of arbitrary pulsed beams through general optical systems. To the best of my knowledge, the comprehensive extension of the GBD method for the spatio-temporal propagation of arbitrary ultrashort pulse through optical systems has not been published previously. Thirdly, the conventional GBD method cannot be used to accurately model the sharp edge diffraction for fields after a hard aperture [19–21]. This is because, in the GBD method, the sharp edges of the field after hard aperture are usually replaced by a rather smooth Gaussian edges during the decomposition [20]. The approximative methods proposed in the literature to increase the steepness of the amplitude profile near the aperture edge can not be used for the accurate modeling of the sharp edge diffraction [19–21]. Finally, the conventional GBD methods are usually discussed based on the scalar theory of diffraction. However, the scalar theory of diffraction is not valid for systems that significantly change the polarization states of the field such as the high numerical aperture focusing. To the best of my knowledge, the full vectorial extension of the GBD method based on the three-dimensional polarization ray-tracing calculus has not been addressed in the literature.

In this work I have developed several methods to extend the conventional GBD method and contribute to filling the scientific research gaps discussed above. The dissertation is organized as follows. In chapter 2, the theory of ultrashort pulse properties and the state of the art methods for its propagation through linear optical systems are presented. The conventional GBD method is discussed in more detail as it is the basis for the new extension methods developed in this work. In chapter 3, the new methods developed to extend the GBD method are discussed. First a method of decomposing an arbitrarily curved but smooth wavefront into a set of GBs with different initial curvatures and directions is discussed. Then the extension of the GBD method, known as the Gaussian pulsed beam decomposition (GPBD) method, to handle the propagation ultrashort pulses through optical systems is presented. Furthermore, a novel approach of extending the GBD and GPBD methods for an accurate modeling of the sharp edge diffraction of fields after a hard aperture is discussed. Lastly, the full vectorial extension of the GBD method by combining with the three-dimensional polarization ray-tracing calculus is presented. In chapter 4, several example calculations are given to validate and show the applications of the new proposed methods. Finally, in chapter 5 concluding remarks are given together with the future outlook of the project.

## 2. Theory and State of the Art Methods

### 2.1 Ultrashort pulse

Ultrashort pulse is a short electromagnetic wave packet with temporal duration in the range of picoseconds ( $10^{-12}s$ ) or femtoseconds ( $10^{-15}s$ ) or even attoseconds ( $10^{-18}s$ ). The extremely short temporal duration of the ultrashort pulse leads to its spread over a wide range of frequencies. This can be understood from the property of the FT, which states that the shorter it is in the time domain the broader it will be in the frequency domain and vice versa [30, 31]. Mathematically, ultrashort pulses are fully described by the space and time-dependent vectorial electric fields. However, for the sake of simplicity let's begin with the temporal description only ignoring the space and polarization dependence. The temporal dependence of the real pulse field, in scalar approximation, is given by [30, 32]

$$E_{\Re}(t) = \Re\{E(t)\} = \Re\{\psi(t) \exp\{i\omega_0 t\}\}, \quad (2.1.1)$$

where  $t$  is the time coordinate,  $\omega_0$  is the carrier angular frequency,  $E(t)$  is the complex pulse field,  $\Re\{\cdot\}$  is the real value operator and  $\psi(t)$  is the complex amplitude envelope function which is given by

$$\psi(t) = \sqrt{I(t)} \exp\{-i\phi(t)\}, \quad (2.1.2)$$

with  $I(t)$  and  $\phi(t)$  being the temporal intensity and phase of the pulse respectively. Hence, the pulse shape in the temporal domain is given by the magnitude of the complex envelope function  $\psi(t)$ . As realistic pulses have complicated shapes, simple standard waveforms such as Gaussian and squared hyperbolic secant envelopes are usually used in the literature to discuss pulse characteristics [30]. Graphically, the temporal amplitude, intensity and phase profiles of a simple Gaussian pulse (GP) with quadratic phase is shown in Fig. 2.1 An ultrashort pulse can be represented by specifying the temporal profile of the pulse (its shape, amplitude and width) and phase. The commonly used method for specifying the pulse width are the intensity full width half maximum (FWHM) and the full width at  $1/e^2$  intensity ( $2\sigma_t$ ) as shown in Fig. 2.1b. They give the distance between two diametrically opposite points at which the intensity profile  $|(E(t))|^2$  reaches half or the  $1/e^2$  of the maximum value, respectively.

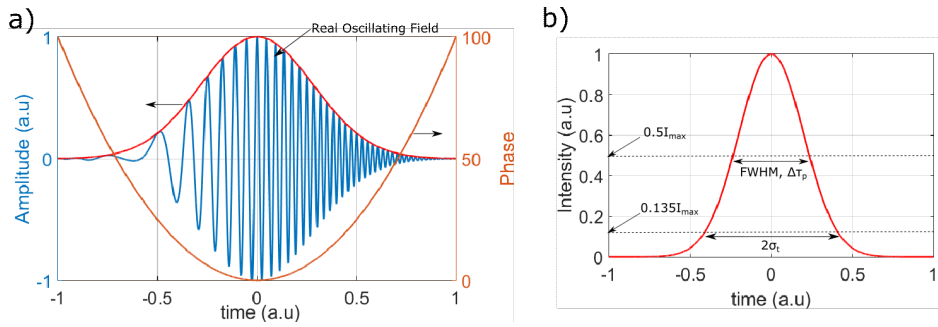


Figure 2.1: a) The amplitude envelope, the oscillating real field, and the phase profile of a Gaussian pulse with quadratic phase. b) The corresponding intensity profile.

The pulse field in the frequency domain is obtained by performing the temporal FT of the temporal field  $E(t)$  as

$$E(\omega) = \mathfrak{F}\{E(t)\} = \frac{1}{2\pi} \int_{-\infty}^{\infty} E(t) \exp\{-i\omega t\} dt, \quad (2.1.3)$$

where  $\omega$  is the angular frequency. The temporal IFT gives back the pulse field in temporal domain as

$$E(t) = \mathfrak{F}^{-1}\{E(\omega)\} = \int_{-\infty}^{\infty} E(\omega) \exp\{i\omega t\} d\omega \quad (2.1.4)$$

The physical interpretation of Eq. (2.1.4) is that the pulse field can be considered as a coherent superposition of plane waves with different frequencies. The pulse field in Fourier (spectral) domain can be expressed by

$$E(\omega) = \sqrt{S(\omega)} \exp\{-i\phi(\omega)\} \quad (2.1.5)$$

where  $S(\omega)$  is the spectral intensity and  $\phi(\omega)$  is the spectral phase. An ultrashort pulse can also be represented by specifying the spectrum of frequencies present in the pulse and the spectral phase [33].

Now let's consider the propagation of a pulse-field through a homogenous medium. The response of a dispersive medium to an electric field propagating through it, which is given the permittivity or the refractive index of the medium, depends on the frequency of the field. Hence, the wave number is also related to the frequency of the field by the relation known as the dispersion relation. The Taylor series expansion of the dispersion

relation is given by

$$k(\omega) = k_0 + \left. \frac{dk}{d\omega} \right|_{\omega_0} (\omega - \omega_0) + \frac{1}{2} \left. \frac{d^2k}{d\omega^2} \right|_{\omega_0} (\omega - \omega_0)^2 + \frac{1}{6} \left. \frac{d^3k}{d\omega^3} \right|_{\omega_0} (\omega - \omega_0)^3 + \dots \quad (2.1.6)$$

where  $k(\omega)$  is the frequency dependant wave number,  $\omega_0$  is the central angular frequency and  $k_0 = k(\omega_0)$ . The first few terms of the dispersion relation in Eq.( 2.1.6) have important physical meanings in the characteristics of electric field propagating through the material. The 1<sup>st</sup> term ( $k_0$ )is proportional to inverse of the phase velocity ( $V_{ph}$ ) of the field inside the medium which is given by

$$V_{ph} = \frac{c}{n(\omega_0)} = \frac{\omega_0}{k(\omega_0)} \propto \frac{1}{k_0}, \quad (2.1.7)$$

where  $c$  is the speed of light in vacuum and  $n(\omega_0)$  is the refractive index of the medium for the given central frequency  $\omega_0$ . The group velocity ( $V_g$ ) of the pulse envelope center is obtained from the inverse of the 2<sup>nd</sup> term in Eq. (2.1.6) by

$$V_g = \left( \left. \frac{\partial k}{\partial \omega} \right|_{\omega_0} \right)^{-1} = c \left( n(\omega_0) + \omega_0 \left. \frac{\partial n(\omega)}{\partial \omega} \right|_{\omega_0} \right)^{-1} = \frac{c}{n_g(\omega_0)} \quad (2.1.8)$$

where  $n_g(\omega_0)$  is the group index of the medium for the given central frequency  $\omega_0$ . In terms of wavelength, the group index of the medium is given by

$$n_g = \left( n(\omega_0) + \omega_0 \left. \frac{\partial n(\omega)}{\partial \omega} \right|_{\omega_0} \right) = \left( n(\lambda_0) - \lambda_0 \left. \frac{\partial n(\lambda)}{\partial \lambda} \right|_{\lambda_0} \right) \quad (2.1.9)$$

For materials with normal dispersion,

$$\frac{\partial n}{\partial \omega} > 0 \implies \frac{\partial n}{\partial \lambda} < 0 \implies n_g > n \text{ and } V_g < V_{ph}, \quad (2.1.10)$$

and for those with anomalous dispersion,

$$\frac{\partial n}{\partial \omega} < 0 \implies \frac{\partial n}{\partial \lambda} > 0 \implies n_g < n \text{ and } V_g > V_{ph}. \quad (2.1.11)$$

The 3<sup>rd</sup> term in the Taylor expansion of the dispersion relation in Eq. (2.1.6) gives the variation of the group velocity over frequency and hence called the group velocity

dispersion (GVD) of the medium which is given by

$$GVD = \left. \frac{\partial^2 k}{\partial \omega^2} \right|_{\omega_0} = \frac{\partial}{\partial \omega} \frac{1}{V_g} = \frac{\partial^2}{\partial \omega^2} \left( \frac{\omega n}{c} \right) = \frac{\lambda^3}{2\pi c^2} \frac{\partial^2 n}{\partial \lambda^2}. \quad (2.1.12)$$

For a pulse propagating through a medium with non-zero GVD, different spectral components will travel with different velocities and hence come out of the medium at different times. This results in the temporal dispersion (chirp) of the pulse. Depending on the sign of the material GVD, pulse through a given medium could be unchirped ( $GVD = 0$ ), up-chirped ( $GVD > 0$ ) or down-chirped ( $GVD < 0$ ) pulse [30,31].

## 2.2 Pulsed beam

Until this point the spatial property of the wave has been omitted. This is valid if the spatial profile is assumed to be an infinitely extended plane wave. However, in reality any wave exists in the form of a beam which has a finite spatial extension. As any beam can be decomposed into infinite number of plane waves each propagating in different directions, the methods discussed in section 2.1 are fully applicable for individual components after such decomposition. A pulsed beam is an electric field with finite extension in both spatial and temporal domains. If the temporal property is independent of the spatial coordinate of the pulsed beam, then the spatial and temporal components are separable. In such cases the pulsed beam is said to have no spatio-temporal coupling (STC) and its complete scalar electric field is given by

$$E(x, t) = E_x(x)E_t(t), \quad (2.2.1)$$

where  $E_x(x)$  is the spatial profile of the pulsed beam which does not vary with time, described in single spatial coordinate for simplicity, and  $E_t(t)$  is the temporal profile which is the same for all spatial coordinates. Applying the FTs (or inverses) with respect to appropriate variables, the electric field of pulsed beam in  $(x, t)$  domain can be represented in other three domains by

$$\begin{aligned} E(x, \omega) &= \mathfrak{F}_t\{E(x, t)\} = \frac{1}{2\pi} \int_{-\infty}^{\infty} E(x, t) \exp\{-i\omega t\} dt, \\ E(k, \omega) &= \mathfrak{F}_x\{E(x, \omega)\} = \frac{1}{2\pi} \int_{-\infty}^{\infty} E(x, \omega) \exp\{-ikx\} dx, \\ E(k, t) &= \mathfrak{F}_\omega^{-1}\{E(k, \omega)\} = \int_{-\infty}^{\infty} E(k, \omega) \exp\{i\omega t\} d\omega. \end{aligned} \quad (2.2.2)$$



In the absence of STC, the pulsed beam field is separable in all four domains. However, propagation of such pulsed beam through optical systems usually results in coupling of the spatial (angular) and the temporal (spectral) components of the pulsed beam [34]. For instance, consider propagation of pulsed beam through prism pair followed by dispersive medium as shown in Fig. 2.2. After the first dispersive prism, different

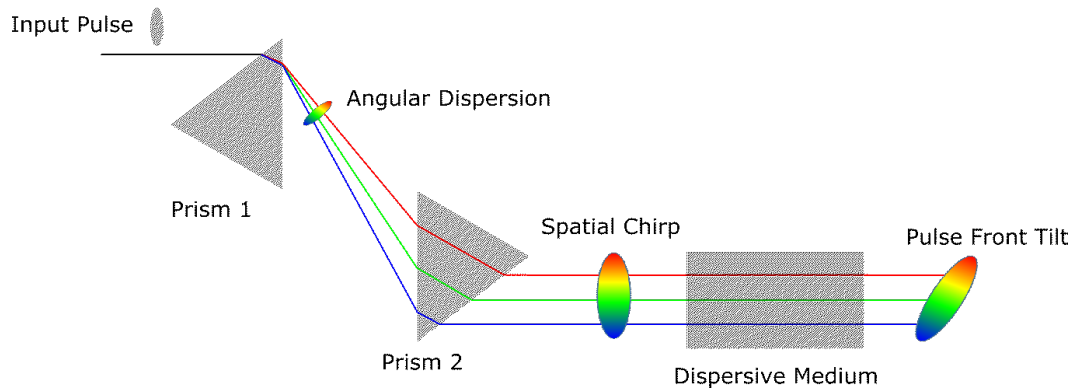


Figure 2.2: Demonstration of angular dispersion, spatial chirp and pulse front tilts of a pulse propagating through prism pair followed by dispersive medium.

frequency components leave the prism at different directions, resulting in the angular dispersion of the pulsed beam. If the second prism is used to remove the angular dispersion, then the resulting pulsed beam would have spatial chirp, where different spectral components are separated spatially. Propagating the spatially chirped pulsed beam through a dispersive medium results in a tilted pulse front as shown in Fig. 2.2 due to the spatial variation of the group velocity and hence the arrival time of the pulse. Although there are in total eight STCs, corresponding to the intensity and phase coupling in all of the four possible domains, only two of them are independent and all the others can be computed from the relations derived from the FT equations given in Eq.(2.2.2) [34–38]. The STCs are also known as spatio-temporal distortions.

## 2.3 Methods of propagating scalar pulse fields

Simulation of pulsed beam propagation through optical systems requires tools that take the dispersion and spatio-temporal distortion of the pulse into account in addition to the diffraction and system aberration of the individual spectral component of the pulse. In this work, only linear optical systems are assumed and the nonlinear propagation of ultrashort pulses is beyond its scope. The propagation of the electric field through linear optical systems is usually based on the principle of superposition. First the given pulsed beam field is decomposed into a set of monochromatic beams with different frequencies,

and each monochromatic beam is then propagated independently through the system. After the optical system, the final pulsed beam is computed by the superposition of the final fields of all monochromatic fields after the propagation. In this section, the current state of the art methods which are used for the propagation of ultrashort pulsed beams through linear optical systems are briefly discussed.

### 2.3.1 Ray tracing

Ray tracing is an extensively used tool for propagating light through optical systems based on the geometrical optics. In the geometrical optics, the Maxwell equations are reduced to the eikonal equation by assuming that the wavelength of light is negligibly small ( $\lambda \rightarrow 0$ ), which allows the representation of light with a pencil of rays [1]. Each ray is represented by a position in space and the unit vector pointing in the direction of its propagation. In the homogenous medium the rays travel in a straight line and at the interface between two different mediums they change their direction according to the geometric law of refraction/reflection [1, 39]. These basic laws of ray tracing can all be concluded from Fermat's principle which states that light rays travel along the path of least time [1]. The wavefront of a monochromatic beam after a given optical system, including the effects of aberration, can be computed by tracing several real rays through the system and taking the locus of points along each ray with equal total optical path length. The ray directions are perpendicular to the wavefront surface computed, which is also called the Malus-Dupin principle of the ray-wavefront equivalence [40, 41]. The validity of the ray-wavefront equivalence requires that the rays do not cross with each other [4, 42]. The intensity distribution of the output beam can be taken into account by considering the change in the ray density or the change in the area of the ray tube constructed from three or more neighboring rays [10].

For ultrashort pulses propagation, the geometrical ray tracing is widely used in computing the dispersion of the optical system by tracing rays with different wavelengths and computing the derivatives of the spectral phases with respect to the angular frequencies. In addition to that, by analyzing the positions and directions of rays with different wavelength, the spatio-spectral dispersions such as the spatial chirp and the angular dispersion of the system can be computed. Although the ray tracing is widely used in the design and simulation of optical systems, it cannot be used to model the diffraction effects. This is because in the geometrical optics the wavelength is assumed to be negligibly small and hence the wave nature of light is partly lost. In addition

to that, in the region where the rays cross with each other, for instance near the focal region of a lens with aberration, it is not possible to get a unique wavefront surface which is perpendicular to all rays. Therefore, to properly model the diffraction effects of light, for instance in the focal region of focusing system and after hard apertures, the physical optics based wave optical propagation methods should be used.

### 2.3.2 Generalized paraxial wave propagation

Most laser light sources produce light which has small divergence, as it has to travel back and forth several times between the oscillator mirrors without leaving the cavity [3]. The propagation of such low divergence beams in homogenous, isotropic medium can be computed by using the generalized paraxial wave equation or the generalized Huygens diffraction integral which are defined in the spatio-temporal domain [3, 5].

#### Generalized paraxial spatio-temporal wave equation

The generalized paraxial spatio-temporal wave equation is a differential equation which governs the propagation of paraxial pulsed beams through a homogenous, isotropic medium in the paraxial, the quadratic dispersion and the slowly varying envelope approximations [3, 5]. It can be derived from the angular spectrum of plane wave method by applying the corresponding approximations as detailed in Appendix A. The final generalized paraxial wave equation in the spatio-temporal domain is given by

$$i \frac{\partial \psi(x, y, \bar{t}; z)}{\partial z} + \left( \frac{1}{2k(\omega_0)} \Delta^{(2)} - \frac{D_0}{2} \frac{\partial^2}{\partial \bar{t}^2} \right) \psi(x, y, \bar{t}; z) = 0. \quad (2.3.1)$$

where  $\psi(x, y, \bar{t}; z)$  is the complex amplitude of the slowly varying envelope,  $\bar{t} = t - t_0$  is the time coordinate in the co-moving reference frame which travels with the group velocity of the pulse,  $t_0$  is the arrival time of the pulse group to given transversal plane,  $k(\omega_0)$  is the wave number in the medium at the central frequency  $\omega_0$ ,  $D_0 = \left. \frac{\partial^2 k}{\partial \omega^2} \right|_{\omega_0}$  is the GVD of the medium and  $\Delta^{(2)} = \left( \frac{\partial^2}{\partial x^2} + \frac{\partial^2}{\partial y^2} \right)$ . For the special cases of monochromatic beam (temporally invariant) and pulsed plane waves (spatially invariant), Eq. (2.3.1) reduces to the usual paraxial wave equation in Eq. (2.3.2) and the parabolic equation in Eq. (2.3.3), respectively [3, 5, 43]:

$$i \frac{\partial \psi(x, y; z)}{\partial z} + \frac{1}{2k(\omega_0)} \Delta^{(2)} \psi(x, y; z) = 0. \quad (2.3.2)$$

$$i \frac{\partial \psi(\bar{t}; z)}{\partial z} - \frac{D_0}{2} \frac{\partial^2}{\partial \bar{t}^2} \psi(\bar{t}; z) = 0. \quad (2.3.3)$$

Mathematically, it can be shown that a monochromatic fundamental Gaussian beam (GB) is one of the solutions of the time independent paraxial wave equation given in Eq. (2.3.2) [44, 45]. The electric field of a generalized non-rotationally symmetric GB in homogenous medium is given by

$$E_{\mathfrak{Re}}(\mathbf{r}; z) = \Re\{\psi(\mathbf{r}; z) \exp\{-ink_0 z\}\}, \quad (2.3.4)$$

with  $\psi(\mathbf{r}; z)$  is the Gaussian complex envelope given by <sup>1</sup>

$$\psi(\mathbf{r}; z) = \psi_0 \exp\left[-\frac{ik_0}{2} \mathbf{r}^T \mathbf{Q}^{-1} \mathbf{r}\right], \quad (2.3.5)$$

where  $\psi_0$  is the on-axis complex amplitude,  $k_0$  is the propagation constant in free space,  $\mathbf{r} = (x, y)$  is the spatial coordinate on the transversal plane located at  $z$  and  $\mathbf{Q}^{-1}$  is the  $2 \times 2$  complex curvature matrix,

$$\mathbf{Q}^{-1} = \begin{pmatrix} q_{xx}^{-1} & q_{xy}^{-1} \\ q_{yx}^{-1} & q_{yy}^{-1} \end{pmatrix}, \quad (2.3.6)$$

defining the beam parameters [44, 45]. The dependence of the Gaussian complex envelope on the refractive index of the medium is included in the complex curvature matrix of the GB. For simply astigmatic GBs, the complex matrix becomes a diagonal matrix with

$$q_{xx}^{-1} = \frac{1}{R_x(z)} - i \frac{\lambda_0}{\pi n \sigma_x(z)^2}, \quad q_{yy}^{-1} = \frac{1}{R_y(z)} - i \frac{\lambda_0}{\pi n \sigma_y(z)^2}, \quad \text{and} \quad q_{xy}^{-1} = q_{yx}^{-1} = 0, \quad (2.3.7)$$

where  $n$  is the refractive index of the medium,  $\sigma_x(z)$  and  $\sigma_y(z)$  are the half width (using the  $1/e$  amplitude width) of the GB and  $R_x(z)$  and  $R_y(z)$  are the radius of curvatures of the GB along x- and y-axis respectively in the transversal plane. For the generally astigmatic beam, the diagonal elements of the complex curvature matrix are non-zero and hence the orientation of the amplitude and phase ellipse are different [19].

Similarly, it can be shown that one possible solution of the quadratic equation in Eq.

---

<sup>1</sup>Unlike the expression in [44] and many other literature, here the normalization factor of  $1/\sqrt{|\mathbf{Q}^{-1}|}$  is not used for the complex envelope. This avoids the dependence of the peak amplitude of the initial GBs on the GB parameters which is helpful for the decomposition later in this work.

(2.3.3) is a Gaussian pulse (GP) which is given by [43]

$$E_{\Re}(t; z) = \Re \left[ \exp \left( i\omega_0 \frac{p_t^{-1} t^2}{2} \right) \exp \{i(\omega_0 t - nk_0 z)\} \right], \quad (2.3.8)$$

with  $p_t^{-1}$  being the temporal complex GP parameter which is defined by <sup>2</sup>

$$p_t^{-1} = \frac{1}{\omega_0} \left( S + i \frac{2}{\sigma_t(z)^2} \right), \quad (2.3.9)$$

where  $\omega_0$  is the central angular frequency,  $S = \Delta\omega/\Delta\bar{t}$  is the frequency sweep rate (equivalent to the linear chirp) and  $\sigma_t$  being the temporal  $1/e$  amplitude half width. Combining Eq. (2.3.8) and Eq. (2.3.4), a Gaussian pulsed beam (GPB) is obtained which is given by

$$E_{\Re}(\tilde{\mathbf{r}}; z) = \Re \{ \psi(\tilde{\mathbf{r}}; z) \exp \{-ink_0 z\} \}, \quad (2.3.10)$$

with  $\psi(\tilde{\mathbf{r}}; z)$  is the GPB complex envelope given by

$$\psi(\tilde{\mathbf{r}}; z) = \psi_0 \exp \left[ -\frac{ik_0}{2} \tilde{\mathbf{r}}^T \tilde{\mathbf{Q}}^{-1} \tilde{\mathbf{r}} \right], \quad (2.3.11)$$

where  $\psi_0$  is the on-axis complex amplitude,  $k_0$  is the propagation constant in free space,  $\tilde{\mathbf{r}}^T = (x, y, c\bar{t})$  is the spatio-temporal coordinate on the transversal plane located at  $z$  and  $\tilde{\mathbf{Q}}_{\tilde{\mathbf{r}}}^{-1}$  is the  $3 \times 3$  complex spatio-temporal curvature matrix given by [44]

$$\tilde{\mathbf{Q}}^{-1} = \begin{pmatrix} q_{xx}^{-1} & q_{xy}^{-1} & q_{xt}^{-1} \\ q_{yx}^{-1} & q_{yy}^{-1} & q_{yt}^{-1} \\ q_{tx}^{-1} & q_{ty}^{-1} & q_{tt}^{-1} \end{pmatrix}. \quad (2.3.12)$$

In Eq. (2.3.12), the terms  $q_{xx}^{-1}, q_{xy}^{-1}, q_{yx}^{-1}$  and  $q_{yy}^{-1}$  are the elements of the usual matrix of spatial complex curvatures including the x-y coupling terms, whereas  $q_{\tau\tau}^{-1}$  is the longitudinal(temporal) complex curvature given by

$$q_{tt}^{-1} = \frac{p_t^{-1}}{c} = \frac{1}{c\omega_0} \left( S + i \frac{2}{\sigma_t(z)^2} \right). \quad (2.3.13)$$

The remaining elements,  $(q_{x\tau}^{-1}, q_{y\tau}^{-1}, q_{\tau x}^{-1}$  and  $q_{\tau y}^{-1})$ , give the spatio-temporal coupling in the GPB [44]. The GPB is one possible solution of the generalized wave equation

---

<sup>2</sup>Since the  $1/e$  width of the amplitude profile is used here instead of the intensity profile, which was used in the original paper [43], the equation given here is slightly different from that in [43].

given in Eq. (2.3.1) and has Gaussian amplitude profiles and quadratic phases in both spatial and temporal domains. The GPB is usually propagated through paraxial optical systems by using the paraxial spatio-temporal matrix method as discussed below.

### Paraxial spatio-temporal matrix

The spatio-temporal matrix is an extension of the usual spatial ABCD matrix to include the first order temporal and spectral effects of the optical system. In 1990, Kostenbauder has reported one of the first comprehensive extension of the  $2 \times 2$  spatial ABCD matrix to  $4 \times 4$  spatio-temporal matrix [46]. That enabled the propagation of ultrashort pulses in paraxial approximation through rotationally symmetric or orthogonal and dispersive optical systems. The non-rotationally symmetric extension of the  $4 \times 4$  Kostenbauder matrix to a  $6 \times 6$  one was later reported by Lin [44]<sup>3</sup> and Marcus [47]. In this work I have selected the matrix formalism described by Lin [44] to propagate paraxial pulsed beams. This is because Lin has overcome the bad numerical conditioning of the matrix, due to extremely small temporal and extremely large frequency quantities, by scaling and normalizing the time and frequency coordinates [44]. In addition to that, it makes the derivation of the propagation equations for GPBs completely analogous with that of the spatial GBs [48, 49].

The first step in computing the Lin matrix of a system is to fix the reference optical axis from the initial to the final plane along the path of a transform limited GPB propagating through the system as shown in Fig. 2.3. The central ray of the GPB which propagates with the group velocity through the optical system is referred to as the pulsed ray. At each point along the reference pulsed ray, transversal planes are erected perpendicular to the ray direction. The frequency  $f_0$ , the arrival time  $t_0$  and the intersection points of the pulsed ray at each transversal plane are used as the reference frequency, the origin of the local temporal and the local spatial coordinate for the pulsed beam, respectively. Any other transform limited paraxial pulsed beam is represented by a ray pulse vector which is given by

$$\mathbf{P} = \left( x \quad y \quad c\bar{t} \quad n\theta_x \quad n\theta_y \quad -\bar{f}/f_0 \right)^T \quad (2.3.14)$$

where  $c$  is the speed of light in vacuum,  $n$  is the refractive index of the medium,  $[x, y]$  and  $[\theta_x, \theta_y]$  are the positions and the slopes of the pulsed ray in the local coordinate

---

<sup>3</sup>In [44] the extended  $6 \times 6$  method was published under arguably a "misleading" title and hence has got low attention in the scientific community.

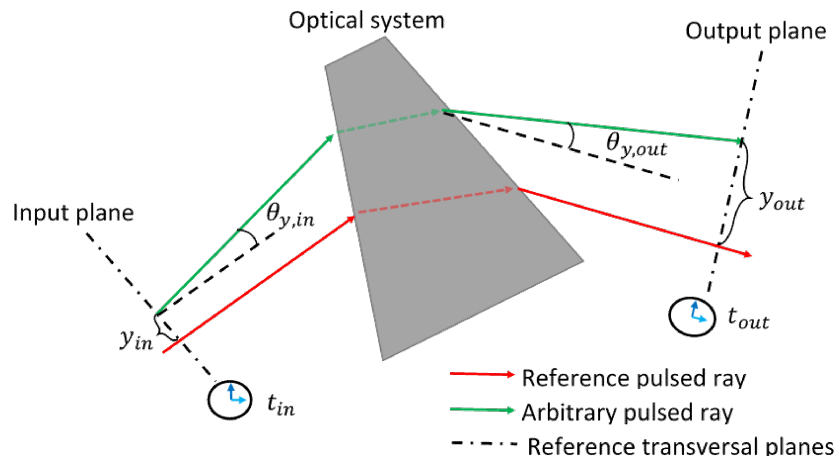


Figure 2.3: Schematic diagram showing the ray pulse parameters of a given optical system.

system on the transversal reference plane, respectively. The parameters  $\bar{t} = t - t_0$  and  $\bar{f} = f - f_0$  are the changes in the arrival time and carrier frequency of the given pulsed ray with respect to the reference pulsed ray, respectively. As the ray pulse vector elements are calculated with respect to the central ray on a transversal plane, the tilt and decenter effects are already included by the real ray tracing of the central ray.

In the first order approximation, the parameters of the ray pulse vector at the output of a paraxial dispersive optical system are linearly related to that at the input by

$$\begin{pmatrix} \tilde{\mathbf{r}}_2 \\ \tilde{\mathbf{v}}_2 \end{pmatrix} = \underbrace{\begin{pmatrix} \tilde{\mathbf{A}} & \tilde{\mathbf{B}} \\ \tilde{\mathbf{C}} & \tilde{\mathbf{D}} \end{pmatrix}}_{\tilde{\mathbf{L}}} \begin{pmatrix} \tilde{\mathbf{r}}_1 \\ \tilde{\mathbf{v}}_1 \end{pmatrix} \quad (2.3.15)$$

where  $\tilde{\mathbf{r}} = (x \ y \ c\bar{t})^T$ ,  $\tilde{\mathbf{v}} = (n\theta_x \ n\theta_y \ -\bar{f}/f_0)^T$  and  $\tilde{\mathbf{L}}$  is the Lin matrix of the system<sup>4</sup>. All elements of vectors  $\tilde{\mathbf{r}}$  have the units of length and that of vector  $\tilde{\mathbf{v}}$  are dimensionless [44]. Each of the four elements of the Lin matrix are by themselves  $3 \times 3$  matrices which are defined by the first order partial derivatives of the ray pulse parameter vectors as

$$\tilde{\mathbf{A}} = \frac{\partial \tilde{\mathbf{r}}_2}{\partial \tilde{\mathbf{r}}_1}, \quad \tilde{\mathbf{B}} = \frac{\partial \tilde{\mathbf{r}}_2}{\partial \tilde{\mathbf{v}}_1}, \quad \tilde{\mathbf{C}} = \frac{\partial \tilde{\mathbf{v}}_2}{\partial \tilde{\mathbf{r}}_1} \quad \text{and} \quad \tilde{\mathbf{D}} = \frac{\partial \tilde{\mathbf{v}}_2}{\partial \tilde{\mathbf{v}}_1}. \quad (2.3.16)$$

Expanding the vectors in Eq. (2.3.16) in terms of the individual elements of the ray

<sup>4</sup>Note that the tilde symbol is added over all parameters to indicate that the spatio-temporal and distinguish from the conventional spatial matrix method.

pulse vector, and combining the four matrices, the complete  $6 \times 6$  Lin matrix becomes

$$\tilde{\mathbf{L}} = \left[ \begin{array}{ccc|ccc} \frac{\partial x_2}{\partial x_1} & \frac{\partial x_2}{\partial y_1} & \frac{1}{c} \frac{\partial x_2}{\partial t_1} & \frac{1}{n_1} \frac{\partial x_2}{\partial \theta_{x1}} & \frac{1}{n_1} \frac{\partial x_2}{\partial \theta_{y1}} & -f_0 \frac{\partial x_2}{\partial f_1} \\ \frac{\partial y_2}{\partial x_1} & \frac{\partial y_2}{\partial y_1} & \frac{1}{c} \frac{\partial y_2}{\partial t_1} & \frac{1}{n_1} \frac{\partial y_2}{\partial \theta_{x1}} & \frac{1}{n_1} \frac{\partial y_2}{\partial \theta_{y1}} & -f_0 \frac{\partial y_2}{\partial f_1} \\ \frac{\partial t_2}{\partial x_1} & \frac{\partial t_2}{\partial y_1} & \frac{\partial t_2}{\partial t_1} & \frac{c}{n_1} \frac{\partial t_2}{\partial \theta_{x1}} & \frac{c}{n_1} \frac{\partial t_2}{\partial \theta_{y1}} & -cf_0 \frac{\partial t_2}{\partial f_1} \\ \hline n_2 \frac{\partial \theta_{x2}}{\partial x_1} & n_2 \frac{\partial \theta_{x2}}{\partial y_1} & \frac{n_2}{c} \frac{\partial \theta_{x2}}{\partial t_1} & \frac{n_2}{n_1} \frac{\partial \theta_{x2}}{\partial \theta_{x1}} & \frac{n_2}{n_1} \frac{\partial \theta_{x2}}{\partial \theta_{y1}} & -n_2 f_0 \frac{\partial \theta_{x2}}{\partial f_1} \\ n_2 \frac{\partial \theta_{y2}}{\partial x_1} & n_2 \frac{\partial \theta_{y2}}{\partial y_1} & \frac{n_2}{c} \frac{\partial \theta_{y2}}{\partial t_1} & \frac{n_2}{n_1} \frac{\partial \theta_{y2}}{\partial \theta_{x1}} & \frac{n_2}{n_1} \frac{\partial \theta_{y2}}{\partial \theta_{y1}} & -n_2 f_0 \frac{\partial \theta_{y2}}{\partial f_1} \\ -\frac{1}{f_0} \frac{\partial f_2}{\partial x_1} & -\frac{1}{f_0} \frac{\partial f_2}{\partial y_1} & -\frac{c}{f_0} \frac{\partial f_2}{\partial t_1} & -\frac{1}{f_0} \frac{c}{n_1} \frac{\partial f_2}{\partial \theta_{x1}} & -\frac{1}{f_0} \frac{c}{n_1} \frac{\partial f_2}{\partial \theta_{y1}} & \frac{\partial f_2}{\partial f_1} \end{array} \right] \quad (2.3.17)$$

As in the case of conventional ABCD matrix algorithm, the total Lin matrix for a general sequence of surfaces or optical components is computed by multiplying that of each surfaces/component of the sequence in reverse order [30, 44, 50] as

$$\tilde{\mathbf{L}}_{Total} = \tilde{\mathbf{L}}_N \tilde{\mathbf{L}}_{N-1} \tilde{\mathbf{L}}_{N-2} \dots \tilde{\mathbf{L}}_1, \quad (2.3.18)$$

where  $\tilde{\mathbf{L}}_{Total}$  is the total Lin matrix for sequence of components,  $\tilde{\mathbf{L}}_1, \tilde{\mathbf{L}}_2, \dots, \tilde{\mathbf{L}}_N$  are the Lin matrices for individual components indexed 1,2,...,N.

The analytical formulas for the Lin matrices for simple optical components such as homogenous dispersive slab, ideal lens/mirror, grating, and the spherical surface can be obtained from the literature [44, 46]. However, the derivation of analytical formulae for the refraction/reflection from a general tilted and decentered optical components and general non-spherical surfaces is not trivial. Therefore, for the general case I have used a method based on the numerical differential ray tracing to compute the partial derivatives in the elements of the Lin matrix of the complete system. For a given central ray, local coordinate systems are setup before and after a given optical system as shown in Fig. 2.3. Then five parabal rays, each with a slightly different position (in x and y), slope (in x and y), and frequency from the central ray, are defined on the input transversal plane. By tracing the parabal rays through the system, the ray pulse parameters are computed at the output transversal plane. Finally the partial differentials in the Lin matrix are computed by taking the ratios of the



output ray pulse parameters to the input ray pulse parameters. As the frequency remains unchanged through the system  $f_{out} = f_{in}$ , the first-order spatial chirp, first-order angular dispersion, and the group delay dispersions can be obtained from the last column of the Lin matrix [44, 46].

### Generalized spatio-temporal Huygens diffraction integral

The generalized paraxial wave equations in Eq. (2.3.1) can be used to propagate paraxial pulsed beams in a homogenous, isotropic medium. However, it is not suitable for the propagation through optical systems containing different components, where an alternative approach, called the generalized spatio-temporal Huygens diffraction integral is usually used [3, 5]. Like the monochromatic Huygens diffraction integral, the generalized spatio-temporal Huygens diffraction integral is derived from the Kirchoff integral equation by applying the Fresnel approximation as detailed in Appendix B. The final expression for the generalized spatio-temporal Huygens integral in paraxial approximation for optical system with linear chirp is given by

$$\psi_2(\mathbf{r}_2, t_2) = \zeta \iiint \psi_1(\mathbf{r}_1, t_1) \exp \left[ -i \frac{k_0}{2} \underbrace{\left( n_2 \boldsymbol{\theta}_2^T \mathbf{r}_2 - n_1 \boldsymbol{\theta}_1^T \mathbf{r}_1 - \frac{\bar{f}_2}{f_0} c \bar{t}_2 + \frac{\bar{f}_1}{f_0} c \bar{t}_1 \right)}_{\Phi} \right] d\mathbf{r}_1 dt_1, \quad (2.3.19)$$

where  $\zeta$  is a constant,  $\psi_i(\mathbf{r}_i, t_i)$  is the reduced complex amplitudes of the field,  $n_i$  are the refractive indices, ( $\boldsymbol{\theta}_i = (\theta_{x_i}, \theta_{y_i}), \mathbf{r}_i = (x_i, y_i), \bar{f}_i/f_0$  and  $c\bar{t}_i$ ) are the elements of the ray-pulse vector on the initial and final transversal planes for  $i = 1$  and  $i = 2$  respectively. The spatio-temporal Huygens integral is fully equivalent and represent the same mathematical and physical approximations as the generalized paraxial wave equation.

### Paraxial wave optical propagation using Lin matrix

From the ray pulse vector transformation using the Lin matrix given in Eq. (2.3.15), the input and output spatio-temporal frequencies are related to the input and output spatio-temporal coordinates by [49]

$$\begin{pmatrix} \tilde{\nu}_1 \\ \tilde{\nu}_2 \end{pmatrix} = \underbrace{\begin{pmatrix} n_1 \tilde{\mathbf{B}}^{-1} \tilde{\mathbf{A}} & -n_1 \tilde{\mathbf{B}}^{-1} \\ n_2 (\tilde{\mathbf{C}} - \tilde{\mathbf{D}} \tilde{\mathbf{B}}^{-1} \tilde{\mathbf{A}}) & n_2 \tilde{\mathbf{D}} \tilde{\mathbf{B}}^{-1} \end{pmatrix}}_{\tilde{\mathbf{R}}} \begin{pmatrix} \tilde{\mathbf{r}}_1 \\ \tilde{\mathbf{r}}_2 \end{pmatrix} \quad (2.3.20)$$

where all parameters are as defined in Eq. (2.3.15). Using Eq. (2.3.20), the spatio-temporal phase term in the exponential of Eq. (2.3.19) can be written in terms of the Lin matrix elements as [49]

$$\Phi = -\frac{k_0}{2} \begin{pmatrix} \tilde{\mathbf{r}}_1 \\ \tilde{\mathbf{r}}_2 \end{pmatrix}^T \tilde{\mathbf{R}} \begin{pmatrix} \tilde{\mathbf{r}}_1 \\ \tilde{\mathbf{r}}_2 \end{pmatrix}, \quad (2.3.21)$$

where  $\tilde{\mathbf{R}}$  is the  $6 \times 6$  matrix defined in Eq. (2.3.20). Since the phase is a scalar quantity, the matrix  $\tilde{\mathbf{R}}$  must have the property of transposition symmetry,

$$\tilde{\mathbf{R}} = \tilde{\mathbf{R}}^T. \quad (2.3.22)$$

From this transposition symmetry and the definition of  $\tilde{\mathbf{R}}$  in Eq. (2.3.20), the following relations between matrix elements can be derived:

$$\tilde{\mathbf{A}}^T \tilde{\mathbf{D}} - \tilde{\mathbf{C}}^T \tilde{\mathbf{D}} = \mathbf{I}, \quad \tilde{\mathbf{A}}^T \tilde{\mathbf{C}} = \tilde{\mathbf{C}}^T \tilde{\mathbf{A}} \quad \text{and} \quad \tilde{\mathbf{B}}^T \tilde{\mathbf{D}} = \tilde{\mathbf{D}}^T \tilde{\mathbf{B}} \quad (2.3.23)$$

Inserting Eq. (2.3.21) into Eq. (2.3.19) and using the relations in Eq. (2.3.23), the spatio-temporal Huygens integral is written in terms of the Lin matrix elements as

$$\psi_2(\tilde{\mathbf{r}}_2) = \zeta \iiint \psi_1(\tilde{\mathbf{r}}_1) \exp \left[ -i \frac{k_0}{2} \left( \tilde{\mathbf{r}}_1^T \tilde{\mathbf{B}}^{-1} \tilde{\mathbf{A}} \tilde{\mathbf{r}}_1 - 2 \tilde{\mathbf{r}}_1^T \tilde{\mathbf{B}}^{-1} \tilde{\mathbf{r}}_2 + \tilde{\mathbf{r}}_2^T \tilde{\mathbf{D}} \tilde{\mathbf{B}}^{-1} \tilde{\mathbf{r}}_2 \right) \right] d\tilde{\mathbf{r}}_1. \quad (2.3.24)$$

By imposing the energy conservation condition,

$$\iiint |\psi_2(\tilde{\mathbf{r}}_2)|^2 d\tilde{\mathbf{r}}_2 = \iiint |\psi_1(\tilde{\mathbf{r}}_1)|^2 d\tilde{\mathbf{r}}_1, \quad (2.3.25)$$

the constant amplitude factor  $\zeta$  in Eq. (2.3.24) is computed to be

$$\zeta = \left( \frac{i}{\lambda_0} \right)^{3/2} [\det(\tilde{\mathbf{B}})]^{-1/2}. \quad (2.3.26)$$

The equation given in Eq. (2.3.24) allows for the wave optical propagation of any paraxial pulsed beams through non-rotationally symmetric and dispersive optical systems with a given Lin matrix by numerical integration. However, for GPB input, the integral can be solved analytically giving simple propagation equations. Using the GPB in Eq. (3.2.17) as an input field to the generalized Huygens diffraction integral, it can

be shown (see Appendix B) that the field after propagation is also another GPB with the reduced complex field given by [44]

$$\psi_2(\tilde{\mathbf{r}}_2) = \frac{\psi_0}{\sqrt{\det(\tilde{\mathbf{A}} + \tilde{\mathbf{B}}\tilde{\mathbf{Q}}_1^{-1})}} \exp\left(-\frac{ik_0}{2}\tilde{\mathbf{r}}_2^T\tilde{\mathbf{Q}}_2^{-1}\tilde{\mathbf{r}}_2\right), \quad (2.3.27)$$

where  $\tilde{\mathbf{Q}}_2^{-1} = (\tilde{\mathbf{C}} + \tilde{\mathbf{D}}\tilde{\mathbf{Q}}_1^{-1})(\tilde{\mathbf{A}} + \tilde{\mathbf{B}}\tilde{\mathbf{Q}}_1^{-1})^{-1}$  is the  $3 \times 3$  complex spatio-temporal curvature matrix of the final GPB.

The spatio-temporal Huygen integral given in Eq. (2.3.21) is completely analogous with the generalized Collins integral in spatial domain, which is given by

$$\psi_2(\mathbf{r}_2) = \zeta_r \iint \psi_1(\mathbf{r}_1) \exp\left[-i\frac{k_0}{2}(\mathbf{r}_1^T\mathbf{B}^{-1}\mathbf{A}\mathbf{r}_1 - 2\mathbf{r}_1^T\mathbf{B}^{-1}\mathbf{r}_2 + \mathbf{r}_2^T\mathbf{D}\mathbf{B}^{-1}\mathbf{r}_2)\right] d\mathbf{r}_1. \quad (2.3.28)$$

with  $\zeta_r = \left(\frac{i}{\lambda_0}\right)[\det(\mathbf{B})]^{-1/2}$  obtained from the energy conservation condition and  $\mathbf{A}, \mathbf{B}, \mathbf{C}$  and  $\mathbf{D}$  are the  $2 \times 2$  matrices components of the  $4 \times 4$  spatial ABCD matrix. Similarly, the GPB propagation equation given in Eq. (2.3.27) above is completely analogous to that of the monochromatic GBs [48, 49],

$$\psi_2(\mathbf{r}_2) = \frac{\psi_0}{\sqrt{\det(\mathbf{A} + \mathbf{B}\mathbf{Q}_1^{-1})}} \exp\left(-\frac{ik_0}{2}\mathbf{r}_2^T\mathbf{Q}_2^{-1}\mathbf{r}_2\right), \quad (2.3.29)$$

where  $\mathbf{Q}_2^{-1} = (\mathbf{C} + \mathbf{D}\mathbf{Q}_1^{-1})(\mathbf{A} + \mathbf{B}\mathbf{Q}_1^{-1})^{-1}$  is the  $2 \times 2$  complex spatial curvature matrix of the final GB.

Although the analytical formula for propagation of GPBs using the Lin matrix method is fast, its application is limited to only to the propagation of GPBs through paraxial optical systems with no aberration and has only quadratic dispersion. However, real optical systems usually have combined effects of system aberrations, higher order dispersions and spatio-spectral distortions. In addition to that, the input pulsed beam can have amplitude profiles which are not necessarily Gaussian shaped and phase profiles which are more complicated than the simple quadratic ones. For such general cases, the ultrashort pulse propagation methods based on the temporal FT are usually employed.

### 2.3.3 Temporal Fourier transform based methods

Consider the propagation of an initial pulsed beam whose complex analytic electric field is given by [5]

$$E(x, y, t; 0) = E_r(x, y; 0)E_t(t)\exp\{i\omega_0 t\} \quad (2.3.30)$$

where  $E_r(x, y; z = 0)$  is the spatial profile of the pulse and  $E_t(t)$  is the temporal profile (pulse envelope) at the initial plane  $z = 0$ . The pulse in the spectral domain is usually obtained by taking the temporal FT of the given analytic field as

$$E(x, y, \omega; 0) = \mathfrak{F}\{E(x, y, t; 0)\}, \quad (2.3.31)$$

where  $\mathfrak{F}\{\cdot\}$  is the temporal FT operation defined in Eq. (2.1.3). For numerical propagation of the pulse, the analytic spectral field is sampled into  $N_\omega$  equidistant spectral components. The spatio-temporal profile of the initial pulse can be obtained by performing the IFT of the spectral components. For the numerical IFT

Once the input pulse is represented by properly sampled spectral equivalent, each spectral component is propagated through the given linear optical systems independently. This results in the spectral equivalent of the pulse at the output plane. The final spatio-temporal pulse profile is obtained by applying the IFT operation on the output pulse field as

$$E(x, y, t; z_f) = \mathfrak{F}^{-1}\{E(x, y, \omega; z_f)\}. \quad (2.3.32)$$

This operation requires that the number of spectral samples used should be large enough to ensure the proper sampling of the spectral phase and amplitude in the output plane as well.

As the linear spectral phase simply delays the pulse without affecting its profile, it is usually removed from the complex field before the Fourier transformation operations. This drastically reduces the number of spectral samples required and hence reducing the computer memory and computational time needed [13]. The remaining higher-order spectral and spatio-spectral phases terms increase the time window of the pulse which in turn requires a higher initial frequency sampling [9]. To propagate the complex field of each spectral component from the input to the output plane, appropriate linear propagation operators are used. For a homogenous medium, the spectrum of plane wave or the Fresnel propagation integral can be used [5]. However, for real non-

paraxial optical systems with multiple components, the propagation is done by the hybrid diffraction propagation method or the GBD method which are discussed below.

### Hybrid diffraction propagation

In the hybrid diffraction propagation method, an input field is propagated using the combination of the geometrical ray tracing, for propagation through real curved surfaces, and the wave optical propagation method, for propagation in homogenous media [14, 51]. For instance, for a focusing optical systems shown in Fig. 2.4, ray tracing is used to compute the spectral complex fields at the exit pupil of an optical system and a diffraction integral is used for the field propagation to the focal region. The complex field for each spectral component at the exit pupil is defined by

$$E_{ex}(p_x, p_y, \lambda_i) = A_{en}(p_x, p_y, \lambda_i) \exp \left[ -i2\pi \frac{W_{ex}(p_x, p_y, \lambda_i)}{\lambda_i} \right], \quad (2.3.33)$$

where  $\lambda_i$  is the wavelength of the spectral component,  $A_{en}(p_x, p_y, \lambda_i)$  is the spectral pupil amplitude apodization, and  $W_{ex}(p_x, p_y, \lambda_i)$  is the wavefront computed from the optical path difference (OPD) of the rays over the exit pupil for a given spectral component.

Once the complex fields at the exit pupil are computed, it is then propagated to the final plane of an optical system by using a wave optical method as the geometrical optics is not valid in the vicinity of the focus. Direct numerical integration of the Rayleigh-Sommerfeld diffraction integral on the complex field at the exit pupil plane is computationally intensive as a huge number

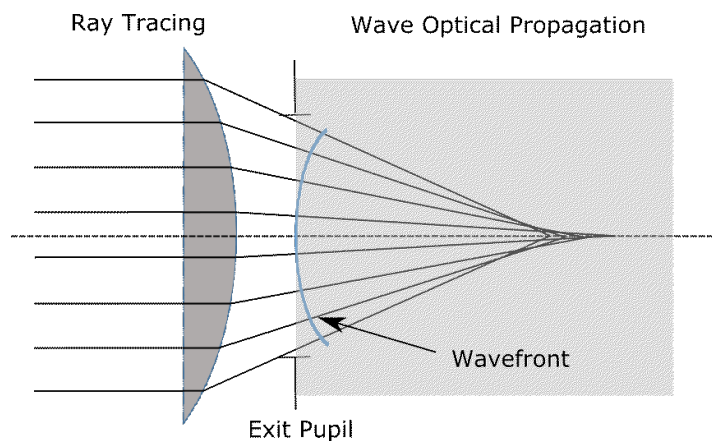


Figure 2.4: The schematic diagram showing the hybrid diffraction model

of sampling points are required for sampling the spherical phase of the initial field. Therefore, the complex pupil field is usually computed on the exit pupil sphere, which automatically compensates for the spherical part of the phase distribution, significantly reducing the number of sampling points required. Applying the small-angle approximation, similar to that of the Fraunhofer diffraction integral, the Rayleigh-Sommerfeld

diffraction integral reduces to a single spatial FT [52]

$$E(x, y, \omega; z_f) = \frac{\omega}{i2\pi cz_f} \exp\{-ikz_f\} \exp\left[-i\frac{k}{2z_f}\sqrt{x^2 + y^2}\right] \mathfrak{F}\{E'_{ex}(p_x, p_y, \omega)\}, \quad (2.3.34)$$

where  $E'_{ex}(p_x, p_y, \omega)$  is the complex spectral field in the exit pupil sphere,  $z_f$  is the distance of the focal plane from the exit pupil,  $k$  is the wavenumber,  $\omega$  is the angular frequency, and  $c$  is the speed of light in vacuum. Applying the temporal IFT, given in Eq. (2.1.4), on the pulse spectrum at the focal plane, given in Eq. (2.3.35), yields the space-time-distribution in the focal plane by phase correct superposition of all spectral components [8]. For a final plane which is shifted from the focal plane by  $\Delta z$ , the pulse spectrum is computed by manipulating the field distribution in the exit pupil with an additional spherical phase factor as

$$E(x, y, \omega; z_f + \Delta z) \propto \mathfrak{F}\left\{\exp\left[-ik\Delta z\sqrt{1 - \frac{1}{z_f}(p_x^2 + p_y^2)}\right] E'_{ex}(p_x, p_y, \omega)\right\}. \quad (2.3.35)$$

However, the application of such a hybrid diffraction method gives the pulse profile near the focal plane and requires a well-defined exit pupil, negligible diffraction except at the exit pupil and small phase aberration which may not be usually met in ultrashort pulse shaping systems [8, 15]. A more general field propagation approach is to divide the optical system into sub-systems and propagate the field using different techniques suitable for each sub-system [9, 10]. However, this usually requires frequent switching between geometrical rays and the complex electric field representations which is computationally intensive for systems with multiple components. In addition to that, for systems with large aberrations, the number of sampling points required by the FT can be extremely large to fulfill the sampling condition for the intermediate complex fields. As an alternative method of system diffraction calculation, A.W. Greynolds has proposed a wave optical propagation method that uses the fundamental GBs as the elementary fields instead of the plane waves [19].

### Gaussian beam decomposition

In the Gaussian beam decomposition (GBD) method, the given arbitrary non-paraxial field is first decomposed into a set of GBs [20, 53, 54]. Then, each GB is propagated through an optical system locally paraxially along its central ray. Finally, the propagated field at any point in the final or any intermediate plane is computed by a coherent superposition of the contributions of the complex field from each GBs after

propagation. The schematic illustration of the GBD method is given in Fig. 2.5. Un-

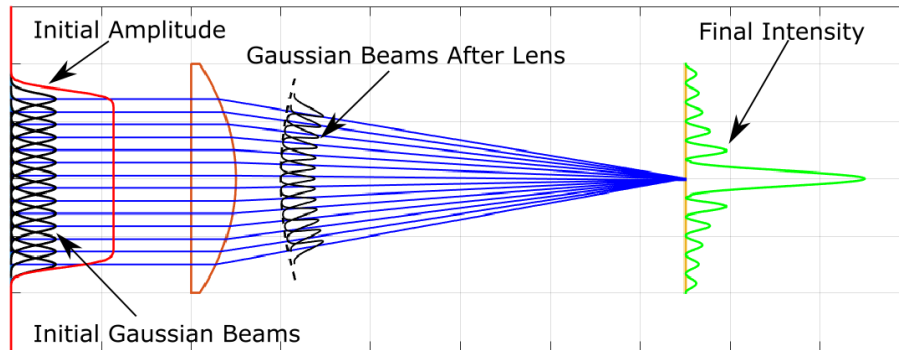


Figure 2.5: The schematic diagram showing the GBD method

like the plane waves, the GBs are very compact and their propagation through both homogeneous medium and a real curved interface can be easily computed, at least in the paraxial approximation [19, 21]. By using a set of multiple GBs, the GBD method allows for the propagation of an arbitrary input field through a real and aberrated optical systems in the scalar approximation. The impact of the aberration is taken into account by calculating each GB central rays exact.

Consider the decomposition of an input field with plane wavefront truncated by circular aperture using a set of uniformly distributed GBs over the input plane. To get a flat top-hat amplitude profile with minimum ripple, the adjacent GBs should partially overlap with each other. The overlap factor is defined by

$$\varepsilon_{OF} = \frac{2\omega_0}{\Delta C_0}. \quad (2.3.36)$$

where  $2\omega_0$  is the beam diameter (defined by using the 1/e amplitude) and  $\Delta C_0$  is the distance between the adjacent beam centers. For a rectangular grid sampling, the number of GBs required along one dimension to fill the aperture window with a given overlap factor  $\varepsilon_{OF}$  and beam waist width  $w_0$  is given by,

$$N_g = \text{ceil} \left( \frac{D\varepsilon_{OF}}{2w_0} \right), \quad (2.3.37)$$

where  $D$  is the width of the aperture window and  $\text{ceil}(\cdot)$  rounds the argument to the nearest integer greater than or equal to it. Hence, the total number of GBs required for the entire rectangular region in two dimensions becomes  $N_g^2$ .

For the decomposition of a super-Gaussian profile using a set of GBs with a width, the

overlap factor determines the number of GBs required and the amount of ripple on the resulting amplitude profile after the decomposition. This is demonstrated in Fig. 2.6 for one dimensional case. It can be seen that, as the overlap factor increases the peak-

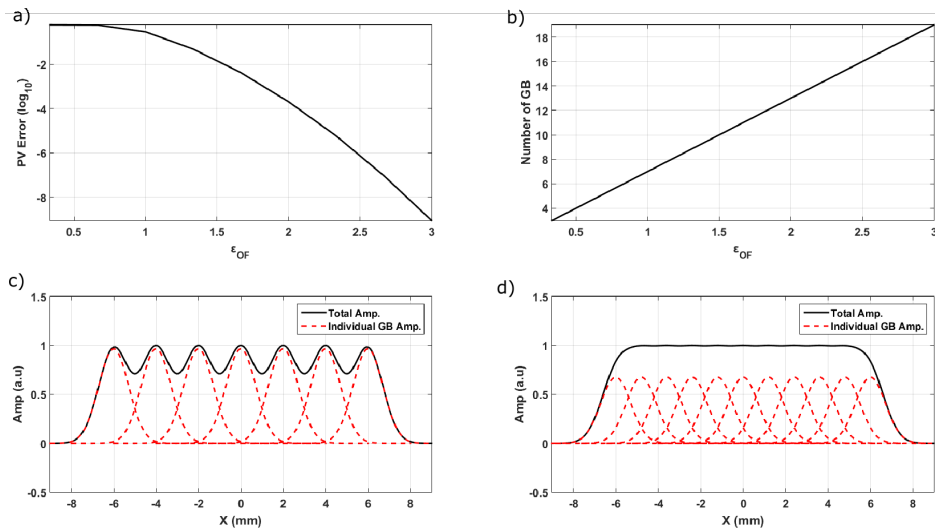


Figure 2.6: The effect of the overlap factor on a) the peak-valley error of the ripple on the top-hat amplitude profile oscillation, b) the number of GB required to fill the same window. The amplitudes of each GB together with the total superposed amplitude are shown for c)  $\varepsilon_{OF} = 1.0$  and d)  $\varepsilon_{OF} = 1.67$ . The width of individual GB is kept constant.

valley value of the amplitude ripple decreases and the number of GBs required increases. For overlap factors of 1.0 and 1.667, shown in Fig. 2.6 (c and d), a set of 7 and 11 GBs are used for the decomposition with the resulting ripple peak-valley of 28.84% and 0.41% , respectively. For common amplitude profiles, an overlap factor from 1.5 to 1.75 is usually sufficient [20,21]. After the GB distribution on the input plane is determined, the next step is to calculate the amplitude coefficients of individual GBs to give the required amplitude profiles. For a simple top hat amplitude profile, the amplitudes of individual GBs are simply taken to be equal. However, for general non-uniform amplitude profile, the amplitude coefficients of the individual GBs is determined using the least square fitting method. For a set of  $N$  GBs, the amplitude coefficients  $c_k$  of individual GBs should be determined such that the total amplitude  $a(x_i)$  at a given position  $x_i \in R$  is given by

$$a(x_i) = \sum_{k=1}^N c_k g_k(x_i), \quad (2.3.38)$$

where  $g_k(x_i)$  is the amplitude contribution of single GB at point  $x_i$ . For a set of  $M$



points in space, Eq. (2.3.38) can be written in matrix vector multiplication form as

$$\underbrace{\begin{pmatrix} g_{11} & g_{12} & \cdots & g_{1N} \\ g_{21} & g_{22} & \cdots & g_{2N} \\ \vdots & \vdots & \ddots & \vdots \\ g_{M1} & g_{M2} & \cdots & g_{MN} \end{pmatrix}}_{\mathbf{G}} \underbrace{\begin{pmatrix} c_1 \\ c_2 \\ \vdots \\ c_N \end{pmatrix}}_{\mathbf{c}} = \underbrace{\begin{pmatrix} a_1 \\ a_2 \\ \vdots \\ a_M \end{pmatrix}}_{\mathbf{a}}, \quad (2.3.39)$$

where  $g_{ij}$  is the amplitude of  $j^{\text{th}}$  beam at  $i^{\text{th}}$  point,  $c_j$  is the amplitude coefficient of the  $j^{\text{th}}$  beam and  $a_i$  is the total amplitude at the  $i^{\text{th}}$  point. For a typical decomposition problem using multiple GBs, the size of individual GB is significantly smaller than the given field window size. Therefore, each GB covers only certain limited points in the aperture and has negligible contribution to other points, resulting in the sparse matrix  $\mathbf{G}$  in Eq. (2.3.39) which is computationally advantageous<sup>5</sup>. If the number of GBs is equal to the number of data points ( $N = M$ ) in Eq. (2.3.39), then the solution for the coefficient vector can be uniquely determined given that the  $\mathbf{G}$  matrix is non-singular and hence is invertible. However, for typical GBD problem, the number of data points exceeds the number of GBs used ( $M > N$ ). Such overdetermined problem usually has no solution but the "best" coefficient vector  $\mathbf{c}$ , which minimizes the mean square error is given by [55]

$$\mathbf{c} = (\mathbf{G}^T \mathbf{G})^{-1} \mathbf{G}^T \mathbf{a}. \quad (2.3.40)$$

Finally the accuracy of the approximation is assessed by computing the root mean square error,

$$rms = \sqrt{\frac{\sum_{i=1}^M \Delta a_i^2}{M}}, \quad (2.3.41)$$

where  $\Delta a_i$  is the difference between the input amplitude and the approximated amplitude after the decomposition.

Once the input field is decomposed into a set of GBs, each GB is propagated through the optical system paraxially along its central ray. For propagating the paraxial GBs through optical systems along skew ray paths, two methods are commonly used: the paraxial ABCD system matrix-based method [56] and the complex ray-tracing method [19–21]. In this work, I have selected the ABCD system matrix-based method as it is suitable for further extension of the GBD method. The ABCD system matrix along

<sup>5</sup>Sparse matrix has most of its elements zero. In Matlab special routines are available for fast algebraic computation involving sparse matrices without storing the zero elements.

the central rays of each GBs is computed from the input to the output plane. Then, the matrix elements are used to compute the output GB parameters from the input ones using the methods discussed in section 2.3.2. After propagating all GBs to the final plane, the total field at the given point is computed by a coherent superposition of the complex field contributions from individual beams. For the phase correct superposition of multiple GBs, the phase factor due to the optical path length of the central ray should be added to the reduced complex field given in Eq. (2.3.29).

The GBD method is useful for performing an end-to-end diffraction calculation through macroscopic optical systems without switching between ray tracing and diffraction propagation [20, 57]. It enables the physical optics modeling of optical systems which have strongly curved and non-spherical wavefronts such as axicon and system with large aberration, which are complicated to model using the FT based methods [14, 21]. The GBD method allows for the computation of the propagated field at any point along the beam path through optical systems.

Although the conventional GBD has been used as an alternative method for wave optical diffraction calculation of optical systems and is incorporated in some commercial optical design computer programs [22–24], it has several limitations which are not yet addressed in the literature. Firstly, there has not been a published work on the systematic method of decomposing a field with generally curved wavefront using GBs which have different initial positions, directions, and curvatures depending on the local wavefront. The second and probably the main limitation of the conventional GBD method is that, it is not possible to accurately model sharp edge diffraction of the field after a hard aperture. This is because in GBD the sharp edge of the field is replaced with the smooth Gaussian edge. Additionally, the conventional GBD method is limited to propagating monochromatic fields and requires temporal FT methods for ultrashort pulse propagation. Hence the issue with sampling of fast oscillating spectral phase becomes critical for propagating through systems with large dispersion and spatio-spectral distortions. Furthermore, the conventional GBD method is usually discussed in the scalar field approximation and the propagation of vectorial fields using the GBD method is not well addressed in the literature. In this work, I have proposed several extension methods and developed algorithms that help in overcoming some of the aforementioned drawbacks of the GBD method.

## 2.4 Propagation of vectorial fields

The methods discussed so far are based on the scalar diffraction theory which ignores the polarization state of light, which is significant in some systems such as high NA focusing systems. In such cases, it is necessary to use the vectorial diffraction integral to trace the polarization states of light instead of the scalar wave equation. In this section the methods of propagating vectorial fields in both geometrical and physical optics approaches are briefly discussed.

### 2.4.1 Three dimensional (3D) polarization ray tracing

In the geometrical optics, the polarization states of each ray is usually traced through an optical system by using the Jones matrix method. In the Jones calculus, the polarization state of each ray in the local  $s-p$  coordinate system is given by a Jones vector and the effect of an interface or another optical component is given by  $2 \times 2$  Jones matrix [5]. However, for a non-paraxial ray tracing, the application of Jones calculus requires frequent transformations between the local and global coordinate systems. This makes the implementation of the Jones calculus very complicated and error-prone. In order to avoid such a morass, the three-dimensional polarization ray-tracing calculus is often used, which is the generalization of Jones calculus to three-by-three matrix formalisms [58, 59]. In the 3D polarization ray-tracing calculus, the polarization state of a given ray is specified by the three-element polarization vector given in the global coordinate system,

$$\mathbf{V} = \begin{pmatrix} V_x \\ V_y \\ V_z \end{pmatrix} = \begin{pmatrix} A_x \exp(-i\phi_x) \\ A_y \exp(-i\phi_y) \\ A_z \exp(-i\phi_z) \end{pmatrix}, \quad (2.4.1)$$

where  $A_{x,y,z}$  and  $\phi_{x,y,z}$  are the amplitudes and the phases of each polarization states.

The effect of an interface or an optical component on the polarization state of the ray is given by the  $3 \times 3$  polarization ray tracing matrix. The polarization ray tracing matrix of an optical component, such as an interface with multilayer coating, is computed from its usual  $2 \times 2$  Jones matrix by

$$\mathbf{P} = \mathbf{R}_{LG}^{out} \mathbf{J}_{3 \times 3} \mathbf{R}_{GL}^{in}, \quad (2.4.2)$$

where  $\mathbf{R}_{LG}^{out}$  is the local (s-p-k) to the global (x-y-z) coordinate transformation matrix after the component,  $\mathbf{R}_{GL}^{in}$  is the global (x-y-z) to the local (s-p-k) coordinate transfor-

mation matrix before the component and  $\mathbf{J}_{3 \times 3}$  is the Jones matrix of the component in the local coordinate system embedded in the left-top corner of the  $3 \times 3$  identity matrix as

$$\mathbf{J}_{3 \times 3} = \begin{pmatrix} J_{ss} & J_{sp} & 0 \\ J_{ps} & J_{pp} & 0 \\ 0 & 0 & 1 \end{pmatrix}. \quad (2.4.3)$$

The coordinate transformation matrices can be obtained from the local coordinate systems which are defined using the incoming and outgoing ray directions at the interface as shown in Fig. 2.7. Like in the Jones calculus, the total polarization ray tracing matrix  $\mathbf{P}_{tot}$  of a sequence of optical components is computed from the polarization ray tracing matrices  $\mathbf{P}_q$  of individual components by

$$\mathbf{P}_{tot} = \mathbf{P}_N \mathbf{P}_{N-1} \dots \mathbf{P}_2 \mathbf{P}_1 = \prod_{q=N,-1}^1 \mathbf{P}_q. \quad (2.4.4)$$

The output polarization vector  $\mathbf{V}_2$  of the electric field after an optical system is computed from the input polarization vector  $\mathbf{V}_1$  by using

$$\mathbf{V}_2 = \mathbf{P}_{tot} \mathbf{V}_1 \implies \begin{pmatrix} V_{x,2} \\ V_{y,2} \\ V_{z,2} \end{pmatrix} = \begin{pmatrix} P_{xx} & P_{xy} & P_{xz} \\ P_{yx} & P_{yy} & P_{yz} \\ P_{yz} & P_{zy} & P_{zz} \end{pmatrix} \begin{pmatrix} V_{x,1} \\ V_{y,1} \\ V_{z,1} \end{pmatrix}. \quad (2.4.5)$$

The main advantage of the three-dimensional polarization ray-tracing calculus over the Jones calculus is that the final polarization state is computed in a single step without requiring the frequent coordinate transformations during tracing [59]. However, as the polarization ray tracing is based on the geometrical ray tracing, it is not valid in cases where the diffraction effects are significant such as the focal region of focusing optics. In such cases, it is necessary to use the vectorial diffraction integral to get the electric field components as discussed in the following section.

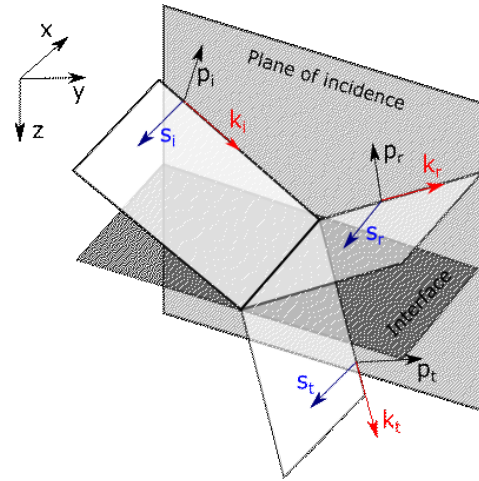


Figure 2.7: The local coordinate systems for the ray reflected and refracted from a plane interface.

### 2.4.2 Vectorial diffraction for high NA focusing

Consider the focusing of a polarized input field by an optical system with plane entrance pupil and spherical exit pupil as show in in Fig. 2.8. The incident field  $\mathbf{E}_i(r, \phi)$  at point  $Q_1$  is decomposed into the s-polarized (tangential) and the p-polarized (radial) components. At the exit pupil of the optical system, the wave field is deflected in the radial plane and focused towards the focal point [60]. The complex amplitudes of the transmitted field at the corresponding point  $Q_2$  on the exit pupil sphere is given by a three element vector which is computed by

$$\mathbf{E}_t(\theta, \phi) = t_p(\mathbf{E}_i \cdot \mathbf{p}_1) \mathbf{p}_2 + t_s(\mathbf{E}_i \cdot \mathbf{s}_1) \mathbf{s}_2 \quad (2.4.6)$$

where  $t_p(\theta, \phi)$  and  $t_s(\theta, \phi)$  are the complex transmission coefficients (due to accumulated phase distortions and attenuation) of the optical system for the p- and s-polarization components, respectively. The unit vectors of the s- and p-components at the entrance and exit pupils are given by

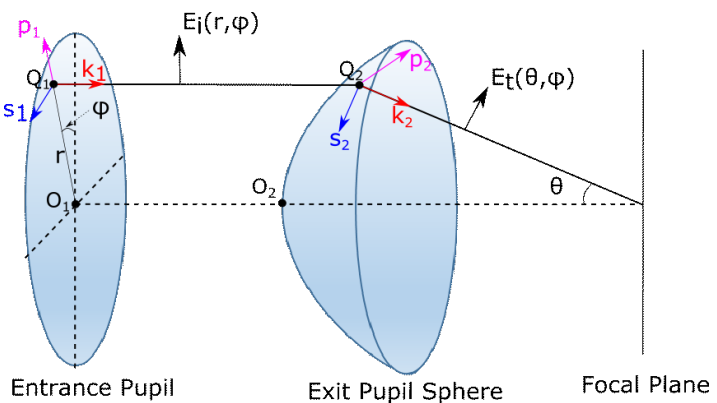


Figure 2.8: The geometry of a high NA focusing.

$$\mathbf{s}_1 = \begin{pmatrix} -\sin \phi \\ \cos \phi \\ 0 \end{pmatrix} \quad \mathbf{p}_1 = \begin{pmatrix} \cos \phi \\ \sin \phi \\ 0 \end{pmatrix} \quad \mathbf{s}_2 = \mathbf{s}_1 \quad \text{and} \quad \mathbf{p}_2 = \begin{pmatrix} \cos \phi \cos \theta \\ \sin \phi \cos \theta \\ \sin \theta \end{pmatrix}, \quad (2.4.7)$$

where  $\theta$  and  $\phi$  are angles as shown in Fig. 2.8.

In the diffraction computation according to the Debye approximation, each point of the exit pupil is taken as the source of a plane wave with amplitude, phase and polarization prescribed by this point. Hence, the vectorial field at any point  $(x, y, z)$  in the focal region is obtained by integrating the propagated plane waves by [60, 61]

$$\mathbf{E}(x, y, z) = -\frac{if}{\lambda_0} \int_{\theta=0}^{\theta_{max}} \int_{\phi=0}^{2\pi} \mathbf{E}_t(\theta, \phi) \sin \theta \exp\{i(k_z z - k_x x - k_y y)\} d\phi d\theta \quad (2.4.8)$$

where  $\theta_{max} = \arcsin NA/n_t$  with  $NA$  and  $n_t$  being the numerical aperture and the

last medium refractive index of the system, and  $k_x, k_y$  and  $k_z$  are elements of the wave vector  $\mathbf{k}_t$  of the transmitted field which is given by

$$\mathbf{k}_t(\theta, \phi) = \frac{2\pi}{\lambda_0} n_t \begin{pmatrix} -\cos \phi \sin \theta \\ -\sin \phi \sin \theta \\ \cos \theta \end{pmatrix}. \quad (2.4.9)$$

The diffraction integral in Eq. (2.4.8) is called the vectorial Debye diffraction integral. For fast computation, the Debye integral is usually rewritten in terms of FT by [60]

$$\mathbf{E}(x, y, z) = -\frac{if}{\lambda_0 k_t^2} \mathfrak{F} [\mathbf{E}_t(\theta, \phi) \exp\{ik_z z\} / \cos \theta] \quad (2.4.10)$$

The FT in Eq. (2.4.10) requires the sampling condition to be fulfilled for both the field  $\mathbf{E}_t(\theta, \phi)$  at the exit pupil and the propagation kernel  $\exp\{ik_z z\}$ . For an optical system with large aberrations, the sampling of fast oscillating residual phase becomes critical.

### 3. New Extensions to the Gaussian Beam Decomposition Method

In this chapter the new methods which are developed to address some of the limitations and challenges of the conventional GBD method discussed in chapter 1 and 2 above are presented. These newly proposed methods and developed algorithms are the main contributions of this Ph.D. project. Most of the methods discussed in this chapter have already been published in the peer-reviewed journals [53, 62–65]. The example calculations for the validation of the methods and demonstrate their application is presented separately in the next chapter (chapter 4).

#### 3.1 Curved wavefront decomposition

For fields with strongly curved wavefronts, the fast oscillating phase of the complex field on the initial plane makes it difficult to perform the GBD on the input plane [25, 54]. This can be overcome by performing the GBD directly on the wavefront surface, without going to the complex field representation on a single plane. Although this idea has been briefly mentioned in a previous study [20], the detailed decomposition algorithm is not discussed yet in the literature to the best of my knowledge. In this work I propose and describe a method to decompose a smooth wavefronts into a set of GBs that are distributed directly on the wavefront surface, have different positions, directions, and non-zero initial phase curvatures.

The decomposition of a field with a smooth wavefront  $\phi(x, y)$  and a given amplitude profile starts by taking several overlapping GBs distributed on the  $XY$  plane using a given sampling scheme as shown in Fig. 3.1. The Fibonacci sampling grid is used here as it usually gives better accuracy for circular aperture in the radial basis function fitting problems [66]. Different sampling scheme which can be used in the GBD are briefly discussed in Appendix E. For a given total number of GBs used, the width of individual GBs is determined in such a way that each beam overlaps partially with its neighboring beams as shown in Fig. 3.1a. The number of GBs required and the overlap factor used depends on the wavefront and amplitude profiles of the input field. As discussed in subsection 2.3.3 above, for the overlap factor a typical value in the range of 1 to 1.75 is usually used. The basic principles for estimating the number of GBs required is given at the end of this subsection. For each sampling point  $(x_g, y_g)$  on

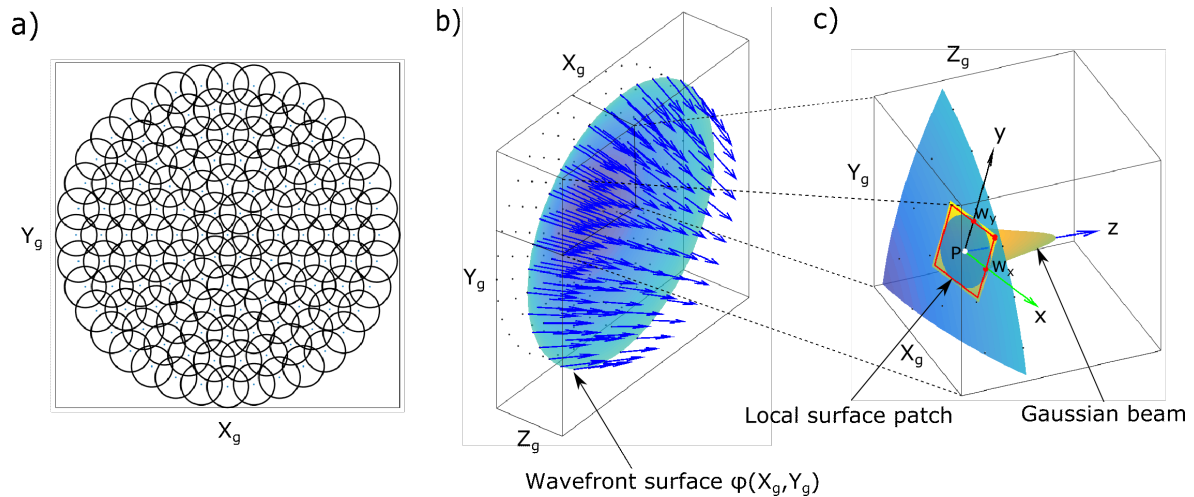


Figure 3.1: a) The footprint of overlapping GBs projected on the transversal X-Y plane. b) The directions (shown in blue arrows) of all GBs used for decomposition of a given curved wavefront. c) The local surface patch of a single GB d) Sketch showing different parameters of the rays representing a single GB computed by the decomposition algorithm. Here only the YZ-cross section is shown for simplicity and the size of the GB is exaggerated.

the XY plane, a GB is placed in the corresponding point on the wavefront surface as shown in Fig. 3.1b. Each GB is rotated in such a way that the directions of its central rays are along the wavefront surface normal at the beam center point. Then a local coordinate system is defined for each GB with z-axis being along the beam direction and the x- and y- axes on the plane tangent to the wavefront at the beam center as shown in Fig. 3.1c. In the local coordinate of a given GB, the Taylor expansion of the given wavefront surface in the quadratic approximation results in

$$z_q(x, y) = c_{xx}x^2 + c_{xy}xy + c_{yy}y^2, \quad (3.1.1)$$

where  $c_{xx}, c_{xy}$  and  $c_{yy}$  are the coefficients of the expansion. The constant offset and the linear term does not appear in Eq. (3.1.1) due to the special choice of the local coordinate system. The local quadratic approximation of a given wavefront surface around a given point on the wavefront can be done using two approaches. The first approach is by using a paraboloid which has the same curvature as the local wavefront surface curvature at the given point. This results in the quadratic approximation which is exact at the GB center point but may have a large deviation in the neighborhood. Alternatively, the coefficients of the local quadratic approximation in Eq. (3.1.1) can be computed by forcing a paraboloid placed at the center point to match with the given wavefront surface at least at three points on the edge of a finite surface patch around



the point. This results in the quadratic approximation which has a small deviation not only at the center but also in the finite area around the center point. To illustrate this, consider the parabolic approximations of the spherical wavefront in 1D using the two approaches as shown in Fig. 3.2. From the residual error plot in Fig. 3.2b, it can

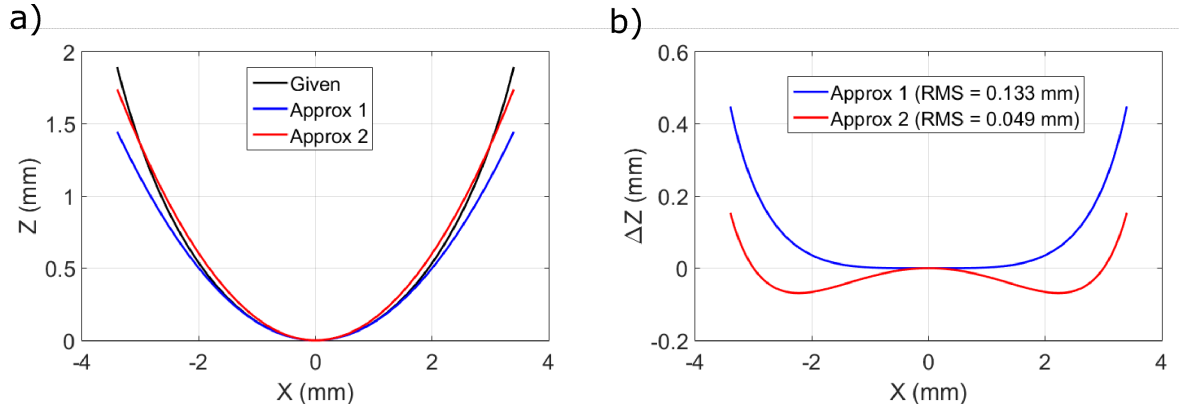


Figure 3.2: a) Parabolic approximations of a spherical wavefront, with a radius of  $4\text{mm}$ , by using the curvature at the center (in approx. 1) and by forcing the parabolic wavefront to coincide with the given one at a finite width  $x = 3\text{mm}$  (in approx. 2). b) The residual error of the two approximations shown in (a).

be seen that the second method gives better approximation (with small RMS error) over wider area. Therefore, the second approach is employed for the computation of the curvatures of the GBs used to decompose curved wavefronts. The size of the finite surface patch considered around the beam center is determined by the width of the GB. For the GB in 3D space as shown in Fig. 3.1c, the quadratic coefficients are computed by

$$\begin{aligned} c_{xx} &= \frac{z_\phi(w_x, 0)}{w_x^2} \quad , \quad c_{yy} = \frac{z_\phi(0, w_y)}{w_y^2} \quad , \\ c_{xy} &= \frac{z_\phi(w_x, w_y) - (c_{xx}w_x^2 + c_{yy}w_y^2)}{w_x^2w_y^2} \quad , \end{aligned} \quad (3.1.2)$$

where  $w_x$  and  $w_y$  are the waist radius of the GB and  $z_\phi(x, y)$  is the surface sag of the given wavefront at a given point in the local coordinate system. From the equations of the GB given in Eq. (2.3.5 - 2.3.7), the complex curvature matrix elements of the GB are given by

$$\begin{aligned} q_{xx}^{-1} &= -2c_{xx} - 1i \frac{\lambda_0}{\pi w_x^2} \quad , \quad q_{yy}^{-1} = -2c_{yy} - 1i \frac{\lambda_0}{\pi w_y^2} \quad , \\ q_{xy}^{-1} &= q_{yx}^{-1} = -c_{xy} \quad . \end{aligned} \quad (3.1.3)$$

Once the given wavefront is well represented with the GB phase curvatures, the amplitudes of each GBs are computed by using the method of least square fitting method discussed in section 2.3.3 above.

### On the estimation of the number of GBs

For a given overlap factor, the minimum number of GBs required to decompose a given input field depends on the overall size of the field, and the maximum width allowed for the individual GBs used as given in Eq. (2.3.37). However, as the width of the individual GBs increases, the accuracy of the quadratic approximation of the local wavefront as well as the maximum spatial frequency in the amplitude profile which can be represented by the GB decrease. Therefore, the estimation of the maximum width of the GB to use should consider both the amplitude profile and the wavefront of the input field.

For instance, for a spherical wavefront, the residual error of the quadratic approximation of the wavefront using GBs depends on the radius of curvature of the wavefront  $R$  and the GB width  $w_0$ . Figure 3.3 shows the RMS value of the intensity weighted residual wavefront error of the quadratic approximation as function of  $R$  and  $w_0$  for wavelength of  $\lambda = 0.5\mu m$ . For a given target residual error, the maximum GB width allowed to represent a spherical wavefront with a specific radius of curvature can be directly obtained

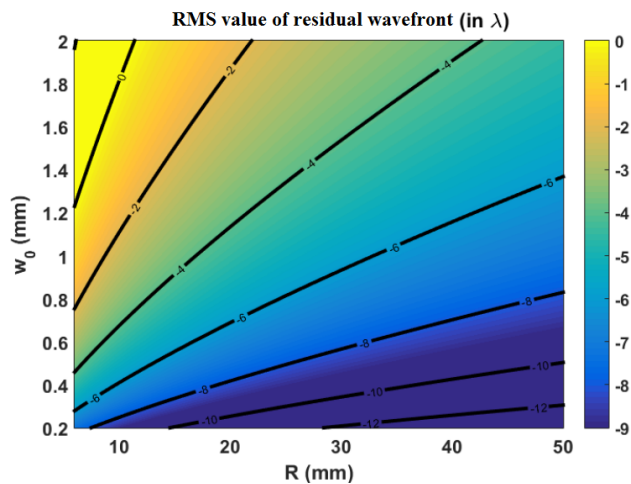


Figure 3.3: The weighted RMS values of the residual wavefront error for the quadratic approximation of spherical wavefront with different radius of curvature  $R$  using a single GB with different  $1/e$  beam width  $w_0$ . The logarithm value of the calculated result is shown in the plot.

from the plot. In addition to the wavefront approximation, the width of the elementary GBs determines the maximum spatial frequency in the amplitude profile which can be represented by the GBD. For a given field with oscillating amplitude profiles, GBs with small width should be used to represent the large spatial frequencies. The spatial frequency content of a given amplitude profile can be obtained by performing the FT.

The GBD method discussed in this section allows the decomposition of a monochromatic field with a curved wavefront and an arbitrary amplitude profile. As the de-

composition is done directly on the wavefront surface without going to the complex field in a single plane, the method does not suffer from the sampling problem of the fast oscillating phase. In addition to that, this method utilizes the initial direction and curvature parameters of the GBs to best fit the local wavefront which reduces the number of GBs required for the decomposition with a given accuracy.

## 3.2 Extension to ultrashort pulse propagation

For a linear optical system, the Gaussian beam decomposition (GBD) method allows for the propagation of a monochromatic field with arbitrary spatial amplitude and wavefront profile through an optical system. Analogously, it is reasonable to think that a Gaussian pulse decomposition (GPD) method can be used to propagate an input pulse with arbitrary spectral amplitude and phase through dispersive optical systems. However, such an approach for ultrashort pulse propagation has not yet been addressed in the literature. In this section, I propose a method of decomposing an ultrashort pulse with arbitrary spectral amplitude and phase profiles into a finite number of delayed and chirped Gaussian pulses with different central frequencies. Then, by combining the GBD with the GPD methods, a new alternative method for the spatio-temporal propagation ultrashort pulsed beams through real optical systems is developed.

### 3.2.1 Decomposition of arbitrary spectral profile

Consider the decomposition of a general spectral profile of an ultrashort pulse with an arbitrary spectral amplitude and phase profiles into a set of GPs with different central frequencies, peak amplitudes and having overlapping spectral profiles as shown in Fig. 3.4. The first step in the spectral GPD is the determination of the spectral range over which the spectral amplitude has non-negligible values. Then,  $N_\omega$  uniformly sampled points are taken over the resulting frequency range and used as the central frequencies of the GPs used for the decomposition. The spectral profiles of the adjacent GPs are generated to overlap with a given spectral overlap factor  $\varepsilon_{OF}^\omega$  which is defined by

$$\varepsilon_{OF}^\omega = \frac{2\sigma_\omega}{\Delta\omega_0}, \quad (3.2.1)$$

where  $\sigma_\omega$  is the spectral width of the pulse (defined by using the 1/e amplitude) and  $\Delta\omega_0$  is the spectral separation between the adjacent pulse centers. Like in the case of the spatial GBD, the spectral overlap factor determines the smoothness of the total amplitude profile after the decomposition and for most cases the typical values between

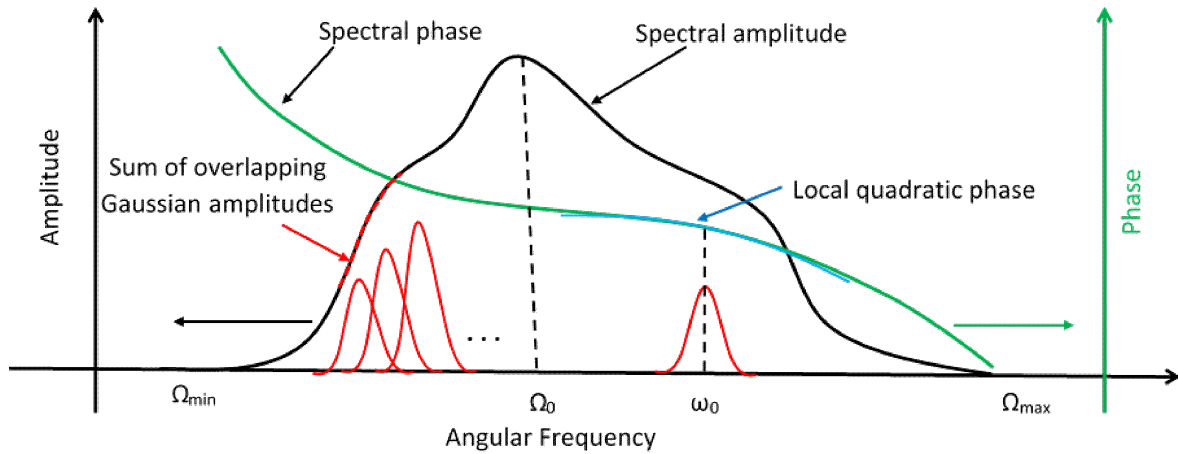


Figure 3.4: The schematic diagram showing the spectral decomposition of an ultrashort pulse with an arbitrary spectral amplitude and phase profile into set of Gaussian pulses.

1.5 and 1.75 give good results. For a uniform sampling scheme, the spectral width of each GP is given by

$$\sigma_{\omega} = \frac{1}{2} \frac{(\Omega_{max} - \Omega_{min})}{N_{\omega}} (\varepsilon_{OF}^{\omega}), \quad (3.2.2)$$

where  $\Omega_{max}$  and  $\Omega_{min}$  are the maximum and minimum angular frequency with non-negligible input amplitude, respectively.

Once the GP distributions are fixed, the next step is the computation of the delay and chirp parameter of individual GPs from the given spectral phase. The parameters are determined in such a way that the individual GP properly represents the given spectral phase up to the quadratic order locally. To this end, the second order Taylor expansion is applied on the given spectral phase about the central angular frequency  $\omega_0$  of each GP as

$$\phi(\omega) \Big|_{\omega_0} \approx \phi_0 + \phi_1(\omega - \omega_0) + \phi_2(\omega - \omega_0)^2, \quad (3.2.3)$$

where the Taylor expansion coefficients are given by  $\phi_0 = \phi(\omega_0)$ ,  $\phi_1 = \phi'(\omega_0)$  and  $\phi_2 = 0.5\phi''(\omega_0)$ . The constant term ( $\phi_0$ ) and the linear coefficient ( $\phi_1$ ) in the Taylor expansion give the constant phase offset and the group delay of the GP. Whereas, the quadratic coefficient ( $\phi_2$ ) corresponds to the temporal chirp of the GP which determines its temporal complex curvature.

From the temporal FT of the GPB given in Eq. (2.3.10), the spectral profile at the

center of the GPB is given by

$$E(\mathbf{r} = 0, \bar{\omega}) \propto \exp\left(i\frac{1}{2k_0c^2q_{\tau\tau}^{-1}}\bar{\omega}^2\right), \quad (3.2.4)$$

where  $\bar{\omega} = \omega - \omega_0$ . Separating the real and imaginary parts, the term inside the exponent in Eq. (3.2.4) can be written in terms of the spectral width  $\sigma_\omega$  and the quadratic spectral phase coefficient  $\phi_2$  as

$$i\frac{1}{2k_0c^2q_{\tau\tau}^{-1}}\bar{\omega}^2 = -\frac{\bar{\omega}^2}{\sigma_\omega^2} + i\phi_2\bar{\omega}^2. \quad (3.2.5)$$

From Eq. (3.2.5), the complex curvature parameter of the GP is computed from the quadratic coefficient ( $\phi_2$ ) of the local spectral phase by using

$$q_{\tau\tau}^{-1} = i \left[ 2k_0c^2 \left( -\frac{1}{\sigma_\omega^2} + i\phi_2 \right) \right]^{-1}. \quad (3.2.6)$$

The GPD in the spectral domain allows for the ultra-wide spectral bandwidth of the given ultrashort pulse to be represented with a set of GPs with much narrower bandwidth which can be propagated using the parabolic wave equation discussed in 2.3.2. Finally, like in the case of monochromatic GBD, the least square fitting method is used to compute the peak amplitudes of each GPs so that their total superposition results in the given spectral amplitude.

The number of GPs required for the decomposition depends on the complexity of the given spectral amplitude and/or phase profiles and the spectral bandwidth of the given pulse. If the spectral amplitude and/or phase profile is not very smooth and/or its spectral bandwidth is very wide, then a large number of GPs are required. In addition to that, the spectral width of each GP used should be small enough for the validity of slowly varying approximation and the parabolic wave equation, which is used during the propagation of individual GPs.

### 3.2.2 Gaussian pulsed beam decomposition

The Gaussian pulsed beam decomposition (GPBD) method is an extension of the monochromatic GBD method to handle linear propagation of ultrashort pulsed beams through general dispersive non-paraxial optical systems. Like the conventional GBD method, the GPBD method also involves three steps: first decomposition of the given

ultrashort pulse into a set of GPBs, then propagation of individual GPBs, and finally superposition of the complex amplitudes to get the propagated pulse-field at any spatiotemporal target point.

As the decomposition of ultrashort pulses with spatio-temporal coupling is too complicated, here it is assumed that there is no spatio-temporal coupling in the input ultrashort pulse. Hence, the spatial and the spectral (temporal) components of the input pulse are initially separable. With this assumption, the spatial and spectral components of the input pulsed beam are decomposed independently into a set of Gaussian beams (GBs) and Gaussian pulses (GPs) respectively using the methods discussed in sections 3.1 and 3.2.1. It is important to note that, the assumption of no spatio-temporal coupling is required only for the initial pulse field. The spatio-temporal coupling due to the propagation through optical systems is fully taken into account by the GPB propagation method.

Once the input spatial and spectral profiles are decomposed into a set of GBs and GPs respectively, the complete GPB set representing the input ultrashort pulse is obtained by combining the two sets. For instance, using  $N_r$  GBs for the spatial decomposition and  $N_\omega$  GPs for the spectral decomposition, a total of  $N_r \times N_\omega$  GPBs are used for the decomposition. The individual GPBs are then propagated through the optical systems independently using the Lin matrix method discussed in section 2.3.2. The linearity of the scalar wave diffraction integrals implies that if the initial pulsed beam is properly represented with a set of GPBs, then the propagated field should also be accurate in the superposition [67].

The reduced complex field of the propagated GPB given in Eq. (2.3.27) is computed in the local temporal coordinate which is measured in the co-moving reference frame which travels together with the pulse peak. Hence, it is very important to determine the location of the peak of the GPB at any given global flight time. This is usually done by computing the group delay from the numerical derivative of the optical path length with respect to the angular frequency near the carrier frequency [9, 68]. However, in the following subsection the concept of group path length is introduced, which allows the exact analytical calculation of the group delay for each ray directly during the ray tracing. For a single GPB propagation, the absolute phase of the outgoing pulsed beam is not usually required. However, as multiple GPBs are used in the GPBD method, the total absolute phase and the total group delays of the individual GPBs should

be correctly computed and traced for the phase correct superposition in the detector plane.

### 3.2.3 The concept of group path length

It is well known that the time taken for a monochromatic wavefront to travel a geometrical distance  $\Delta z$  through a medium with refractive index of  $n$  (at the given wavelength) is given by

$$t_{phase} = \frac{n\Delta z}{c}, \quad (3.2.7)$$

where  $c$  is the speed of light in vacuum. The product of the geometrical path length and the refractive index of the medium, also known as the optical path length ( $\Delta_{OPL}$ ), is a very important parameter to determine the phase of monochromatic beams propagating through optical systems.

For pulsed beams, the time taken for the pulse group maxima is different from that of the carrier wavelength due to the difference in the group and phase velocities (in other words the refractive index and the group indices) inside dispersive media. The time taken for the pulse group to travel a geometric distance of  $\Delta z$  through a medium with group index  $n_g$  is given by

$$t_{group} = \frac{n_g\Delta z}{c}. \quad (3.2.8)$$

Here I define the product of the geometrical path length and the group index of the medium as a group path length ( $\Delta_{GPL}$ ) which is given by

$$\Delta_{GPL} = n_g\Delta z. \quad (3.2.9)$$

Like the optical path length, the group path length can be computed for each GPBs propagating through real dispersive optical systems during ray tracing of the central rays by adding the group path lengths of the individual sub-paths in the system. The analytical formulae for the group indices of glasses can be derived directly from the derivatives of the dispersion equations of the medium using Eq. (2.1.9) [3, 4]. This allows the exact analytical calculation of the total group delay of each pulsed ray without using the finite difference approximation. When a ray is refracted or reflected from an optical interface between two media, just like the optical path length, the group path length also remains unchanged. However for the diffraction grating, which is commonly used in the pulse shaping systems, the change in the optical path length and hence the group path length requires additional correction terms which are

discussed in the following section.

### 3.2.4 Modeling of ideal diffraction grating

Diffraction gratings are one of the commonly used components in the ultrashort pulse shaping optical systems such as pulse stretchers and compressors. Therefore, modeling the effects of a diffraction grating on an ultrashort pulse is very crucial for modeling of a complex ultrashort-pulse optical systems. A diffraction grating diffracts an incoming electric field into several directions with different diffraction efficiencies depending on the grating period, the diffraction orders used and the wavelength of the field. As the diffraction efficiency of a real grating depends on the shape and nature of the grating structure within a single period, its rigorous analysis usually requires computationally intensive FT based methods [69–71]. In the GPBD method the diffraction efficiencies of each diffraction order cannot be computed rigorously. Nevertheless, the GPBD method can be used to model the diffraction and angular dispersion of an idealized diffraction grating, with a diffraction efficiency of 100% or any other value obtained from an independent calculation for a given diffraction order.

For a GPB incident on a linear diffraction grating, the direction of the transmitted or reflected light is determined by performing the real ray tracing of its central ray using the generalized diffraction grating equation [39, 72, 73]. The application of the grating equation requires that the groove width of the grating should be smaller, at least by a factor of 5, than the beam footprint diameter but large enough for the mathematical validity of the grating equation [73]. Although this condition is usually fulfilled for pulse shaping systems, it has to be checked for all GPBs during the propagation. The effect of the diffraction grating on the spatio-temporal complex curvature matrix of the GPB is computed from the Lin matrix of the grating [44].

Unlike other simple interfaces, the absolute phase of light reflected from or transmitted through a diffraction grating cannot be simply obtained from the usual optical path length calculation using the grating equation [74]. An additional correction term should be added to the total phase and group delay of the individual GPBs for an appropriate mix of geometrical and physical optics [72, 74, 75].

Consider a ray pulse from a point  $A$  impinging at point  $P$  on an ideal diffraction grating in air with grating period of  $d$  and rulings parallel to the x-axis as shown in Fig. 3.5. The direction of the reflected ray can be computed by using the general-



ized 3D ray tracing procedure [39, 72]. Taking a point  $A'$  in the reflected ray path for a given diffraction order  $m$ , the total optical path length accumulated by the wavefront as it travels from point  $A$  to  $A'$  is given by

$$\Delta_{OPL} = \overline{AP} + \overline{PA'} + \Delta_{OPL}^a, \quad (3.2.10)$$

where  $\overline{AP}$  and  $\overline{PA'}$  are the geometrical path lengths, and the third term

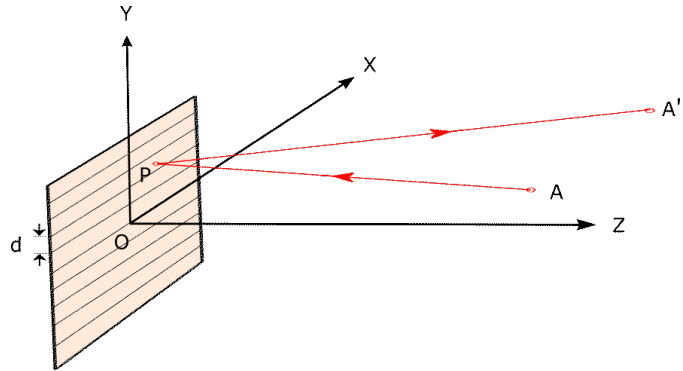


Figure 3.5: Schematic diagram of a ray reflected from a grating.

$$\Delta_{OPL}^a = \frac{m\lambda y}{d}, \quad (3.2.11)$$

gives the additional effect of the diffraction grating on the incoming wavefront [72, 74]. For the detailed discussions and interpretations of this additional optical path length correction term, the reader is referred to the literature [72, 74–76].

Because of the optical path length correction, it is reasonable to think that one also needs some correction on the group path length of the ray pulse reflected from the ideal grating. This group path length correction is computed by taking the spectral derivative of the additional phase shift due to diffraction grating. The total phase shift of the ray from  $A$  to  $A'$  is given by the sum of the phase shift due to the propagation distances and an additional linear phase due to the grating which is given by

$$\phi_a = \frac{2\pi}{\lambda}(\Delta_{OPL}^a) = \frac{2\pi m y}{d}. \quad (3.2.12)$$

The additional phase in Eq. (3.2.12) is independent of the wavelength and hence the associated additional group path length becomes

$$\Delta_{GPL}^a = c \frac{\partial \phi_a}{\partial \omega} = 0, \quad (3.2.13)$$

where  $c$  is the speed of light in vacuum.

Therefore, for a ray pulse reflected from or transmitted through a diffraction grating, the total group delay is the same as that computed from the geometrical path lengths without any additional correction. In addition to enabling the phase correct

superposition in the GPBD method, this result can be applied to perform geometrical dispersion analysis of complicated optical systems with multiple diffraction grating in a general 3D orientation in space. For a simple well-aligned grating pair compressor, the independence of the total group delay on the phase correction term has been reported in the literature using geometrical construction followed by a long analytical derivation [74–76]. For a single GPB reflected from an ideal diffraction grating, the additional linear phase across its local spatial cross-section is already incorporated in the new direction of the beam. However, since multiple GPBs are used in the GPBD method, it is necessary to consider the relative additional phase of individual GPBs for a phase-correct superposition. Using the method discussed in this section, it is possible to propagate an ultrashort pulse (with arbitrary spatial and spectral profiles) through complicated phase shaping systems containing diffraction grating using the GPBD method.

### 3.2.5 Spatio-temporal coupling in free space propagation

The spatial and the temporal properties of a GPB get coupled and the pulse front gets distorted even during free-space propagation. This is due to the fact that in free space, where the group velocity is the same as the phase velocity, the pulse front travels together with the phase front which gets curved due to the diffraction of the field. This results in a curved pulse front with different arrival times of the pulse for different off-axis points [77–79]. However, in the previous studies dealing with the matrix method for pulsed beam propagation [35, 44, 46, 47], this off-axis delay is usually not considered. This can only be justified for short propagation distances (compared to the Rayleigh length) or for temporally long and slowly diverging pulsed beams. However, in the GPBD method, it is

important to consider the off-axis delay time for the phase correct superposition of many GPBs. For a rotationally symmetric GPB, the pulse front for off-axis points is delayed by  $\Delta t$  which is given by [77]

$$\Delta t(y) = \frac{y^2}{2cR(z)}, \quad (3.2.14)$$

where  $y$  is the transversal coordinate of the off-axis point,  $c$  is the speed of light in

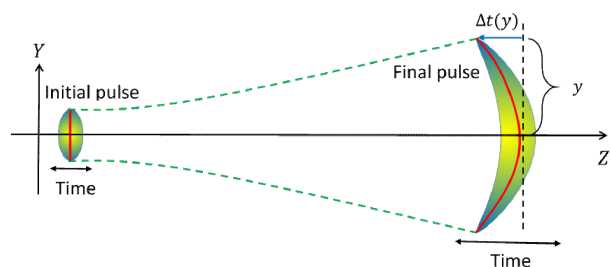


Figure 3.6: Schematic diagram showing the curved pulse front due to the spatio-temporal coupling in free space.

vacuum and  $R(z)$  is the radius of curvature of the wavefront for the central frequency. This is illustrated by schematic plot shown in Fig. 3.6. As a result of this spatio-temporal coupling, the GPB propagating in free space does not remain Gaussian.

By generalizing this off axis delay to any GPB, which is defined by the complex curvature parameter in Eq. (3.2.17) propagating in dispersive media, the generalized off axis delay becomes

$$\Delta t(\tilde{\mathbf{r}}_0) = \frac{n_g z(\tilde{\mathbf{r}}_0)}{c}, \quad (3.2.15)$$

where  $n_g$  is the group index of the medium and  $z(\tilde{\mathbf{r}}_0) = 0.5\Re\epsilon\left(\tilde{\mathbf{r}}_0^T \tilde{\mathbf{Q}}^{-1} \tilde{\mathbf{r}}\right)$  is the wavefront sag for the central frequency for spatio-temporal coordinate  $\tilde{\mathbf{r}}_0 = [x, y, 0]^T$ . If the temporal width of the GPB is very large compared to the off-axis delay, the effect of the off-axis delay can be neglected. For instance, for a GPB with temporal width of  $100fs$  and spatial waist radius of  $1mm$  and wavelength  $\lambda = 800nm$ , the off-axis delay is below 2% of the pulse temporal width for a propagation distance of  $5z_R$ , with  $z_R = 3.927m$  is the Rayleigh length at the central wavelength. Therefore, by decomposing an ultrashort pulse into set of longer pulses in the spectral domain, it is possible to get the curved pulse front without explicitly considering the off-axis delay of individual GPBs.

### 3.2.6 Spatio-temporal and spatio-spectral detectors

The final step in the GPBD method is the computation of the total complex field of the propagated pulse from the phase correct superposition of the contribution of the individual GPB after the propagation. To this end I have defined two detectors, the spatio-temporal and spatio-spectral, which are discussed below.

#### Spatio-temporal detector

The spatio-temporal detector allows for the computation of the total electric field of the final pulse at a given spatial location  $(\mathbf{r}, z)$  and at a given time  $t$ . Consider a GPB propagating along a skew ray direction as shown in Fig. 3.7. The complex spatio-temporal amplitude of the GPB at a target spatial position  $P(X_P, Y_P, Z_P)$  in the global coordinate system and at a given global flight time  $t$  is computed by using the following procedure:

1. Propagate the GPB to the transversal plane which is perpendicular to the propagation direction and passing through the required point of interest  $P$ .
2. Transform the point  $P(X_P, Y_P, Z_P)$  from the global  $(X, Y, Z)$  to the local  $(x, y, z)$

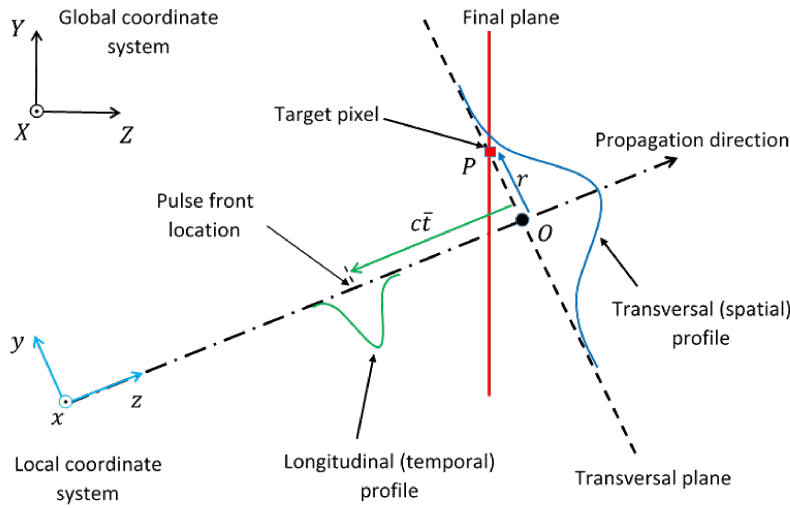


Figure 3.7: A simple 2D geometric construction for computation of the complex amplitude of the GPB on a given target pixel  $P$  at a given flight time.

coordinate of the GPB. The  $x - y$  coordinates give the transversal location  $\mathbf{r}$  of the target point in the local coordinate system.

3. Compute the arrival time of the pulse group to the transversal plane containing the required point  $P$  using  $t_0 = \frac{\Delta_{GPL}}{c}$ , where the  $\Delta_{GPL}$  is the total group path length of the GPB and  $c$  is the speed of light in vacuum.
4. Compute the local temporal coordinate  $\bar{t}_0$ , time in the co-moving reference frame, for the on-axis point from the given global flight time vector and the group arrival time by  $\bar{t}_0 = t - t_0$ .
5. Since  $P$  is an off-axis point, compute the additional delay time  $\Delta t_r$  using Eq. (3.2.15) and determine the corresponding corrected local temporal coordinate  $\bar{t}_r = \bar{t}_0 - \Delta t_r$  for the point of interest  $P$ .
6. Finally compute the complex amplitude of the GPB at spatial position  $P(\mathbf{r}, z)$  computed at specific time  $t$  is given by [44]

$$E(\mathbf{r}, z, t) = \Re \{ U(\mathbf{r}, \bar{t}; z) \exp\{i(\omega_0 t - k_0 \Delta_{OPL})\} \}, \quad (3.2.16)$$

where  $k_0$  is the propagation constant in free space,  $\omega_0$  is the central angular frequency,  $\Delta_{OPL}$  is the total optical path length and  $U(\mathbf{r}, \bar{t}(\mathbf{r}); z)$  is the reduced

complex amplitude of GPB defined in the co-moving time frame given by

$$U(\mathbf{r}, \bar{t}; z) = U_0 \exp \left\{ -\frac{ik_0}{2} \begin{pmatrix} \mathbf{r}^T & c\bar{t}_r \end{pmatrix} \left( \tilde{\mathbf{Q}}^{-1} \right) \begin{pmatrix} \mathbf{r} \\ c\bar{t}_r \end{pmatrix} \right\}, \quad (3.2.17)$$

where  $c$  is the speed of light in vacuum,  $k_0$  is the wave number for the central wavelength in free space,  $\tilde{\mathbf{Q}}^{-1}$  is the  $3 \times 3$  spatio-temporal complex curvature matrix specifying the GPB parameters.

The spatial profile of the propagated pulse whose flight is paused in time can be obtained by directly computing the spatio-temporal profile on a set of spatial points in a 2D plane or 3D space at a given fixed flight time. Similarly, the temporal profile of the pulse at a given spatial point can be computed by performing steps (1-3) once for the given point and then performing steps (4-6) for each temporal coordinates. Hence, the time required for computing the temporal profile of the pulse for  $N$  number of time coordinates at a given point is less than that required for computing the spatial profile of the pulse for  $N$  spatial points at a given time.

### Spatio-spectral detector

The spatio-spectral detector computes the complex amplitudes of the final pulse at a given spatial point  $(\mathbf{r}, z)$  for different spectral component  $\omega$ . In the spatio-temporal domain it is usually difficult to analyze the phase coupling due to the fast oscillation phase profiles of the complex field computed. In such cases, it is advantageous to analyze the pulse in the spatio-spectral domain instead. This is because, the phase coupling in the spatio-temporal domain manifests as the intensity coupling in the spatio-spectral domain which can easily be analyzed from the intensity profile [35]. For instance, the spatial chirp is manifested as the wavefront rotation in the spatio-temporal domain but in the spatio-spectral domain it is directly observed from the tilted pulse front [80].

In principle, the spatio-spectral profiles of a pulse can be computed from the spatio-temporal profiles by performing the temporal FT numerically. However, for ultrashort pulses with large dispersion and large spatio-spectral distortion, the number of temporal sampling points required to correctly sample the fast oscillating temporal phase for the FT becomes too large and hence computationally intensive. In the GPBD method, the total spatio-spectral profile of the pulse is obtained by computing and superposing the spatio-spectral amplitudes of individual GPB after the propagation. The spatio-spectral profiles  $E(\mathbf{r}, \omega; z)$  of each GPB can be computed analytically by performing

the FT of its spatio-temporal amplitude  $E(\mathbf{r}, t; z)$  as [35]

$$E(\mathbf{r}, \omega; z) = \frac{1}{2\pi} \int E(\mathbf{r}, t; z) \exp(-i\omega t) dt. \quad (3.2.18)$$

Now inserting Eq. (3.2.16) into Eq.( 3.2.18), the spatio-spectral profiles becomes

$$E(\mathbf{r}, \omega; z) = \frac{1}{2\pi} \int U(\mathbf{r}, \bar{t}; z) e^{i(\omega_0 t - nk_0 z)} e^{(-i\omega t)} dt, \quad (3.2.19)$$

where  $\mathbf{r} = [x, y]$ ,  $t_0$  is the arrival time of the reference pulse at a given plane and  $\omega_0$  is the central angular frequency. Now replacing  $t = \bar{t} + t_0$ ,  $\omega = \bar{\omega} + \omega_0$  and then taking the constant terms out of the integral, Eq. (??) becomes

$$E(\mathbf{r}, \omega; z) = e^{-i(\bar{\omega} t_0 + nk_0 z)} U(\mathbf{r}, \bar{\omega}; z) \quad (3.2.20)$$

where  $U(\mathbf{r}, \bar{\omega}; z)$  is the FT of the reduced complex amplitude of GPB which is given by

$$U(\mathbf{r}, \bar{\omega}; z) = \frac{1}{2\pi} \int U(\mathbf{r}, \bar{t}; z) e^{-i\bar{\omega} \bar{t}} d\bar{t}, \quad (3.2.21)$$

with  $\bar{t}$  (the time in the co-moving frame) and  $\bar{\omega}$  (the relative angular frequency) being the Fourier conjugate variables. Inserting Eqs. (3.2.16) and (3.2.17) into Eq.(3.2.21) and performing long but straight forward integration, the spatio-spectral profiles finally becomes

$$E(\mathbf{r}, \omega; z) = \frac{\exp\{-i(\bar{\omega} t_0 + k_0 \Delta_{OPL})\}}{c\sqrt{i2\pi k_0 \tilde{Q}_{\tau\tau}^{-1}}} \exp\left[-\frac{ik_0}{2} \begin{pmatrix} \mathbf{r}^T, & \bar{\omega} \end{pmatrix} \tilde{\mathbf{G}}^{-1} \begin{pmatrix} \mathbf{r} \\ \bar{\omega} \end{pmatrix}\right], \quad (3.2.22)$$

where  $\tilde{\mathbf{G}}^{-1}$  is the complex curvature matrix in the spatio-spectral domain which is given by

$$\tilde{\mathbf{G}}^{-1} = \begin{pmatrix} \mathbf{G}_{rr}^{-1} & \mathbf{G}_{r\omega}^{-1} \\ \mathbf{G}_{\omega r}^{-1} & \mathbf{G}_{\omega\omega}^{-1} \end{pmatrix}, \quad \mathbf{G}_{rr}^{-1} = \mathbf{Q}_{rr}^{-1} - \frac{(\mathbf{Q}_{r\tau}^{-1} + \mathbf{Q}_{\tau r}^{-1T})(\mathbf{Q}_{r\tau}^{-1T} + \mathbf{Q}_{\tau r}^{-1})}{4\mathbf{Q}_{\tau\tau}^{-1}}, \quad (3.2.23)$$

$$\mathbf{G}_{\omega\omega}^{-1} = -\frac{1}{k_0^2 c^2 \mathbf{Q}_{\tau\tau}^{-1}}, \quad \mathbf{G}_{r\omega}^{-1} = -\frac{\mathbf{Q}_{r\tau}^{-1}}{k_0 c \mathbf{Q}_{\tau\tau}^{-1}}, \quad \mathbf{G}_{\omega r}^{-1} = -\frac{\mathbf{Q}_{\tau r}^{-1}}{k_0 c \mathbf{Q}_{\tau\tau}^{-1}},$$

with  $\mathbf{Q}_{rr}^{-1}$ ,  $\mathbf{Q}_{r\tau}^{-1}$ ,  $\mathbf{Q}_{\tau r}^{-1}$  and  $\mathbf{Q}_{\tau\tau}^{-1}$  being the elements of the spatio-temporal complex curvature matrix  $\tilde{\mathbf{Q}}^{-1}$ . The results in Eq. (3.2.22) and (3.2.23) are applicable to general case of rotationally non-symmetric GPBs. For the case of rotationally symmetric GPB,

the above equations simplify to those reported in Eq. (12-13) of [35] except for the on-axis complex amplitude factor.

### 3.3 Propagation of field after hard aperture

As mentioned in section 2.3.3, one of the main limitations of the conventional GBD method is that it is not able to accurately model the sharp edge diffraction field after a hard aperture. In this section a novel approach that enables the GBD method to accurately model propagation of field after hard aperture is described. First a new kind of paraxial beam, called the truncated GB, is defined and its propagation equation is derived. Then a method of using the truncated GB in the GBD method to propagate fields after a hard aperture is proposed. Finally the approach is extended for modeling the sharp edge diffraction of an ultrashort pulse truncated by hard aperture.

#### 3.3.1 Truncated Gaussian beams

A truncated GB is defined as a monochromatic beam that is obtained by blocking a part of the fundamental GB with a semi-infinite hard aperture bounded by a straight sharp edge as shown in Fig. 3.8. Mathematically, the reduced complex Gaussian amplitude (without the fast oscillating central phase factor) of the truncated GB shown in Fig. 3.8a is given by

$$U_t(\mathbf{r}) = U_f(\mathbf{r})\theta_x(\mathbf{r}, c_x), \quad (3.3.1)$$

where  $U_f(\mathbf{r})$  is the reduced complex amplitude of the full GPB given in Eq. (3.3.1) and  $\theta_x(\mathbf{r}, c_x)$  is the shifted Heaviside step function given by

$$\theta_x(\mathbf{r}, c_x) = \theta_x(x, y; c_x) = \begin{cases} 1 & x \geq c_x \\ 0 & x < c_x \end{cases}, \quad (3.3.2)$$

with  $c_x$  being the truncation parameter.

For the truncation parameter  $c_x = 0$ , the truncated GB becomes a half GB as shown in Fig. 3.9. The truncated GB has a sharp edge on one side and smooth Gaussian distribution on the other side of its spatial profile. This makes it very suitable for

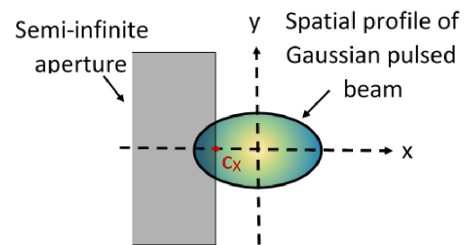


Figure 3.8: Schematic sketch showing the spatial profile of a truncated GB with truncation parameter  $c_x$ .

representing fields with sharp edges after hard apertures. However, the propagation equation used for the GB cannot be directly used for the truncated GBs. Therefore, I have derived the analytical propagation equation

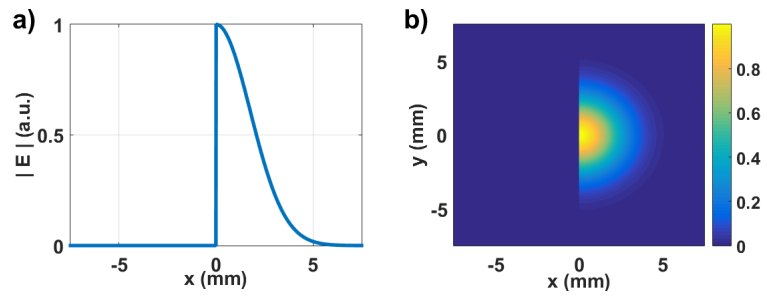


Figure 3.9: The amplitude profile of a symmetrical half GB shown in a) one and b) two-dimensional space.

for the truncated GB from the general Collins integral as discussed below.

### Propagation of truncated Gaussian beams

The propagation of any beam through a general non-rotationally symmetrical paraxial optical system is given by the Collins integral [81]. By using the truncated GB given in Eq. 3.3.1 as the initial field in the Collins integral, I have derived the analytical equation for its propagation through a non-rotationally symmetrical paraxial optical system. The complete derivation is given in Appendix D.1. The final reduced complex amplitude of the truncated GB after the propagation is given by

$$\psi_{2,t}(\mathbf{r}_2) = \frac{1}{2} \operatorname{erfc} \left( \frac{b_x + a_x c_x}{\sqrt{a_x}} \right) \psi_2(\mathbf{r}_2), \quad (3.3.3)$$

where  $\psi_2(\mathbf{r}_2)$  is the reduced field of the full GB after propagation,  $\operatorname{erfc}(\cdot)$  is the complementary error function,  $c_x$  is the truncation parameter, and the other parameters are given by

$$\begin{aligned} a_x &= -(g_{xx} - h^2 g_{yy}), & b_x &= -\frac{1}{2}(g_x - h g_y), & h &= \frac{g_{xy}}{2g_{yy}} \\ g_{xx} &= -\frac{ik}{2} \mathbf{P}_{xx}, & g_{yy} &= -\frac{ik}{2} \mathbf{P}_{yy}, & g_{xy} &= -\frac{ik}{2} (\mathbf{P}_{xy} + \mathbf{P}_{yx}), \\ \mathbf{P} &= \mathbf{Q}_1^{-1} + \mathbf{B}^{-1} \mathbf{A}, & g_x &= ik(\mathbf{B}_{xx}^{-1} x_2 + \mathbf{B}_{xy}^{-1} y_2), & g_y &= ik(\mathbf{B}_{yx}^{-1} x_2 + \mathbf{B}_{yy}^{-1} y_2), \end{aligned} \quad (3.3.4)$$

where  $\mathbf{A}$ ,  $\mathbf{B}$ ,  $\mathbf{C}$  and  $\mathbf{D}$  are the  $2 \times 2$  sub-matrix elements of the system ABCD matrix. From Eq. (3.3.3) it can be seen that the diffraction of a truncated GB is obtained by multiplying the full GB after propagation by a complementary error function with complex parameters. Therefore, an accurate computation of the complementary error function is crucial in determining the sharp edge diffraction of the truncated GB. As the built in complementary error function in Matlab does not support the complex number arguments, an open source Faddeeva package written by Steven G. Johnson [82] has been used for computing the  $\operatorname{erfc}(\cdot)$ .



In the literature, the error functions have been used for the free space diffraction of GBs truncated by circular apertures [83,84]. However, the truncated GBs propagation equations derived in this work considers a semi-infinite hard aperture and can be used for propagation through any paraxial optical systems. In addition to that, the truncated GBs can be combined with the GBD method to enable calculating the diffraction of a given arbitrary monochromatic field from any arbitrarily shaped hard aperture as discussed in the following section.

### 3.3.2 Decomposition of a field after hard aperture

When a given field passes through a hard aperture, the outgoing field will have a sharp edge which is difficult to decompose with the conventional GBD method. To tackle this problem, the sharp edge part of the field is first extracted by using a set of truncated GBs that are placed near the aperture edge and oriented in such a way that their sharp edge side aligns with the sharp edge of the outgoing field. This extracted field with a sharp edge is referred to as the outer subfield in the following section. Usually truncated GBs with truncation parameter of  $c_x = 0$ , also called the half GBs, are used. By subtracting the outer subfield from the given field after the aperture, an inner subfield that has smooth edges is obtained which can be readily decomposed using the conventional GBD method. By propagating the full and truncated GBs through an optical system, the sharp edge diffraction of the field after a hard aperture is computed.

To demonstrate the sharp edge extraction, let us consider a rectangular amplitude profile in one dimension as shown in Fig. 3.10. To represent the sharp edges, two half GBs are placed one at each end of the aperture as shown in Fig. 3.10a. The peak amplitudes of the half GBs are set to the amplitude values of the input field at the edge. By subtracting the two truncated GBs from the rectangular amplitude profile, the central part with a smooth profile is obtained.

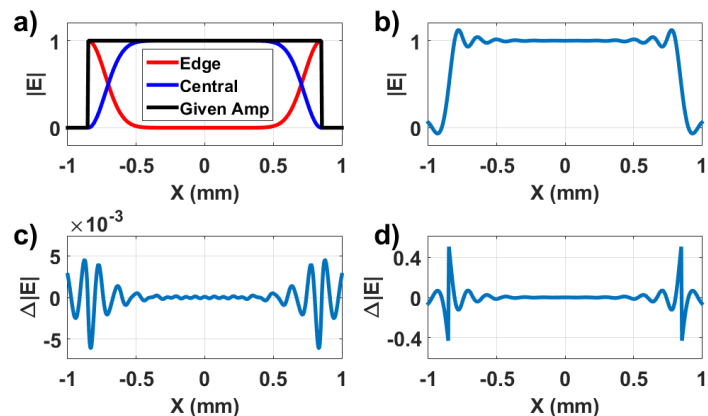


Figure 3.10: a) Extraction of the sharp edges from rectangular amplitude profile in 1D using half GBs. b) The GBD result of the rectangular amplitude without sharp edge extraction. The residual amplitude error for GBD of c) the smooth central amplitude after sharp edge extraction, and d) the rectangular amplitude without sharp edge extraction.

The remaining central field has smooth edges which makes it more comfortable for the application of the conventional GBD. In Fig. 3.10c, the residual amplitude error after performing the GBD of the central smooth amplitude using 30 GBs is plotted. It can be seen that the residual error is in the order of  $10^{-3}$ . However, decomposing the rectangular amplitude directly without extracting the sharp edge using the same number of GBs, a large residual error is observed near the sharp edge as shown in Fig. 3.10(b and d).

In the two dimensional case, the sharp edge part of the field is extracted by using a set of shifted, rotated, and partially overlapping half GBs which are placed around the aperture edge as shown in Fig. 3.11. The truncated GBs are distributed uniformly around the aperture edge and are oriented in such a way that, their sharp edges coincide with a line tangent to the local aperture curve at that point. For apertures with curved edges, such as circular apertures, the straight edges of the half GB do not fit very well with the curved apertures for a small number of half GBs as shown in Fig. 3.11b. Therefore, a relatively large number of truncated GBs with a smaller waist radius are required to improve the accuracy of the curved aperture edge representation. However, reducing the waist radius of the half GB used increases the slope near the edge of the remaining central subfield after the sharp edge extraction. This makes it difficult to apply the GBD for the central subfield. Therefore, in such cases, it is advantageous to use astigmatic truncated GBs, which have smaller waist radius along the axis aligned with the sharp edge and larger waist radius in the other axis as shown in 3.11d.

The amplitude coefficients of the truncated GBs are computed, in the general case, by the least square fitting method using the given amplitude on the aperture edge as the target [53,55]. The coherent superposition of all truncated GBs gives the outer subfield with a sharp edge. The outer subfield with the sharp edge is then subtracted from the total field to get the inner sub-field which has smooth edges. The conventional GBD is then applied to the smooth inner subfield.

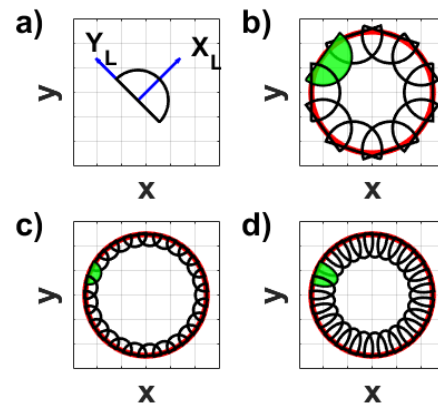


Figure 3.11: a) A single half GB with shifted and rotated local axis. The footprint diagrams of a set of (b)10 non-astigmatic (c) 25 non-astigmatic and (d) 25 astigmatic half GBs used to represent a circular aperture.

### 3.3.3 Spatially truncated Gaussian pulsed beams

In this section, the application of the truncated GBs from the sharp edge diffraction of the monochromatic field is extended to the spatio-temporal propagation of ultrashort pulse after hard apertures. Like in the monochromatic field case, a spatially truncated GPB is first defined as a pulsed beam which is obtained by truncating a GPB by a semi-infinite hard aperture as shown in Fig. 3.8. Mathematically, the reduced complex amplitude (without the fast oscillating central phase factor) of the spatially truncated GPB is given by

$$U_t(\tilde{\mathbf{r}}) = U_f(\tilde{\mathbf{r}})\theta_x(\tilde{\mathbf{r}}, c_x), \quad (3.3.5)$$

where  $\tilde{\mathbf{r}}$  is the spatio-temporal coordinate,  $U_f(\tilde{\mathbf{r}})$  is the reduced complex amplitude of the full GPB given in Eq. 3.3.5,  $c_x$  is the truncation parameter and  $\theta_x(\tilde{\mathbf{r}}, c_x)$  is the shifted Heaviside step function given in Eq. (3.3.2).

The spatially truncated GPB has a sharp edge along the x-axis but has smooth Gaussian distributions along the y-axis and the temporal coordinate. This makes it very suitable for representing ultrashort pulse fields with sharp edges after hard apertures. The spatial profile of the input pulse is decomposed by following a method similar to that discussed in section 3.3.2 for the monochromatic case. However, due to the additional temporal coordinate, the propagation equations derived for the monochromatic truncated GB cannot be used directly for the spatially truncated GPBs. The analytical equation for the propagation of spatially truncated GPB are derived by using the reduced complex field given in Eq. (3.3.5) as an input field to the generalized Huygens diffraction integral given in Eq. (2.3.19). As the spatial profile of the truncated GPB is truncated along x-axis, the  $x$ -component is treated differently from the  $y$  and  $\tau$  components in the Huygens diffraction integral. Hence, the  $3 \times 1$  vector  $\tilde{\mathbf{r}}$  is separated into its  $x$  and  $y - \tau$  components as

$$\tilde{\mathbf{r}} = [x, y, \tau]^T = [x, \mathbf{w}]^T, \quad (3.3.6)$$

where  $\mathbf{w} = [y, \tau]$ . Similarly, the  $3 \times 3$  spatio-temporal complex curvature matrix  $\tilde{\mathbf{Q}}^{-1}$  is separated into  $x$  and  $\mathbf{w}$  components as

$$\tilde{\mathbf{Q}}^{-1} = \begin{pmatrix} \tilde{\mathbf{Q}}_{xx}^{-1} & \tilde{\mathbf{Q}}_{x\mathbf{w}}^{-1} \\ \tilde{\mathbf{Q}}_{\mathbf{w}x}^{-1} & \tilde{\mathbf{Q}}_{\mathbf{w}\mathbf{w}}^{-1} \end{pmatrix}, \quad (3.3.7)$$

where  $\tilde{\mathbf{Q}}_{xw}^{-1} = [\tilde{\mathbf{Q}}_{xy}^{-1}, \tilde{\mathbf{Q}}_{x\tau}^{-1}]$ ,  $\tilde{\mathbf{Q}}_{wx}^{-1} = [\tilde{\mathbf{Q}}_{yx}^{-1}, \tilde{\mathbf{Q}}_{\tau x}^{-1}]^T$  and  $\tilde{\mathbf{Q}}_{ww}^{-1} = \begin{pmatrix} \tilde{\mathbf{Q}}_{yy}^{-1} & \tilde{\mathbf{Q}}_{y\tau}^{-1} \\ \tilde{\mathbf{Q}}_{\tau y}^{-1} & \tilde{\mathbf{Q}}_{\tau\tau}^{-1} \end{pmatrix}$ . All  $3 \times 3$  spatio-temporal system matrix elements ( $\tilde{\mathbf{A}}, \tilde{\mathbf{B}}, \tilde{\mathbf{C}}$  and  $\tilde{\mathbf{D}}$ ) are also separated into  $x$  and  $\mathbf{w}$  components using expressions similar to Eq. (3.3.7). Solving the resulting modified integral by following the long mathematical derivation given in Appendix D.2, the complex amplitude of the propagated field is finally given by

$$U_{2,t}(\tilde{\mathbf{r}}_2) = \frac{1}{2} \operatorname{erfc} \left( \frac{b_x + a_x c_x}{\sqrt{a_x}} \right) U_{2,f}(\tilde{\mathbf{r}}_2), \quad (3.3.8)$$

where  $U_{2,f}(\tilde{\mathbf{r}}_2)$  is the complex field of the full (non-truncated) GPB after propagation,  $\operatorname{erfc}(\cdot)$  is the complimentary error function,  $c_x$  is the truncation parameter and  $a_x$  and  $b_x$  are the complex scalar numbers given by

$$a_x = -(\mathbf{g}_{xx} - \mathbf{h}^T \mathbf{g}_{ww} \mathbf{h}), \quad b_x = -\frac{1}{2}(\mathbf{g}_x - \mathbf{g}_w^T \mathbf{h}), \quad (3.3.9)$$

with

$$\begin{aligned} \mathbf{g}_{xx} &= -\frac{ik_0}{2} \tilde{\mathbf{P}}_{xx}, & \mathbf{g}_{ww} &= -\frac{ik_0}{2} \tilde{\mathbf{P}}_{ww}, & \tilde{\mathbf{P}} &= \tilde{\mathbf{Q}}_1^{-1} + \tilde{\mathbf{B}}^{-1} \tilde{\mathbf{A}}, \\ \mathbf{h} &= -\mathbf{g}_{xw} (\mathbf{g}_{ww} + \mathbf{g}_{ww}^T)^{-1}, & \mathbf{g}_{xw} &= -\frac{ik_0}{2} (\tilde{\mathbf{P}}_{xw} + \tilde{\mathbf{P}}_{wx}), \\ \mathbf{g}_x &= ik_0 (\tilde{\mathbf{B}}_{xx}^{-1} x_2 + \tilde{\mathbf{B}}_{xw}^{-1} \mathbf{w}_2), & \mathbf{g}_w &= ik_0 (\tilde{\mathbf{B}}_{wx}^{-1} x_2 + \tilde{\mathbf{B}}_{ww}^{-1} \mathbf{w}_2), \end{aligned} \quad (3.3.10)$$

where  $\tilde{\mathbf{A}}, \tilde{\mathbf{B}}, \tilde{\mathbf{C}}$  and  $\tilde{\mathbf{D}}$  are the  $3 \times 3$  sub-matrix elements of the spatio-temporal Lin matrix.

As can be seen from Eq. (3.3.8), the diffraction of a spatially truncated GPB is obtained by multiplying the full GPB after propagation with the complementary error function with complex parameters. This is analogous with the propagation of the truncated monochromatic GB given in section 3.3.1. Using Eq. (3.3.8 - 3.3.10), spatially truncated GPB can be propagated through a non-rotationally symmetric and dispersive optical system in paraxial approximation.

### Spatio-temporal coupling in spatially truncated Gaussian pulsed beams

As discussed in section 3.2.5, for ultrashort pulses the spatiotemporal coupling occurs during the propagation through even the simplest optical system, a non-dispersive free space. For full GPBs, the spatio-temporal coupling is taken into account by computing the group delay correction for the off-axis points from the smooth wavefront of

the carrier frequency. However, for spatially truncated GPBs it is not easy to compute the smooth wavefront (unwrapped phase) after propagation. Therefore, spectral decomposition is performed to represent the spatially truncated GPB with a set of temporally longer elementary pulsed beams for which the effects of the off-axis delay can be neglected compared to the temporal width of the elementary GP. The first order spatio-temporal coupling during propagation through optical systems is already taken into account by the propagation equation given above for each spatially truncated GPB.

### 3.4 Extension to vectorial field propagation

The GPBD is an end-to-end wave optical method for propagating ultrashort pulses through real, dispersive, and non-paraxial optical systems in scalar approximation. However, for optical systems significantly affecting the polarization state of the input field such as high numerical aperture focusing systems and system containing polarization filters, the scalar treatment is not sufficient to correctly describe the propagation of the electromagnetic fields. To model the vectorial effects, the GBD method has to be extended to include the polarization state of light. In this section I propose a method to accomplish this by combining the GBD with the three-dimensional polarization ray-tracing method [59]. This combined method is referred to as the polarized GBD method in the following discussions. Although the discussion here is given for the GBD method, there is no reason which limits its application to the GPBD method as well.

In the polarized GBD method, the vectorial input field is decomposed into a set of polarized GBs each with polarization states corresponding to the local polarization of the input field at the GPB center. The polarization of an input field is usually given as Jones vector in the input transversal plane. But, as the GBD is done using a set of GBs which are placed directly on the curved wavefront surface, the polarization states of each GB is determined from the input Jones vectors by using the ray bending argument as follows [85]:

$$\begin{pmatrix} V_x \\ V_y \\ V_z \end{pmatrix} = \frac{1}{\sqrt{S_z}} \begin{pmatrix} \frac{S_x^2 S_z + S_y^2}{S_x^2 + S_y^2} & \frac{-S_x S_y (1 - S_z)}{S_x^2 + S_y^2} \\ \frac{-S_x S_y (1 - S_z)}{S_x^2 + S_y^2} & \frac{S_y^2 S_z + S_x^2}{S_x^2 + S_y^2} \\ -S_x & -S_y \end{pmatrix} \begin{pmatrix} J_x \\ J_y \end{pmatrix}, \quad (3.4.1)$$

where  $J_x$  and  $J_y$  are the components of the Jones vector of the input field on the transversal plane,  $(S_x, S_y, S_z)$  is the unit vector in the direction of the GB. To account for the conservation of power during the ray bending, the amplitude of each component is multiplied with factor of  $\frac{1}{\sqrt{S_z}}$  [86]. This enables the decomposition of general vectorial field with spatially varying polarization states provided that the polarization state change smoothly so that interpolation is valid in the points in between the GB centers.

During the propagation, the total three dimensional polarization matrix of the central ray is traced, using the method discussed in section 2.4.1, in addition to the paraxial spatio-temporal Lin matrix, the total optical and group path length for each GPBs. In the final analysis point, the reduced vectorial field contributions of each GPB is given by

$$\begin{pmatrix} U_{2,x}(\tilde{\mathbf{r}}_2) \\ U_{2,y}(\tilde{\mathbf{r}}_2) \\ U_{2,z}(\tilde{\mathbf{r}}_2) \end{pmatrix} = U_2(\tilde{\mathbf{r}}_2) \begin{pmatrix} V_{2,x}(\tilde{\mathbf{r}}_2) \\ V_{2,y}(\tilde{\mathbf{r}}_2) \\ V_{2,z}(\tilde{\mathbf{r}}_2) \end{pmatrix}, \quad (3.4.2)$$

where  $U_2(\tilde{\mathbf{r}}_2)$  is the complex amplitude of scalar field computed using Eq. (2.3.27),  $V_{2,x}, V_{2,y}$  and  $V_{2,z}$  are the components of the final polarization vector computed using Eq. (2.4.5). The total vectorial field of the propagated ultrashort field in the target analysis point is computed by phase correct superposition of each polarization components separately.

## 4. Validations and Application Examples

In this chapter several example calculations are presented for validating the methods proposed in chapter 3 and show their application in modeling the wave optical propagation of both monochromatic and pulsed beams through optical systems.

### 4.1 Monochromatic beam propagation

In this subsection the analytical propagation equation of the truncated GB is first validated and then examples are presented to show its application in modeling the sharp edge diffraction of the field after hard apertures both in Fresnel and the far-field region. Following that examples are given to demonstrate the application of the modified GBD method in the propagation of fields with strongly curved wavefronts. Finally, the polarized GBD method is validated by calculating the vectorial field in the focal plane of an ideal high numerical aperture focusing system. Most of the results presented in this subsection have already been published in the peer-reviewed journals [53, 62, 65].

#### 4.1.1 Propagation of single truncated Gaussian beam

Considered the propagation of two truncated GBs shown in Fig. 4.1(a and b), which are formed by splitting a single GB with plane wavefront, waist width of  $w_x = w_y = 5mm$  and wavelength of  $\lambda = 0.5\mu m$  at line  $x = 4mm$ . The truncated GBs are propagated in free space using the analytical propagation formula presented in section 3.3.1. Figure 4.1 shows the final amplitude profiles of the truncated GBs after propagating in free space by a distance of  $z = 0.1Z_R$ , where  $Z_R = 157.08mm$  is the Rayleigh length of the GB.

The amplitude profiles of the propagated subfields shown in Fig. 4.1(c and d) have the typical oscillations coming from the sharp edge diffraction. Especially, from Fig. 4.1c, it can be seen that the maximum value of the amplitude is shifted from the edge of the geometrical shadow towards the illuminated region. This is the typical diffraction pattern of Fresnel diffraction at a semi-infinite plane bounded by straight sharp edge [1]. To verify the propagation results, the results in Fig. 4.1d have been compared with that obtained by propagating the truncated GBs using the spectrum of plane wave (SPW) method using  $1024 \times 1024$  sampling points as shown in Fig. 4.2.

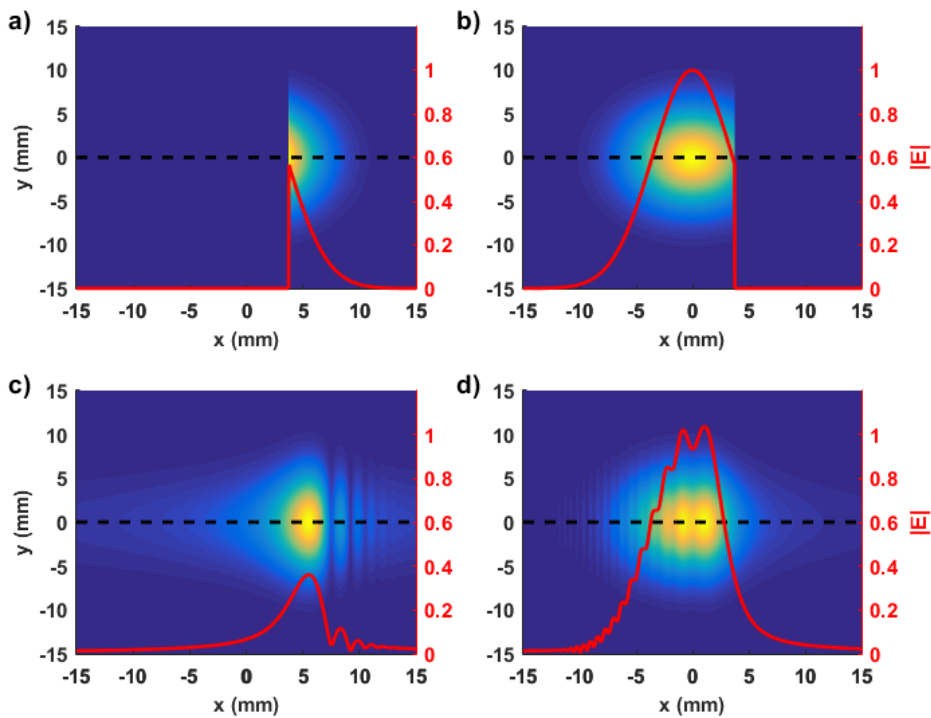


Figure 4.1: (a-b) A single GB divided into two asymmetrical half GBs with sharp edges. (c-d) The amplitude profiles after the propagation of the half GBs shown in a and b respectively by a distance of  $z = 0.1Z_R$ .

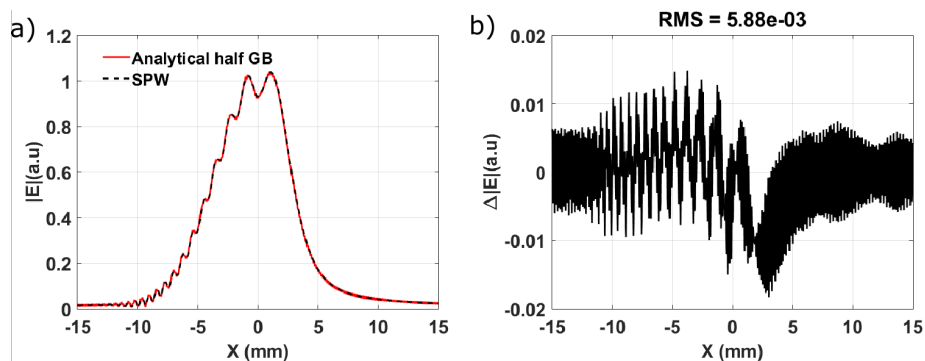


Figure 4.2: a) The cross-sectional amplitude of the propagated field in Fig. 4.1d together with that computed using the SPW method, b) The difference in the final amplitude propagated using the two methods.

As can be seen from Fig. 4.2, the root mean square value of the difference in the final amplitude using the analytical truncated GB propagation and the SPW method is below 0.5%.

To see the effect of increasing the propagation distance, I have performed the propagation to different distances in the range of  $0.1Z_R$  to  $3Z_R$ . As the propagation distance increases, the amplitude profiles of the truncated GB become wider with reduced peak value and reduced oscillations due to sharp edge diffraction as shown in Fig. 4.3. As



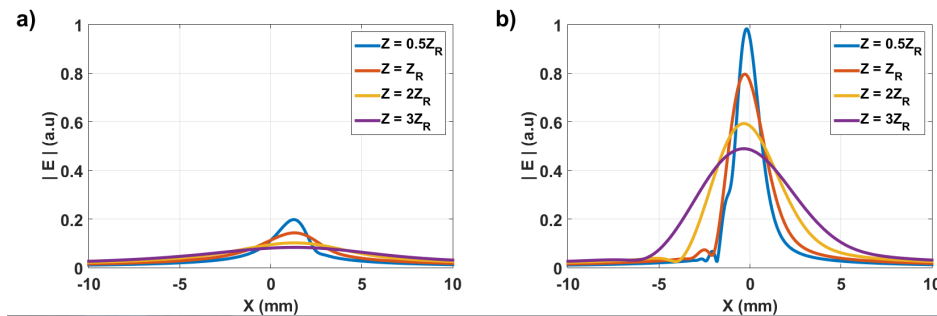


Figure 4.3: The x-cross-sectional plots of the amplitude profiles of the subfields shown in Fig. 4.1 (a and b) respectively for different propagation distances.

the two truncated GBs are initially part of a single GB, the coherent superposition of the two truncated GBs after the propagation also gives back the smooth GB. To demonstrate this, the x-cross-sectional plots of the resulting GB after propagation distances of  $z = 0.5Z_R$  and  $z = 3Z_R$  have been plotted in Fig. 4.4. I have also shown the amplitude profiles obtained by the direct analytical propagation of the full GB to further verify the results. The RMS value of the residual error computed for both cases

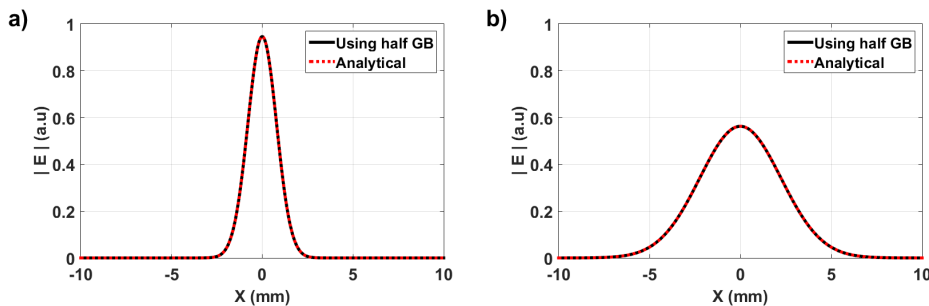


Figure 4.4: The comparison of the x-cross-section of the amplitude profile of the final propagated GB obtained as a coherent superposition of the two asymmetrical half GBs after propagation with the analytical result for propagation distances of a)  $z = 0.5Z_R$  and b)  $z = 3Z_R$ .

in Fig. 4.4 is in the order of  $10^{-16}$  which is nothing but numerical error. This shows that the analytical propagation formula of the truncated GB derived in this work is both accurate and self-consistent. As discussed in section 3.3.2, the truncated GBs can be used to extend the application of the conventional GBD method to modeling sharp edge diffraction of a general non-Gaussian input field after hard aperture. This is demonstrated in the following example.

#### 4.1.2 Fresnel diffraction of the field after a hard aperture

In this example, I apply the modified GBD method to model the propagation of a plane wave with  $\lambda = 0.5\mu\text{m}$  truncated by a hard aperture which is composed of a semi-circle

with a radius of  $a = 5\text{mm}$  and a half square with side length of  $2a = 16\text{mm}$  as shown in Fig. 4.5a. The outer sharp edge is first extracted using 70 partially overlapping

half GBs distributed uniformly around the hard aperture edge as shown in Fig. 4.5b. In addition to the half GBs, two quarter GBs (see Appendix D.1) indicated in Fig. 4.5b with blue color have also been used for better accuracy at the two right-angled sharp corners. The use of quarter GB makes sense only if the aperture has a right angle edge as shown in this section. The superposition of the truncated GBs gives the sharp edge part of the given amplitude profile after the aperture as shown in Fig. 4.5c. Subtracting the outer

subfield from the given amplitude after aperture, the inner subfield which is shown in Fig. 4.5d has been obtained. The inner subfield, which has smooth edges, is then decomposed into  $25 \times 25$  GBs using the conventional GBD method.

Once the field after hard aperture is divided into the two subfields shown in Fig. 4.5 (c and d), they are propagated independently through the system and coherently superposed in the final plane. I have calculated the diffraction pattern on the target plane which is located at a distance of  $z = 10\text{m}$  from the hard aperture. The resulting Fresnel number of the diffraction setup is given by  $N_F = a^2/(\lambda z) = 12.8$ . This indicates that the amplitude profile of the propagated field will have a small number of oscillations which in turn makes the graphical comparison of the results easier. On the target plane, the final propagated amplitudes profiles shown in Fig. 4.6 have been obtained for the two subfields. From the results shown in Fig. 4.6, it can be seen that after the propagation the sharp edge part has an oscillating amplitude due to the sharp edge diffraction, whereas the central smooth part is not significantly changed during the propagation. The total propagated field shown in Fig. 4.7a is obtained by the

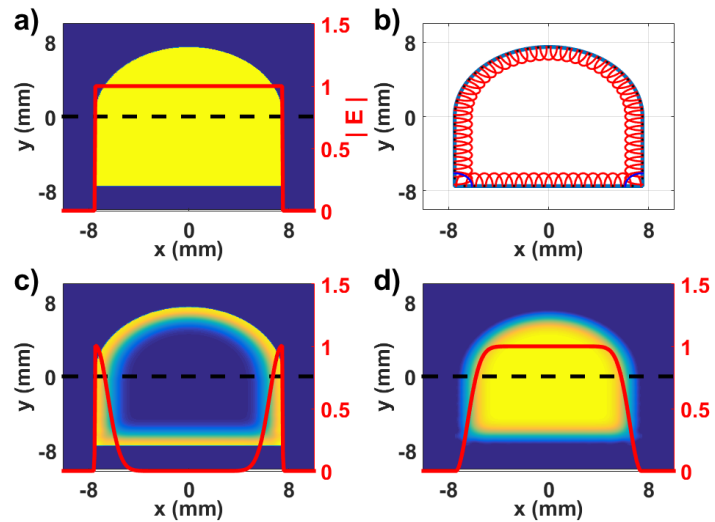


Figure 4.5: Sharp edge extraction using truncated GBs in 2D. a) The input uniform amplitude after the hard aperture, b) the footprint of the truncated GBs, c) the extracted sharp edge amplitude profile, and d) the remaining central amplitude profile with smooth edges. The red line plots over the amplitude profiles show the x-cross-sectional view.

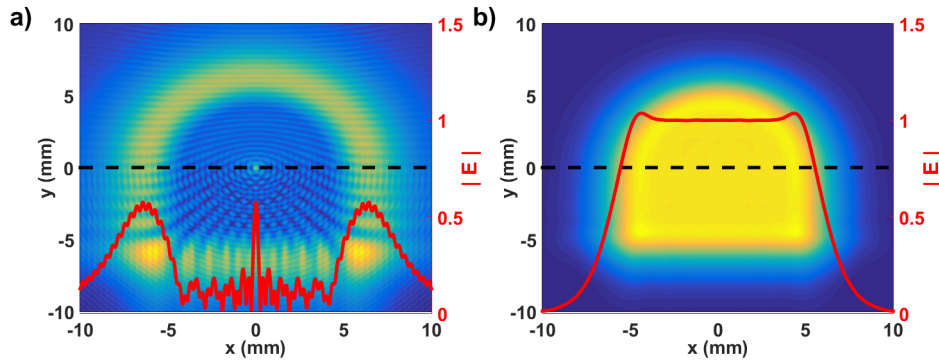


Figure 4.6: The amplitude profiles of the a) outer sharp edge subfield b) the inner smooth subfield after propagating a distance of  $z = 10m$  in free space.

coherent superposition of the two subfields. From Fig. 4.7a it can be seen that, the

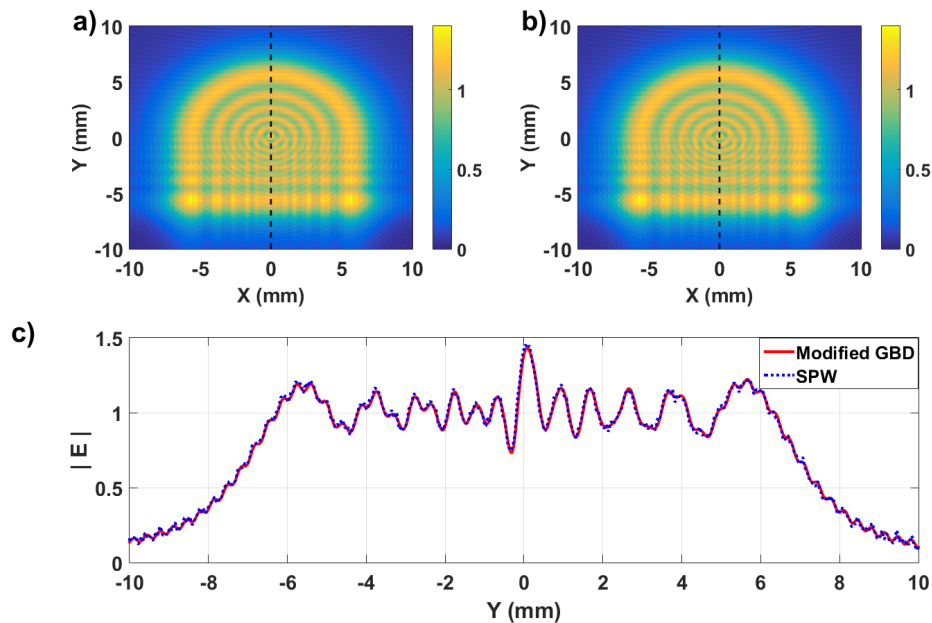


Figure 4.7: The amplitude profiles of the final propagated field using a) the modified GBD method b) the angular spectrum method. c) The y-cross-sectional view of the final propagated amplitude profiles.

amplitude profile of the propagated field is not symmetrical along the y-cross-section due to the fact that the aperture is not rotationally symmetric. In order to validate the results, I have performed the free space propagation of the same input field by the same distance using the angular spectrum method using  $1024 \times 1024$  sampling points. The resulting amplitude profile on the final plane is shown in Fig. 4.7b respectively. From the comparison of the y-cross-sectional amplitude shown in Fig. 4.7c, it can be seen that the result computed using the proposed method agrees with that obtained from the angular spectrum method. The root mean square of the residual amplitude

error is about 1.2%. The reasons for the observed slight disagreement are twofold: firstly, the angular spectrum method requires an extremely large number of sampling points to accurately model the diffraction from such sharp edges, which are handled by the analytical formula in the GBD method. Secondly, there is always a residual error during the GBD of the central subfield.

The application of the modified GBD method is not limited to the propagation of the field with initial plane wavefronts. In the following example its application for initial fields with curved wavefronts is demonstrated.

### 4.1.3 Converging spherical wavefront after circular aperture

In this example, I calculate the ideal point spread function by propagating a converging spherical wavefront after circular aperture to the focal plane using the modified GBD method. For the calculation, a converging wavefront with a radius of curvature  $R = 30\text{mm}$ , wavelength  $\lambda = 0.5\mu\text{m}$ , and uniform amplitude truncated by a circular aperture with a semidiameter  $a = 18\text{mm}$  has been considered.

As discussed in chapter 3, a set of GBs with non-zero initial curvatures together with truncated GBs are used for the decomposition of a given field with a curved wavefront after a hard aperture. To investigate the effect of the number of GBs and the overlap factor used on the residual errors of the GBD, I have decomposed the input field discussed in this subsection using a different number of GBs and different overlap factors. The RMS value of the resulting residual amplitude error and the residual phase are shown in Fig. 4.8. In all cases, the GBs used were allowed to have a non-zero initial curvature. It can be seen that, as the number of GBs used increase the

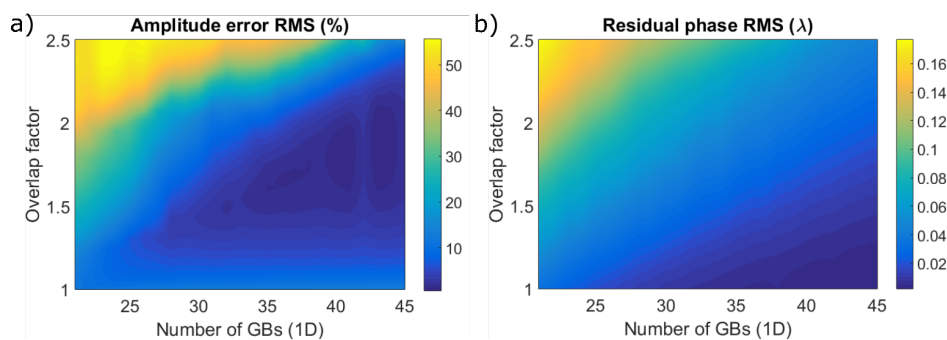


Figure 4.8: The dependance of a) the residual amplitude error and b) the residual phase on the number of GBs and the beam overalp factor used for the decomposition.

residual errors decrease in both amplitude and phase. However, for the overlap factor, the minimum amplitude error is obtained by using a value between 1.5 and 2. Whereas,

the residual phase error increases with the overlap factor. This is because as the overlap factor increases for a given number of GBs, the width of individual GB becomes large and hence the accuracy of the local quadratic approximation reduces. For the following analysis, we have used a grid of  $45 \times 45$  GBs and an overlap factor of 1.6.

To demonstrate the advantage of the decomposition method proposed in chapter 3, I have also performed the GBD of the given field using three different approaches. In the first and second approaches, a set of  $45 \times 45$  GBs with zero and non-zero initial curvatures, respectively, are used without employing the truncated GBs for the sharp edge modeling. In the third approach, a set of  $45 \times 45$  GBs with non-zero initial curvatures and 70 truncated GBs are used to decompose the field with sharp edge after the aperture. In all cases the initial GBs are distributed directly on the wavefront surface and with directions computed from the local wavefront surface normal. The results of the three different decomposition approaches are shown in Fig. 4.9.

As it can be seen from Fig. 4.9 (a-c), the decomposition without using initial curvature of the GBs gives very lousy result and the decomposition has residual large error. This is because GBs with zero curvature cannot accurately represent the curved wavefront of the given field. Although, the decomposition accuracy is improved by using GBs with non-zero initial curvatures, as shown in Fig. 4.9 (d-f), there still exists significant residual error near the sharp edge of the amplitude profile. By additionally using a set of truncated GBs for handling the field near the sharp edge, the decomposition accuracy has been significantly improved with the rms value of about 1.48% and  $0.015\lambda$  for the amplitude error and the residual phase, respectively, as shown in Fig. 4.9 (g-i).

After the initial decomposition, the complex amplitude of the focal field is obtained by propagating the GBs individually and performing the coherent superposition at the focal plane. The point spread function is then computed as the square of the complex field amplitude. Since the Fresnel number is very large ( $N_F = a^2/(\lambda z) = 5400 \gg 1$ ), the focal shift is negligible and the real focus of the converging field occurs on the geometrical focal plane [87]. Hence, the ideal point spread function computed using the analytical Airy pattern formula can be used for comparison of the results. In Fig. 4.10, I have plotted the cross-sectional view of the point spread function computed using the analytical Airy pattern formula, the FT based scalar far-field propagator (with a sampling grid size of  $[2048 \times 2048]$ ), the conventional GBD method (the first approach in Fig. 4.9) and the modified GBD method using the truncated GBs (the

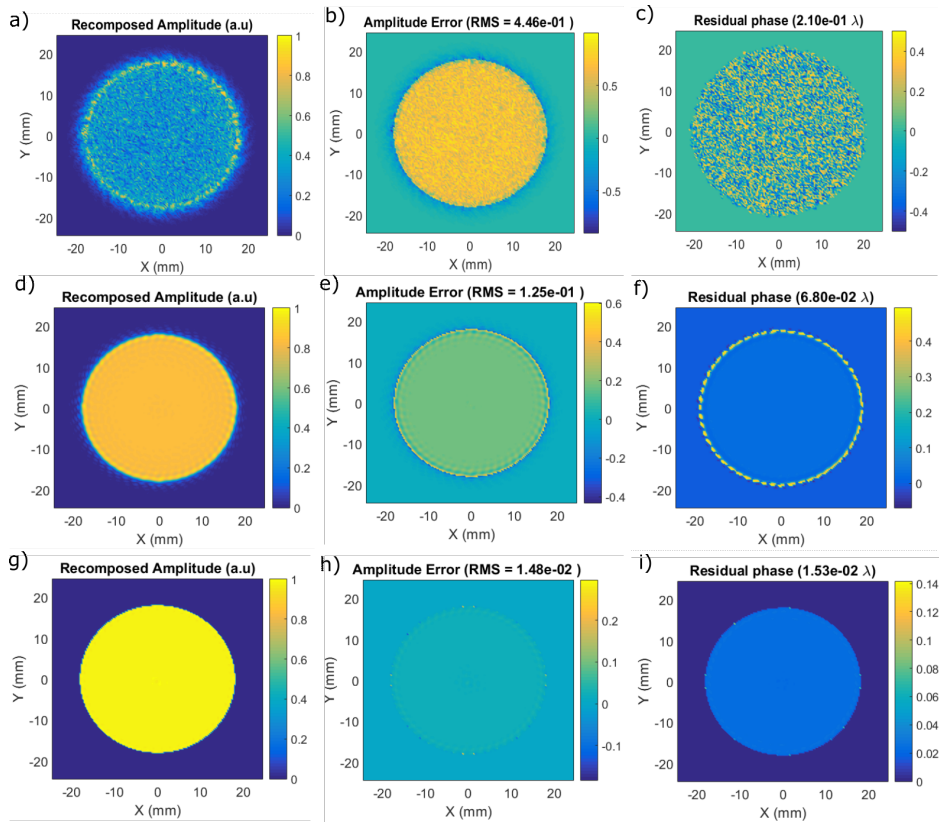


Figure 4.9: The recomposed amplitudes and the corresponding residual amplitude and phase errors after the decomposition of spherical wavefront with radius of curvature

$R = 30\text{mm}$  after circular aperture with a semidiameter  $a = 18\text{mm}$  using three decomposition approaches. The results shown in (a)-(c) are obtained by using a set of GBs with zero initial curvatures; those shown in (d)-(f) are obtained by using a set of GBs with non-zero initial curvatures; and for the results shown in (g)-(i), truncated GBs are used to handle the sharp edge of the field after the hard aperture.

third approach in Fig. 4.9). From Fig. 4.10 it can be seen that the results using all the methods agree in the first few rings. However, they start to deviate as one goes further from the center peak. Since the conventional GBD method cannot accurately model the sharp edge of the field after the hard aperture, its result departs largely and quickly from the analytical solution. The intensity of the focal field obtained from the FT based scalar far-field propagator also gradually departs from the analytical reference result. This is due to the fact that with finite sampling grid size limits the maximum spatial frequency propagated from the sharp edge diffraction. However, the result obtained using the modified GBD method strongly agrees with the analytical result for more than 100 rings as shown in Fig. 4.10 with the residual RMS error of  $1.2 \times 10^{-4}$ . The main reason for such high accuracy is that the sharp edge diffractions are accurately handled with the analytical propagation formulas of the truncated GBs

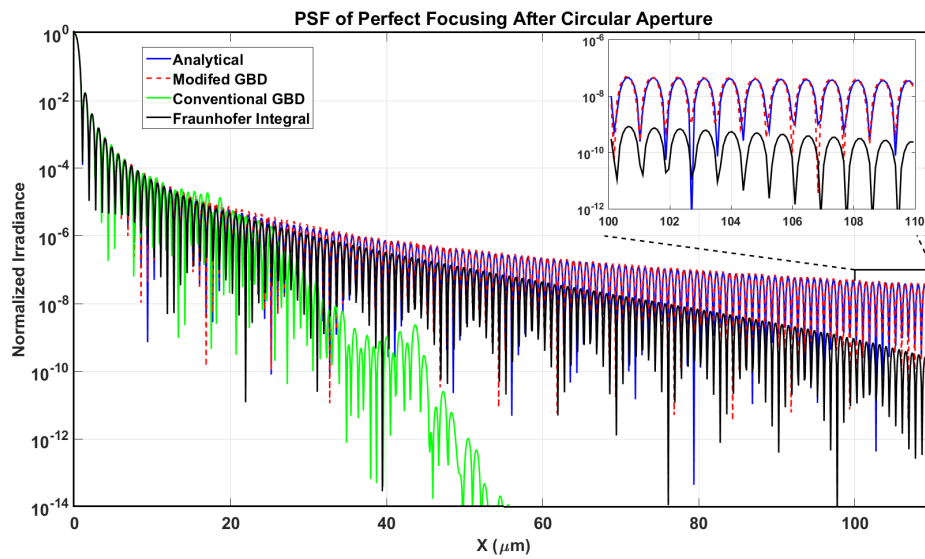


Figure 4.10: Point spread function comparison for a perfect lens with a circular clipping aperture (Airy pattern)

presented in this work.

For focusing setup with a very low Fresnel number, the diffraction of the outgoing converging spherical waves from circular aperture results in the significant shift of the point of maximum intensity from the geometrical focus [87, 88]. The modified GBD method can be directly applied to calculate the diffraction of the spherical wave in focusing setups with very low Fresnel number as long as the scalar diffraction approximation holds. To observe the focal shift phenomena, I have computed the on-axis amplitude for a converging spherical wave with a wavelength of  $0.5\mu\text{m}$  after a circular aperture of  $0.1\text{mm}$  for different Fresnel numbers, achieved by changing the radius of curvature  $R$  (hence the numerical aperture). For a focusing setup with Fresnel number  $N_F = 1$ , obtained by using  $R = f = 20\text{mm}$ , the focal shift  $\Delta f$  becomes as large as 40% of the focal length  $f$  as it can be seen from Fig. 4.11a which shows the on-axis intensity profile near the focal plane. As the Fresnel number of the focusing setup increases, the resulting relative focal shift reduces as shown in Fig. 4.11b. The results obtained using the modified GBD method are similar to those reported in the literature previously using other classical diffraction calculation methods [87–89].

#### 4.1.4 Propagation of field with non-spherical wavefronts

One of the main application area of the modified GBD method is in the propagation of electric field with strongly curved and non-spherical wavefronts. In the conventional FT based methods, the propagation of such kind of fields is computationally intensive due

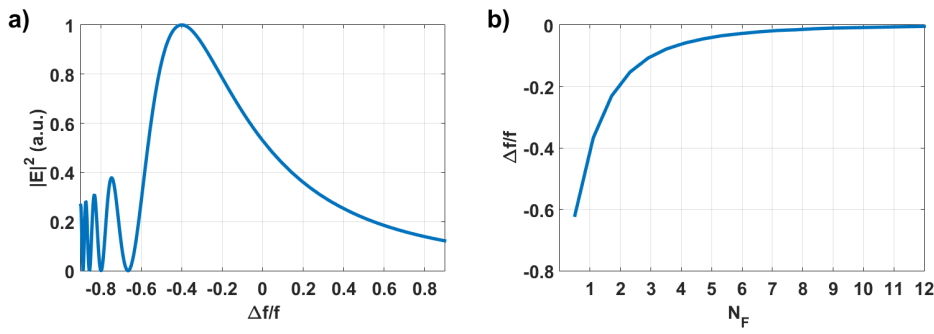


Figure 4.11: a) The on-axis intensity of converging spherical wave with Fresnel number of  $N_F = 1$ . b) The relative focal shift of a converging spherical wave using focusing setups with different small Fresnel numbers.

to the huge number of sample points required for sampling the fast oscillating spatial phase in the initial plane. In this section, the power of the modified GBD method is demonstrated by propagating converging wavefront with large spherical aberration and a cone shaped wavefront which is usually obtained after axicon components.

### Field with large spherical aberrations

Consider the propagation of a field with a non-spherical wavefront which is given by

$$\phi(x, y) = \frac{(1/R)(x^2 + y^2)}{1 + \sqrt{1 - (1/R)^2(x^2 + y^2)}} + c_9 (1 - 6(x_n^2 + y_n^2) + 6(x_n^2 + y_n^2)^2), \quad (4.1.1)$$

where  $R$  is the radius of curvature of the spherical part,  $c_9$  is the coefficient of the 9<sup>th</sup> term of the Zernike fringe polynomial (primary spherical aberration with defocus) and  $(x_n, y_n) = (x/r_n, y/r_n)$  are the normalized  $(x, y)$  coordinates with the normalization radius  $r_n$ . For the wavefront parameter, the radius of curvature  $R = 40\text{mm}$  and Zernike fringe coefficient of  $c_9 = 100\lambda$  with normalization radius  $r_n = 10\text{mm}$  have been used. The amplitude profile of the field is defined by a super Gaussian profile with diameter of  $9\text{mm}$  and super Gaussian order of 50 for smooth edges. The given

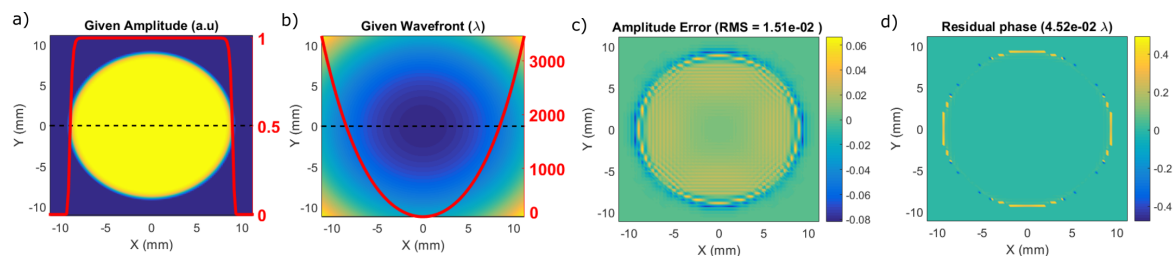


Figure 4.12: a) The amplitude profile on the wavefront surface, and b) the wavefront profile of the input field. The cross sectional plots along the black dotted lines are shown using the red line with the values indicated in the right axis. c) The amplitude error and, d) the residual phase error after the GBD.



amplitude and wavefront profiles are shown in Fig. 4.12 (a and b). The given input field has been decomposed into a set of a uniformly distributed  $50 \times 50$  GBs using the method discussed in section 3.1. The residual errors after the decomposition are shown in Fig. 4.12 (c and d). As it can be seen from Fig. 4.12(b and c), the root mean square values of the residual amplitude and phase error after the decomposition are 1.51% and  $0.045\lambda$  respectively. The residual errors are concentrated around the steep edge of the given amplitude profile.

By propagating the decomposed field in free space, the field in the focal region is obtained whose cross-sectional intensity distribution is shown in Fig. 4.13. From the

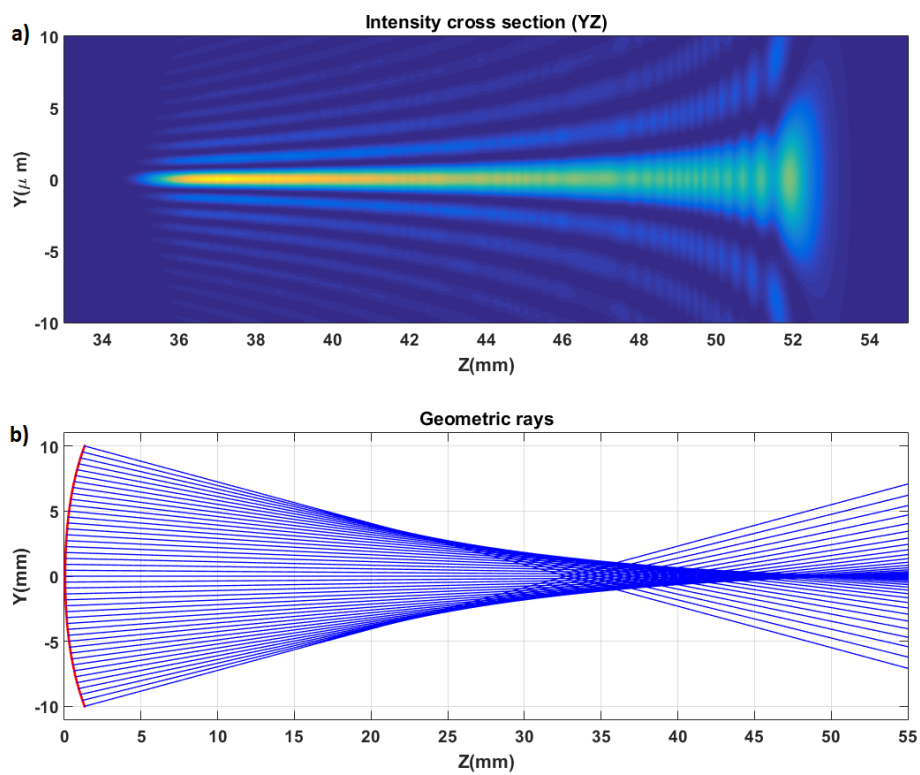


Figure 4.13: (a) The YZ-cross section of the intensity profile computed in the focal region of the converging wavefront with spherical aberration  $c_9 = 100\lambda$ , (b) the geometric rays traced from the wavefront to the focal region.

result in Fig.4.13(a) it can be seen that the width of the central lobe increases as one goes from the left side, marginal focus, to the right, paraxial focus, along the z-axis. This is due to the fact that the deflection angle of the rays decreases, hence decreasing the numerical aperture, as one goes from the marginal to the paraxial focal point.

### Field with cone shaped wavefront

As a second example to demonstrate the application of the modified GBD method, the propagation of a cone shaped wavefront, which are usually created by axicon, is considered. The cone-shaped wavefront results in a line focus (Bessel beam) in the focal region where the rays intersect with each other. Consider an input field with a

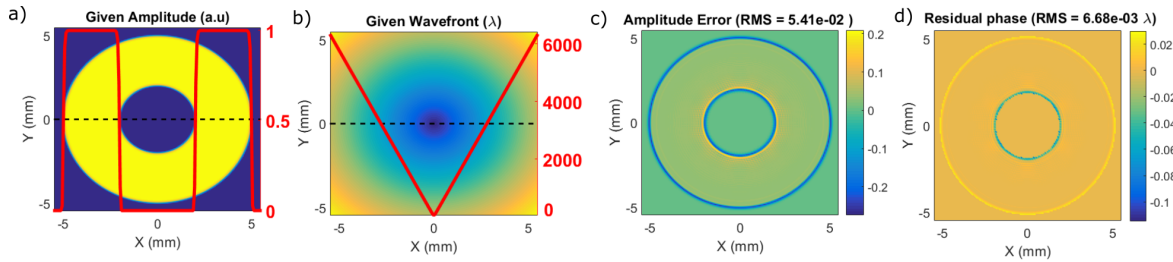


Figure 4.14: The same as Fig. 4.12 but now for the case of the input field with a cone shaped wavefront.

cone-shaped wavefront with a half cone angle of 60 deg and a uniform amplitude profile defined in a circular ring with an inner and outer radius of  $2mm$  and  $5mm$ , respectively with smooth super-Gaussian edge (with order of 50) as shown in Fig. 4.14 (a and b). The ring-shaped amplitude profile makes sure that there is finite working distance from the wavefront and the region where the rays start to cross forming the line focus, which is often desired in practical applications. The ring-shaped input amplitude is also an advantage for the GBD method as it avoids the decomposition of the wavefront near the apex of the cone where the curvature is extremely large which requires a large number of GBs for the correct decomposition.

The given ring shaped field has been decomposed into a set of about  $65 \times 65$  beams inside circular aperture of radius  $5mm$  distributed in a Hexapolar pattern using the method discussed in section 3.1. The residual errors of the amplitude profile computed on the wavefront surface after the decomposition are shown in Fig. 4.14 (c and d). As it can be seen from Fig. 4.14 (c and d), the root mean square value of the amplitude error after the decomposition is around 5.4% and that of the residual phase is about  $0.0067\lambda$  with largest contributions coming from the inner edges.

Finally by performing the free space propagation of the decomposed field, a line focus field is obtained whose YZ-cross sectional intensity profile is shown in Fig. 4.15. From Fig. 4.15 (a and b) it can be seen that the line focus beam created extends from about  $z = 4.3mm$  to  $z = 11.8mm$  along the axis. The peak intensity on the axial intensity profile is on the right end due to the uniform illumination of the ring aperture. By

using a Gaussian-shaped illumination it is possible to shift the peak to the center of the axial intensity profile.

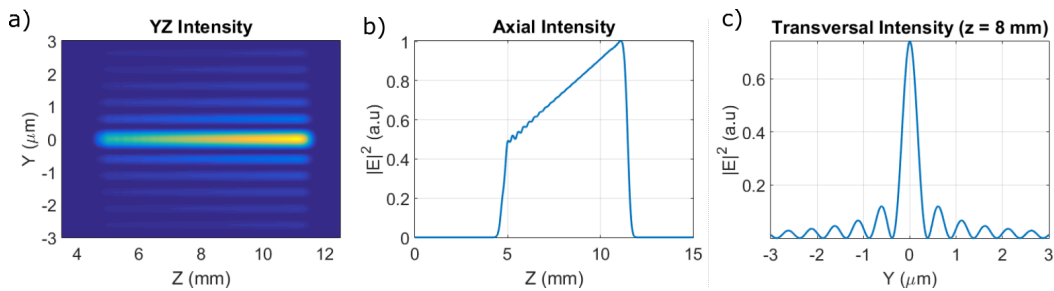


Figure 4.15: The normalized intensity plots calculated by propagating the cone shaped wavefront with uniform ring illumination using the GBD method in free space : a) The YZ cross section, b) the axial profile for  $x = y = 0$  and c) the transversal profile at  $z = 8mm$ .

#### 4.1.5 Vectorial field propagation in a high NA focusing

In this section the application of polarized GBD method for the propagation of a vectorial field in a high NA focusing system like the one shown in Fig. 2.8 is demonstrated. Consider focusing of an x-polarized input field with a wavelength of  $830nm$  and having a uniform amplitude truncated by a circular aperture with a radius of  $2mm$  by an ideal focusing system with  $f = 2.2mm$  in air (numerical aperture,  $(NA) = 0.9091$ ). At the exit pupil, the system has a perfect converging spherical wave with the radius of curvature  $R = f = 2.2mm$ . To propagate the polarized field into the focal region, the GBD of the initial spatial profile is performed directly on the wavefront sphere at the exit pupil using  $30 \times 30$  full and 70 truncated GBs as discussed in section 3.3.2 above. The truncated GBs are used to represent the sharp edge part after the circular aperture. Since the polarization state of the input field is given on the entrance pupil plane of the system, the polarization vectors of each GBs on the exit pupil sphere are computed from the input Jones vector by using the relation given in Eq. (3.4.1). Finally, by propagating the individual GBs to the focal plane and performing the coherent superposition of each vectorial component, the

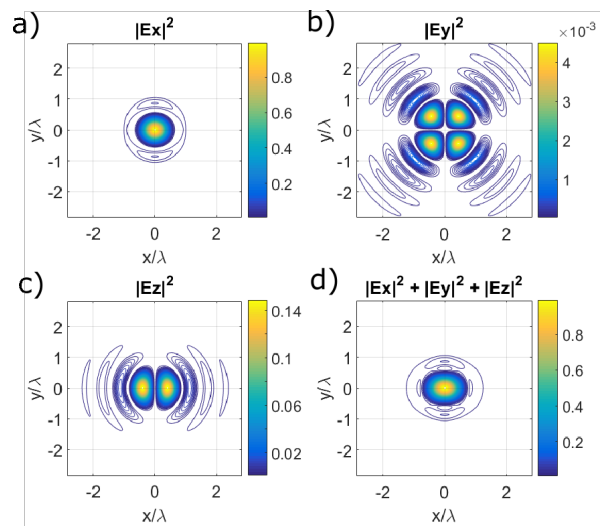


Figure 4.16: The vectorial field components at the focal plane computed by the polarized GBD method.

focal plane vectorial field shown in Fig. 4.16 is obtained.

As can be seen from Fig. 4.16, although the input field is purely x-polarized, the field in the focal plane has significant z-polarization and small y-polarization component in addition to the x-polarization component due to high bending of rays. This also results in the non-rotationally symmetric total intensity point spread function as shown in Fig. 4.16d.

To validate the result, the vectorial focal plane field has been computed by using the vectorial Debye diffraction integral. The resulting vectorial focal fields are shown in Fig. 4.17. Comparing the result in Fig. 4.16 and Fig. 4.17, it can be seen that the result obtained using the polarized GBD agrees with that computed using the vectorial Debye integral. For more quantitative comparison the cross sectional view of the total intensity profiles obtained by both methods are plotted in Fig. 4.18. From the result in Fig. 4.18 it can be seen that the root mean square error of the results obtained by the polarized GBD method is below 0.5% which can further be reduced by increasing the number of GBs used for the decomposition.

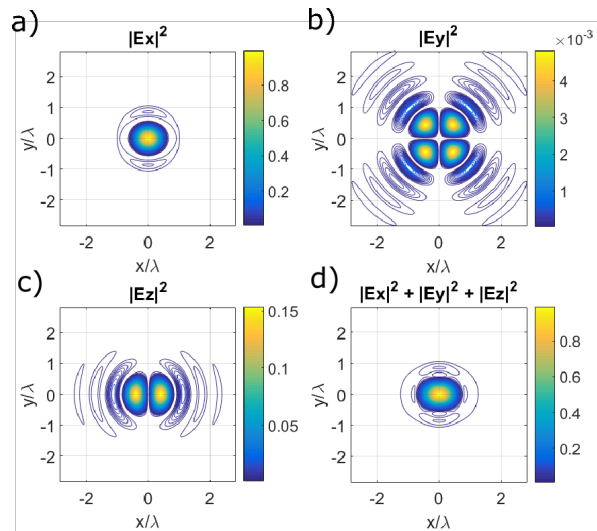


Figure 4.17: The vectorial field components at the focal plane computed by the vectorial Debye integral.

## 4.2 Ultrashort pulse propagation

In this subsection, the calculation results for validating and demonstrating the application of the GPBD method for the propagation of ultrashort pulses through optical systems are presented. First, the methods of computing the free space spatio-temporal coupling of a single GPB in free space and the analytical propagation equation of the spatially truncated GPBs are validated. Then the systematic method of decomposing an arbitrary spectral profile into a set of chirped Gaussian pulses is demonstrated. Finally, several examples are presented to demonstrate the applications of the GPBD method in modeling the sharp edge diffraction of ultrashort pulses after a hard aperture and the pulse propagation through different optical systems. The results given in

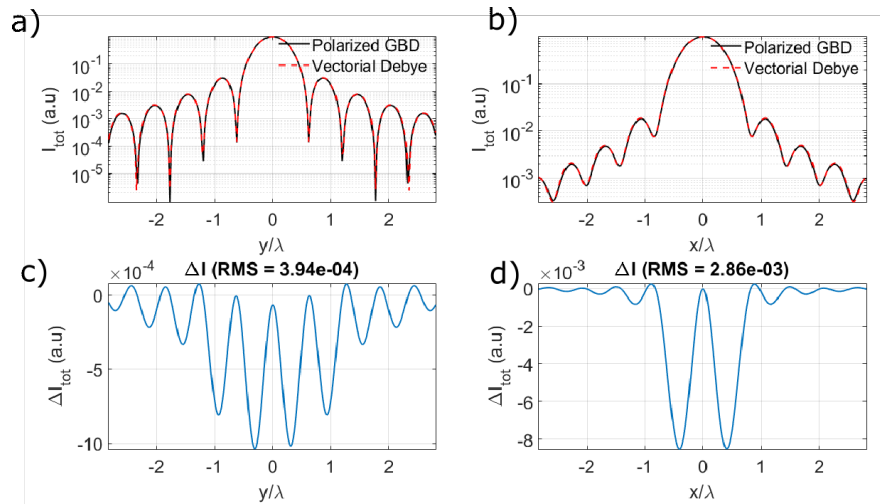


Figure 4.18: (a) The  $y$ - and (b) the  $x$ - cross-sectional plots of the total intensities shown in Fig. 4.16d and Fig. 4.17d in logarithmic scale. (c,d) The difference between the intensity values computed using the polarized GBD method and the vectorial Debye integral method for the corresponding cross-sections.

this subsection have already been published in the peer-reviewed journals [63, 64, 90].

### 4.2.1 Spatio-temporal coupling of Gaussian pulsed beam in free space

In this example I validate the method proposed in section 3.2.5, for including the spatio-temporal coupling in free space into the Lin matrix-based propagation of the single GPB. Consider a single GPB with spatial and temporal width of  $\sigma_r = 100\mu\text{m}$  and  $\sigma_t = 50\text{fs}$ , respectively and central wavelength of  $\lambda_0 = 800\text{nm}$ . Propagating the GPB in free space to final transversal planes which are located at distances of  $z = 0, 5Z_R, 50Z_R$  ( $Z_R = 39.27\text{mm}$  is the Rayleigh length for the central wavelength) from the initial plane, the final spatio-temporal profiles obtained are shown in Fig. 4.19. As can be seen from the  $y - t$  amplitude profiles shown in Fig. 4.19, the pulse front

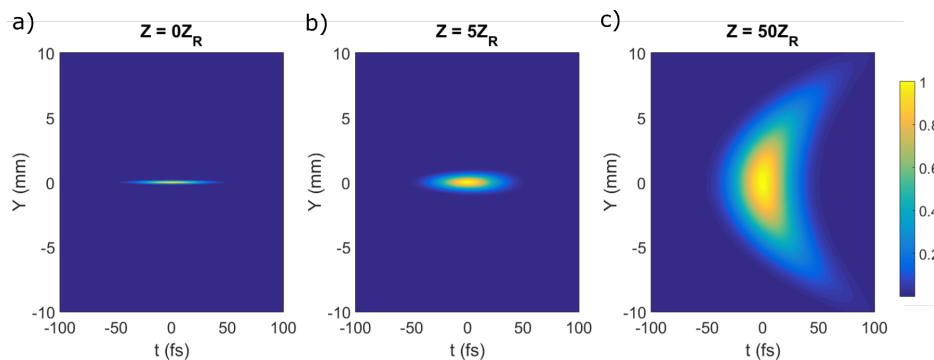


Figure 4.19: The spatio-temporal amplitude profiles of an ultrashort pulse propagating different distances in free space.

gets distorted (curved) even in the free space propagation which becomes significant for longer propagation distances. This curved pulse front is due to the fact that for a given transversal plane the pulse arrives at the on-axis points earlier than the off-axis ones. Since there is no dispersion during free-space propagation, the on-axis temporal profile remains unchanged.

For the numerical validation, the spatio-temporal profile of the pulse after the propagation distance of  $z = 50Z_R$  has been computed using the conventional pulse propagation method based on the FT [8,9]. The resulting final amplitude profile of the propagated pulse together with the residual error is shown in Fig. 4.20. The residual error of

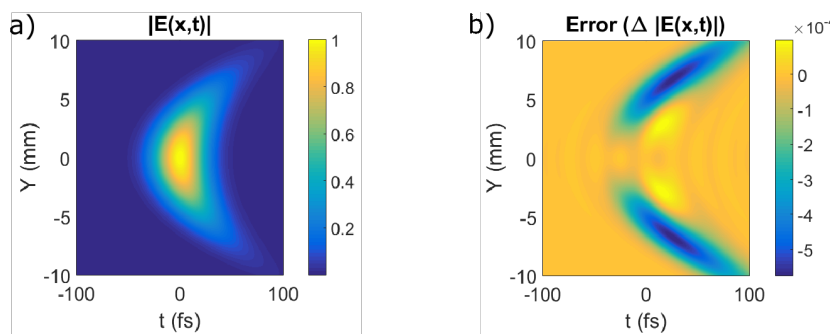


Figure 4.20: a) The same as in Fig. 4.19c but now computed using the conventional FT based method, b) The numerical difference between the amplitude profiles in (a) and in Fig. 4.19c.

the final spatio-temporal amplitude profile computed with the proposed method compared to the temporal FT based method is in the order of  $10^{-4}$ . The main reason for the residual error is that the higher-order dependence of the off-axis pulse delay on the transversal coordinates, beyond the second-order, are not taken into account for a single GPB in the proposed method. However, such higher-order spatio-temporal coupling can be taken into account by performing the GPD of the given pulsed beam in the spectral domain.

#### 4.2.2 Propagation of spatially truncated Gaussian pulsed beam

Now consider a single truncated GPB with a central wavelength of  $800nm$ , the temporal width of  $50fs$ , spatial waist radius of  $100\mu m$ , and truncation parameter  $c_x = 0$  in the x-dimension propagating through fused silica. To model the spatio-temporal coupling, the input spectral profile is decomposed into a set of 15 GPs with different central frequencies distributed uniformly in the input spectral range. This decomposition results in temporally wider GPs for which the off-axis delay can be neglected compared

to their temporal duration. Employing a single truncated GB for the spatial profile, a total of 15 spatially truncated GPBs is obtained to represent the given truncated pulsed beam. By propagating each spatially truncated GPB through the fused silica and performing the phase correct superposition, the spatio-temporal amplitude profiles of the final pulse are computed for different propagation distances as shown in Fig. 4.21. For the short propagation distance as shown in Fig. 4.21b, the truncated GPB

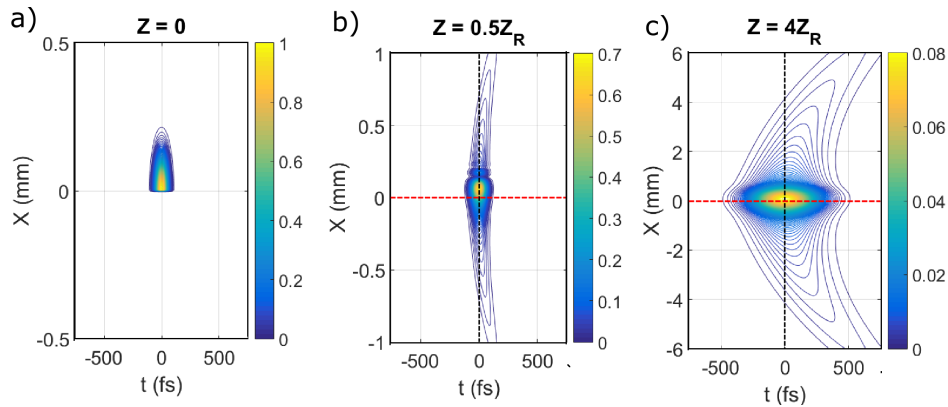


Figure 4.21: The  $x$  cross-section ( $y = 0$ ) spatio-temporal amplitude profile of spatially truncated GPB propagated by a distance of a) 0, b)  $0.5Z_R$  and c)  $4Z_R$  through fused silica with  $Z_R = 39.27\text{mm}$  being the Rayleigh length computed using the central frequency. The vertical axis and color bar scales of the three plots are not the same whereas that of the horizontal axis are the same.

starts to diverge spatially quickly and has the typical oscillations and asymmetry in the amplitude profile due to the diffraction from the sharp edge of the semi-infinite aperture. Additionally, the temporal width of the pulsed beam increases, and the pulse front gets curved due to the dispersion of the medium and the spatio-temporal coupling respectively during the propagation. As the propagation distance increases, the temporal width of the pulse increases significantly due to the large amount of dispersion but the asymmetry and the oscillation in the amplitude profile due to the truncation reduces as shown in Fig. 4.21c.

To validate the results quantitatively, the given spatially truncated GPB has been propagated to a distance of  $z = 0.5Z_R$  by using the conventional pulse propagation method based on the temporal FT [8, 9]. The cross sectional amplitude profiles along the dotted lines in Fig. 4.21b together with the corresponding amplitude profile computed using the FT based method with 128 spectral components are shown in Fig. 4.22. From Fig. 4.22 it can be seen that the results obtained using the propagation methods proposed in section 3.3.3 agrees with that computed using the temporal FT based method with the residual error in the order of  $10^{-3}$  or less.

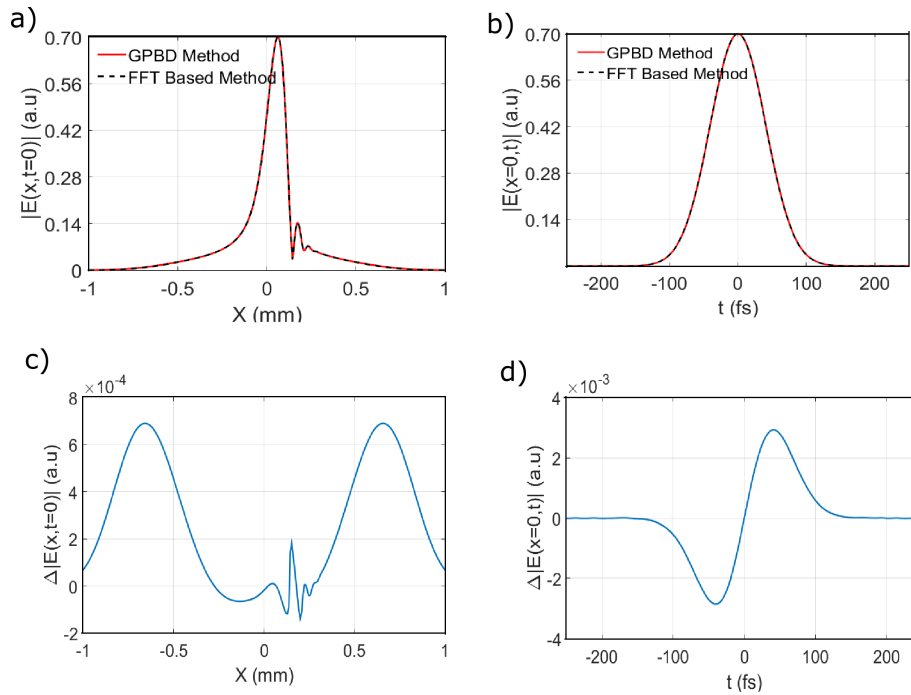


Figure 4.22: The cross sectional view of the spatio-temporal amplitude profile in Fig. 4.21b along a)  $t = 0$  and b)  $x = 0$  together with the corresponding result obtained using the conventional ultrashort pulse propagation method based on the temporal FT. The numerical error  $\Delta|E(x,t)| = |E(x,t)|_{GPBD} - |E(x,t)|_{FFT}$  for the amplitude profiles shown in (a) and (b) are plotted in (c) and (d) respectively.

### 4.2.3 Gaussian pulse decomposition of spectral profile with a large TOD

In this section, the application of the Gaussian pulse decomposition method discussed in section 3.2.1 is demonstrated with an example. Consider the decomposition of an input pulse with central wavelength of  $\lambda_0 = 800nm$ , a Gaussian spectral amplitude profile with bandwidth of  $\Delta\lambda \approx 68nm$  (corresponding to pulse duration of  $\sigma_t \approx 10fs$  in transform limited case) and third order dispersion coefficient of  $TOD = 1000fs^3$  as shown in Fig. 4.23a. The input spectral profile is decomposed using 10 uniformly distributed GPs. The initial temporal delays  $\phi'(\omega_0)$  and the group delay dispersions  $GDD = \phi''(\omega_0)$  of each GPs are shown in Fig. 4.23b. As the input spectral phase is a third order function of the angular frequency, the group delay has quadratic distributions in the spectral range as shown in Fig. 4.23b. It can also be seen that depending on the local curvature of the given spectral phase, the GPs have both positive and negative group delay dispersions. From Fig. 4.23a, it can be seen that the quadratic spectral phase of the GPs fit with the given spectral phase around the central frequency of the GP. After the peak amplitudes of individual GPs is computed, the decomposition



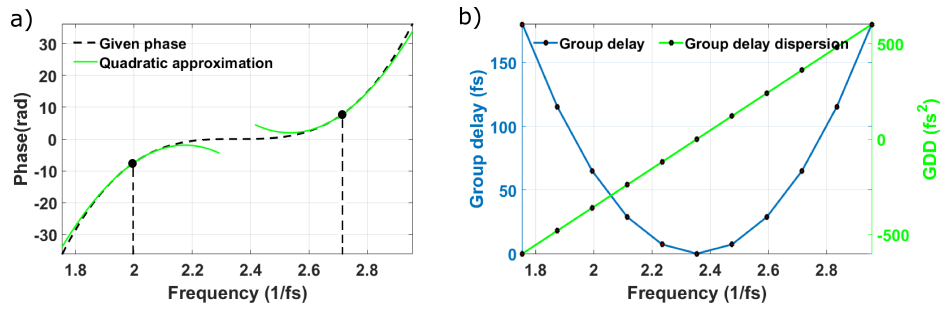


Figure 4.23: a) The spectral phase of the given pulse together with the quadratic spectral phases (shown for only two sampling points, at  $2(1/\text{fs})$  and  $2.7(1/\text{fs})$ , for clarity), b) the group delays and the group delay dispersion of the GPs used for the decomposition. Every black dot corresponds to the center of one GP used.

result has been validated by comparing the given spectral profile with that obtained by the summation of the complex amplitudes of all GPs after the decomposition. From the decomposition result shown in Fig. 4.24, it can be seen that even with such a few number of GPs, the proposed decomposition method gives accurate results. The residual root mean square error is below 0.1% for both amplitude and phase profiles.

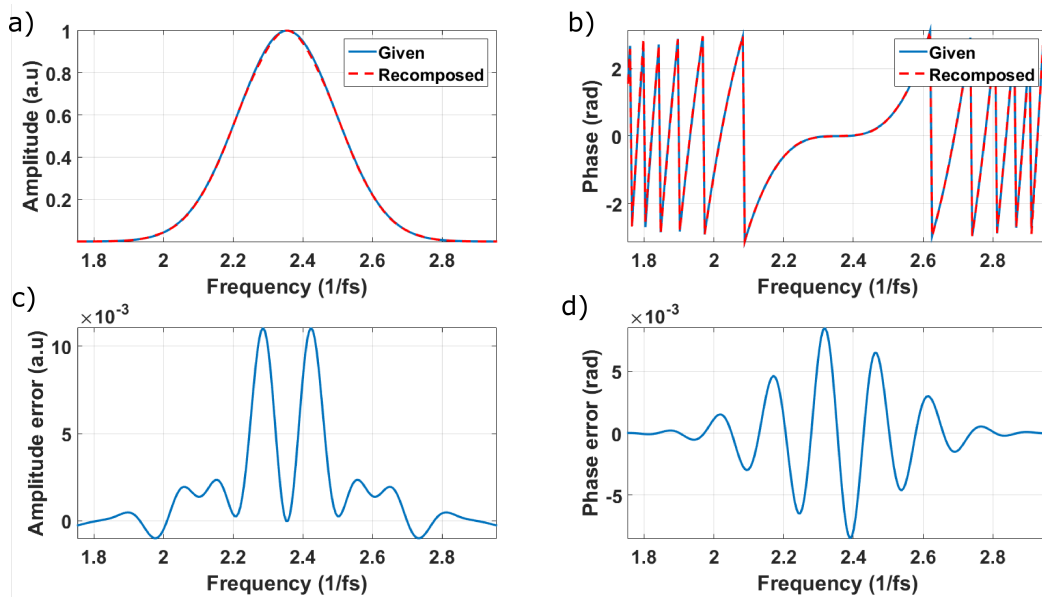


Figure 4.24: The spectral a) amplitude and b) phase profiles of the given pulse together with that obtained by superposition of the elementary GPs each with different delay and chirp parameters. The residual error of the spectral c) amplitude and d) phase after GPD.

By performing the superposition of the GPs in the temporal domain, the temporal profile of the input pulse which is shown in Fig. 4.25 is computed. The asymmetrical oscillation in the amplitude profile in Fig. 4.25 clearly shows the typical temporal shape of a GP with large third order dispersion. For the purpose of comparison, the same spectral profile has been decomposed with the same number of GPs but with

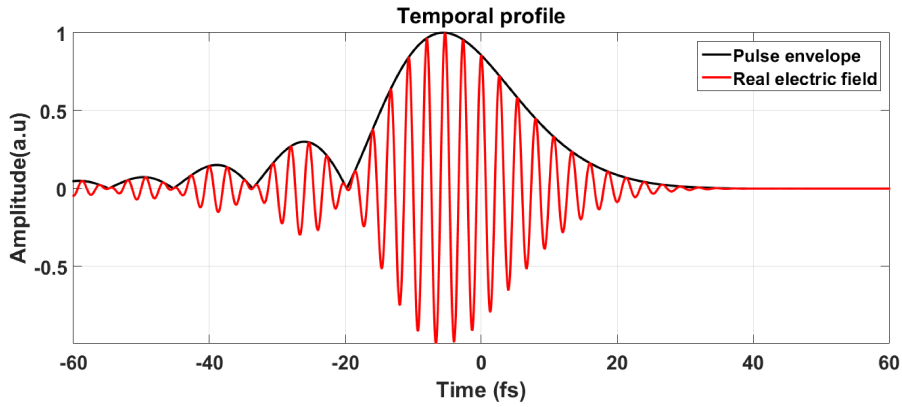


Figure 4.25: The temporal amplitude profile of the given pulse with large TOD computed by superposition of the elementary GPs.

zero initial chirp and no group delays for individual pulses. The resulting accuracy of the decomposition reduces as shown in Fig. 4.26, which shows the significance of using initially delayed and chirped GPs in the decomposition.

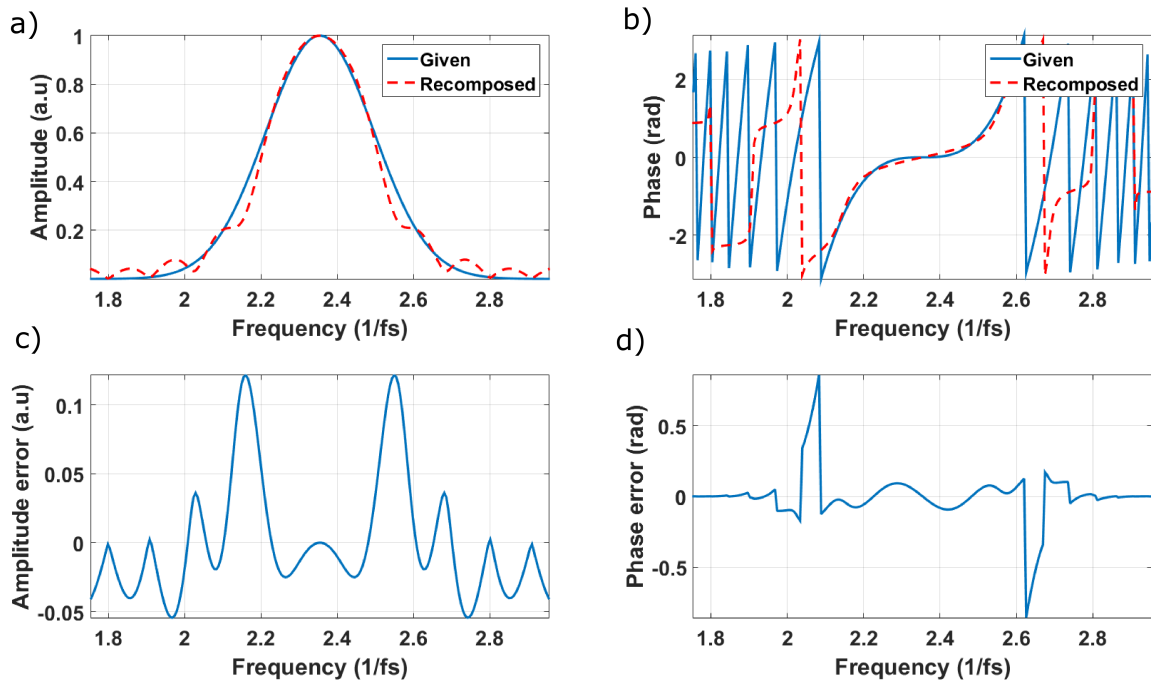


Figure 4.26: The same as in Fig. 4.24 but now computed using zero initial delay and chirp parameters of the individual GPs.

#### 4.2.4 Propagation of ultrashort pulse after circular aperture

In this example I demonstrate the application of the spatially truncated GPBs for modeling the diffraction of pulse field after a hard aperture. Consider an ultrashort pulse with central wavelength of  $\lambda_0 = 800nm$ , Gaussian temporal profile of  $\sigma_t = 10fs$

and uniform spatial amplitude with flat phase truncated by a circular aperture of radius  $a = 2\text{mm}$ . To propagate the pulse after aperture using the GPBD method, the spatial and spectral profiles of the pulse just after the aperture are decomposed into a set of  $30 \times 30$  full GPBs ( $30 \times 30$  GBs for spatial and 1 GP for spectral) and 1050 spatially truncated GPBs (70 truncated GBs for spatial and 15 GPs for spectral). The truncated GPBs are distributed around the edge of the aperture to represent the sharp edged in the amplitude profile. Since the spatio-temporal coupling of full GPBs in free space are taken into account by computing the off-axis pulse delay from the smooth quadratic phase as explained in section 3.2.5, only a single GP is sufficient to represent the Gaussian spectral profile. However, the spectral profiles of the truncated GPBs is decomposed into 15 temporally wider GPs to account for the spatio-temporal coupling during the propagation as discussed in section 3.3.3. The propagated pulse profiles are computed by performing the phase correct superposition the full and the spatially truncated GPBs after propagation. In Fig. 4.27, the spatio-temporal profile of the propagated ultrashort pulse after by the circular aperture at flight time  $t = 600\text{ps}$  are plotted. The time at which the incoming pulse arrives at the aperture plane is assumed to be  $t = 0$ . Due to the diffraction from the hard aperture edges, the spatio-temporal

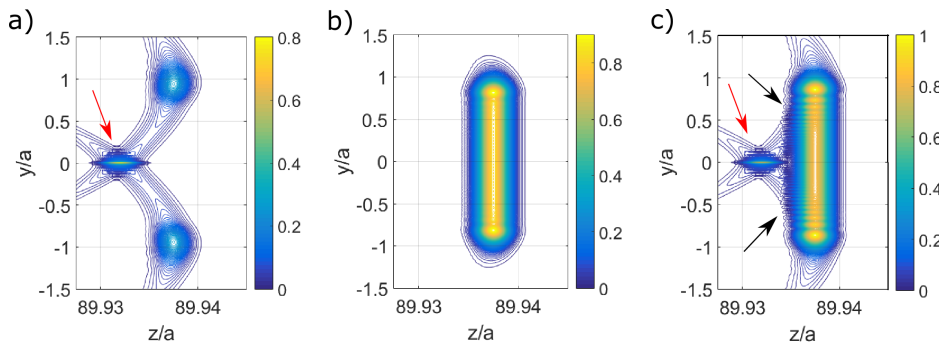


Figure 4.27: The spatial amplitude profile of a) the outer sub-field with sharp edge, b) the inner sub-field and c) the total field for plane wave pulse truncated by circular aperture with radius  $r = a$  after propagating for  $t = 600\text{ps}$ .

profiles in Fig. 4.27 has two types of interference patterns. The first interference pattern, which is shown by red arrow in both Fig. 4.27 (a and c), comes from the interference of the boundary diffraction wavelets and hence is called the boundary wave pulse [8,91,92]. The second one which is shown by the dark arrows in Fig. 4.27c as the oscillations on the main pulse comes from the interference of the main pulse with the boundary pulse [91].

If the spatial profile of the input pulse is changed from plane to a converging spherical

wave with radius of  $R = 50\text{mm}$ , the propagated pulse after the aperture has different spatial profiles before and after the focal planes as shown in Fig. 4.28. In this case, for the time coordinate it is assumed that the incoming pulse reaches the edge of the aperture at  $t = -R/c$  and passes through the focus at  $t = 0$ . As it can be seen from

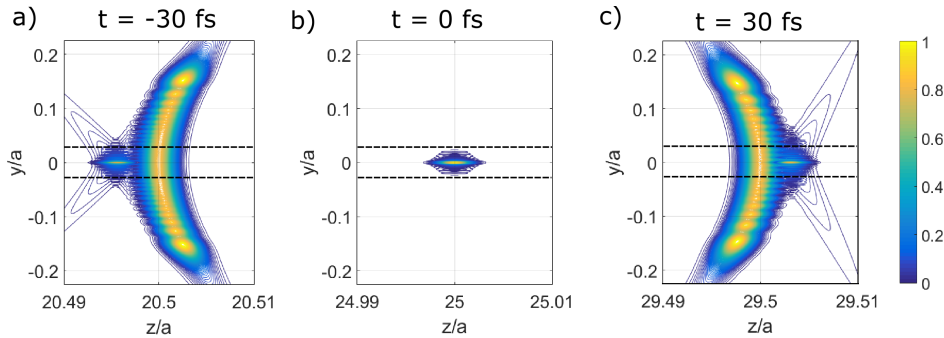


Figure 4.28: The spatial amplitude profile of the converging wave pulse truncated by circular aperture at time a)  $t = -30\text{fs}$ , b)  $t = 0\text{fs}$  and c)  $t = 30\text{fs}$ . The arrival time of the pulse peak at the focal plane is taken as  $t = 0$ .

Fig. 4.28a, the diffraction from the hard aperture results in the boundary wave pulse which lags behind the main pulse. However, as one passes through the focal plane, the boundary wave pulse catches up and then starts to lead main pulse and hence becomes the conventional forerunner pulse [8,92] as shown in Fig. 4.28(b and c). For the pulse away from the focal plane, the additional oscillation on the main pulse is also observed which is due to the interference of the main pulse with the boundary wave pulse like in the case of the plane wave pulse.

The boundary wave pulse has the shape of the letter X which is similar to that of the Bessel-X pulse generated for example after an axicon (see section 4.2.6). However, unlike the Bessel-X pulse, which is a non-diffracting wave, the boundary wave pulse changes its shape as it propagates. This can be clearly seen by observing the boundary wave pulse closely as the pulse propagates in the focal region as shown in Fig. 4.29. From Fig. 4.29 it can be seen that the size and shape of the boundary wave pulse changed during propagation.

#### 4.2.5 Pulse focusing using an aspheric lens

In this example the GPBD method is applied to analyse the focusing of ultrashort pulse using the Geltech aspheric lens from Thorlabs (354240 A) with focal length  $f = 8.00\text{mm}$  and numerical aperture  $NA = 0.5$  shown in Fig. 4.30a [93]. An input pulse with central wavelength  $\lambda_0 = 800\text{nm}$ , Gaussian temporal profile with width of  $24\text{fs}$ , a super-Gaussian spatial amplitude profile with  $8\text{mm}$  diameter and super

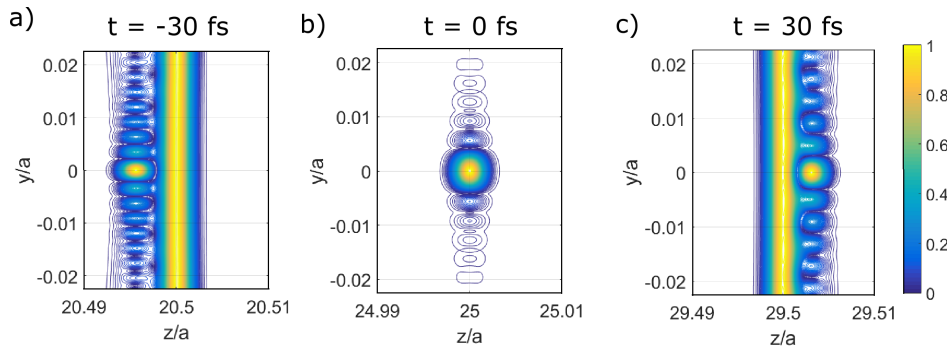


Figure 4.29: The same as in Fig. Fig. 4.28 but showing the central part between the dotted lines in zoomed version by using equal scaling for both axis to clearly show the change in the shape of the boundary wave pulse as it propagates.

Gaussian order of  $m = 20$  has been considered. Additionally, the spectral and spatial phases of the input pulse are assumed to be flat. As the spherical aberration is corrected by the aspherical surface, the dominant remaining aberration of the system is the chromatic aberration [8]. Since the group path length is greater than the refractive index for the dispersive glass, the pulse front after the lens lags behind the phase front. In addition to that, due to the variable glass thickness encountered, the delay of the

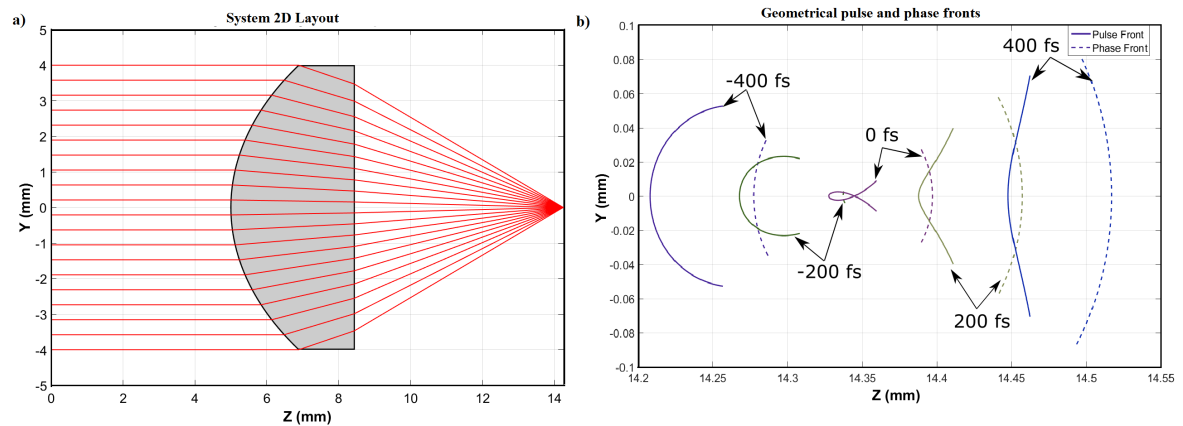


Figure 4.30: a) The 2D system layout, and b) the geometric pulse and phase front in the focal region of the Geltech Aspheric Lens used for focusing ultrashort pulse.

pulse decreases as one goes from the center of the lens towards the edge. This can be seen from Fig. 4.30b, which shows the geometrical pulse front and the phase front in the focal region computed by using the real ray tracing at the central wavelength. The time is chosen in such a way that  $t = 0$  refers to the pulse group along the axis reaches the focal plane.

For the wave optical modeling, including the diffraction effects in the focal region, the super-Gaussian spatial profile of the input pulse has been decomposed into a set of

$30 \times 30$  GBs and a single GP is used for the Gaussian spectral profile. Combining the GP with the GBs, we get a total of  $30 \times 30$  GPBs to represent the input pulse. Applying the GPBD method, the pulse field in the focal region has been computed at different flight times and their  $y - z$  cross-sectional intensities are as shown in Fig. 4.31. From

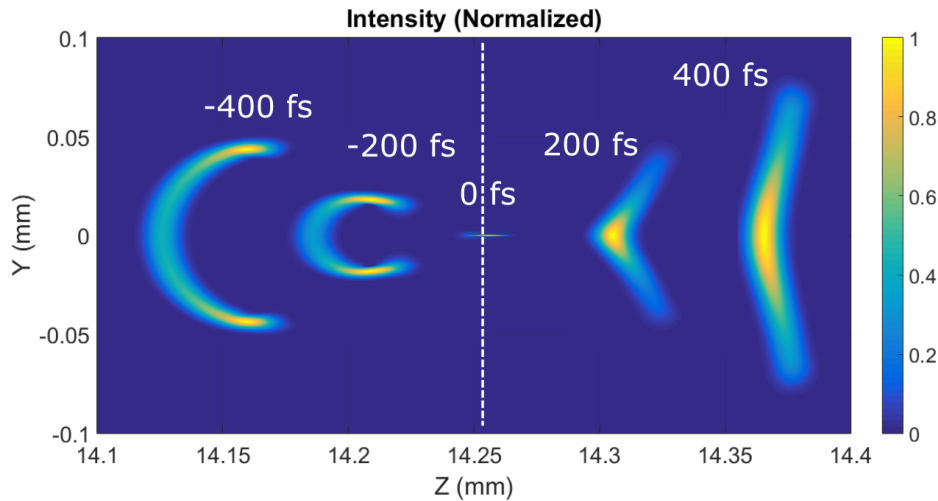


Figure 4.31: The  $y - z$  cross-sectional view of the spatial intensity profile of the ultrashort pulse near the focal plane of the aspheric lens for different times. The time is chosen in such a way that  $t = 0$  refers to the pulse intensity maximum reaches at the focus.

the result in Fig. 4.31 it can be seen that due to the chromatic aberration of the lens, pulse front is distorted to the typical horseshoe shape [8]. In the region outside the close vicinity of the focal plane, the pulse front computed using the wave optical method looks similar to that obtained from the geometrical ray-tracing calculations shown in Fig. 4.30b. To validate the results quantitatively, the pulse profile at the focal plane has been computed using the conventional pulse propagation method based on FTs and compared with the result from the GPBD method. In Fig. 4.32 the  $y$ -cross-section of the intensity profile of the pulse at the focal plane along the dotted white line in Fig. 4.31 is plotted together with the corresponding intensity profile computed using the conventional method [8,9]. From Fig. 4.32 it can be seen that the GPBD method gives focal plane pulse intensities with residual error below 1%. The spatial profiles of the pulse in the focal region obtained using the proposed method also agrees with that computed using the conventional FT based method and reported in Fig. 4b of [8].

However, since a super-Gaussian amplitude profile is used for the input pulse, the front runner pulse, which is the result of sharp edge diffraction of the pulse, does not appear in Fig. 4.31. By changing the spatial amplitude of the input pulse to a uniform amplitude truncated by a hard circular aperture of radius  $r = 4\text{mm}$  and computing

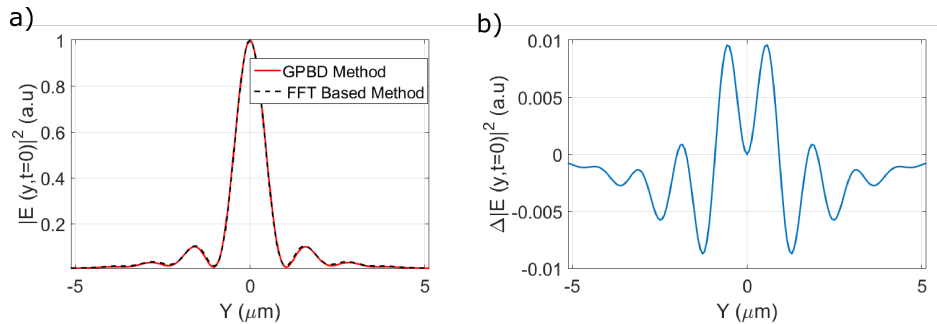


Figure 4.32: a) The  $y$  cross-section of the pulse intensity profile at the focal plane computed using the GPBD and the FT based methods. b) the difference in the pulse intensities obtained using the two methods.

the propagated pulse at time  $t = -200fs$  using the modified GPBD method, the final spatial profile shown in Fig. 4.33a is obtained. From Fig. 4.33 it can be seen that the diffraction from the hard aperture results in the boundary wave pulse along the axis in addition to the main pulse. The boundary wave pulse has already taken over the main pulse before the focal plane of the lens. This is because the pulse front close to the optical axis is delayed compared to that coming from the edge due to the different glass thickness encountered. This shifts the point where the boundary wave takes over the main pulse closer to the lens unlike the ideal focusing case where the takeover occurs at the focal plane (see section 4.2.4).

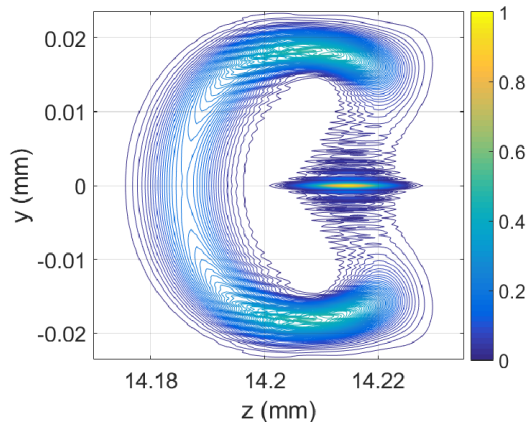


Figure 4.33: The spatial profile of the pulse in the focal region of the lens at  $t = -200fs$  for an input plane wave pulse truncated by a circular aperture.

#### 4.2.6 Bessel-X pulse after an axicon

Propagation of an ultrashort pulse through an axicon results in a Bessel-X pulse which maintains its strong lateral and longitudinal localization for large propagation distances. In this example, the formation of a Bessel-X pulse is demonstrated by propagating an ultrashort pulse after an axicon from Thorlabs (AX252-2.0 $^\circ$ ) using the GPBD method. The axicon is made of fused silica and has a central thickness of  $5.44\text{mm}$ . The front and rear surfaces of the axicon are an odd asphere with  $z(x, y) = -0.0349\sqrt{x^2 + y^2}$  and a plane surface, respectively. This results in axicon with an apex angle of  $176^\circ$  [94]. The ray-tracing result of the axicon is shown in Fig.

4.34. For the input pulse, a Gaussian temporal amplitude profile with a width of  $50fs$ ,

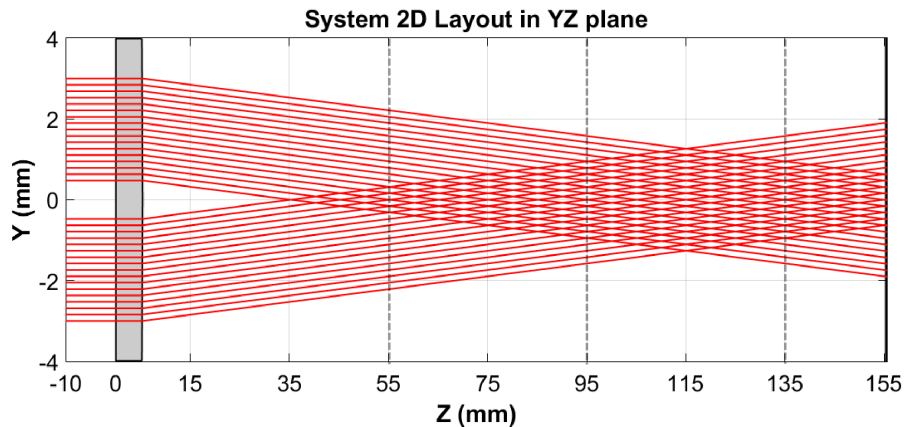


Figure 4.34: The 2D layout of an axicon used to generate a Bessel-X pulse (different scales are used for  $z$  and  $y$ -axis to make the rays more visible). The dotted lines indicate the locations of the transversal planes where the pulse intensities are computed.

central wavelength of  $\lambda_0 = 800nm$ , a ring-shaped spatial amplitude profile with an inner and outer radius of  $0.5mm$  and  $3mm$ , respectively are used. The spatial and spectral phase profiles of the input pulse are assumed to be flat. First, the input pulse is decomposed into  $30 \times 30$  GPBs ( $30 \times 30$  GBs for the spatial and single GP for the spectral profiles). By propagating the decomposed GPBs through the axicon and performing the phase correct superposition, the spatio-temporal amplitude profiles shown in Fig. 4.35 are obtained for the propagated pulses at three different transversal planes after the axicon. For the time coordinates shown in the plots, the arrival time of an on-axis reference pulse propagating along the  $z$ -axis with the speed of light to each transversal plane is used as the origin ( $t = 0$ ). The results in Fig. 4.35 shows that after the axicon, the typical Bessel-X pulse is obtained whose spatial amplitude profile is strongly localized and maintained for such large propagation distance of  $80mm$ . The temporal profiles of the Bessel-X pulse are also not changed as it is propagating in the free space which has no dispersion. However, in the case of a dispersive medium, the axial intensity distribution changes during propagation [95].

For the validation of the result, the comparison of the cross section of the result shown in Fig. 4.35b with that computed using the analytical propagation equations of the Bessel X-pulse [96] is shown in Fig. 4.36. As it can be seen from Fig. 4.36b, the residual error of the result obtained using the GPBD method is below 0.15%.

The temporal cross-sections of the amplitude profiles of the Bessel-X pulse for the three transversal planes, shown in Fig. 4.37, indicates that the temporal profile re-



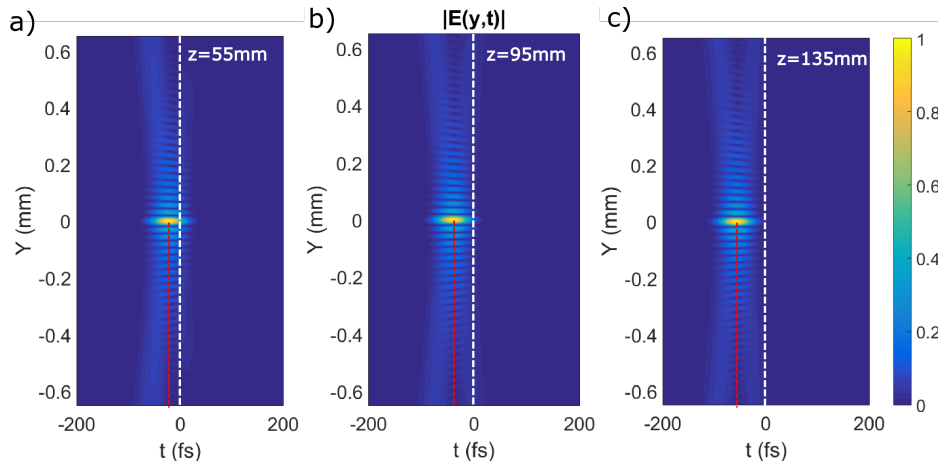


Figure 4.35: The  $y - t$  cross-section of the amplitude profile of the Bessel-X pulse on the transversal planes which are located at a)  $55\text{mm}$ , b)  $95\text{mm}$  and c)  $135\text{mm}$  from the axicon. The white dotted lines indicate the location of  $t = 0$  and the red dotted lines indicate the location of the pulse peak.

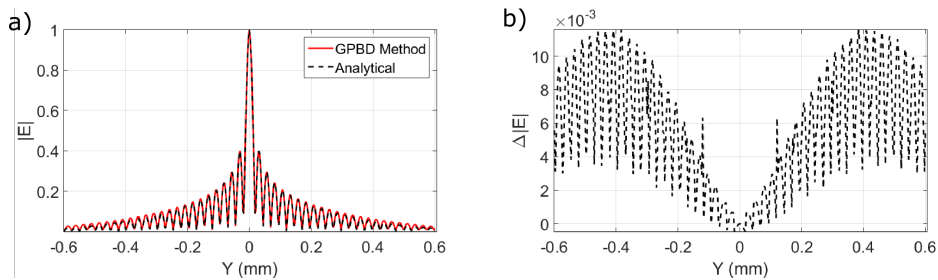


Figure 4.36: a) The 1D cross section of the Bessel X-pulse on the transversal plane located at  $z = 95\text{mm}$  from the axicon computed by using the GPBD method together with that obtained using the analytical propagation formula. b) The numerical difference of the magnitudes of the amplitude profiles shown in (a).

mains Gaussian. However, the arrival time of the pulse peak is different for different propagation distances and is always negative which means earlier in time relative to the reference pulse. This is because the peak of the Bessel-X pulse travels at superluminal group velocity which is greater than the speed of light and hence arrives on each transversal plane before the reference on-axis pulse. The superluminal velocity of the pulse peak is not in contradiction of the Einstein's theory of relativity as the Bessel-X pulses do not transmit information superluminally [97]. This property of the Bessel-X pulse has been studied experimentally in the previous studies [8, 97, 98].

The superluminal velocity along the  $z$ -axis of Bessel-X pulse is theoretically computed from the deflection angle  $\alpha$  which the outgoing ray from the axicon makes with the  $t$ -axis by  $v_g = c / \cos \alpha$  [8]. For the example axicon under consideration,

the deflection angle  $\alpha = 0.9238^\circ$ , and hence the expected speed of the intensity peak becomes  $1.00013c$ . From Fig. 4.37, it can be seen that over the propagation distance of  $80\text{mm}$ , the Bessel-X pulse leads the reference pulse by  $35.2\text{fs}$ . From this the group velocity of the Bessel-X pulse peak is computed to be  $v_g = 1.0001319c$ . This group speed is very close to the theoretically expected value. Similar results have been obtained from the experimental measurements and independent simulations reported previously [97].

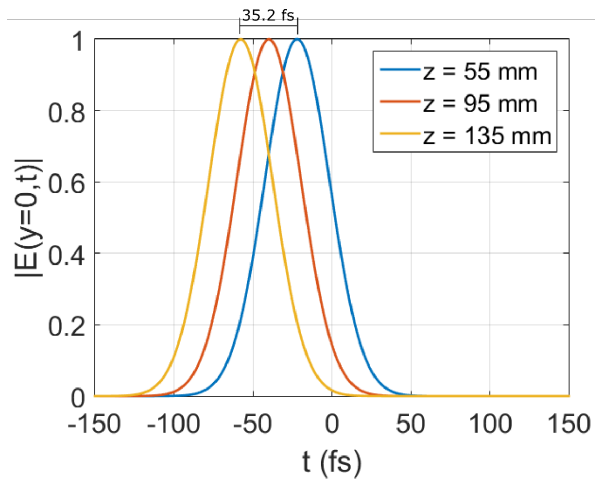


Figure 4.37: The temporal cross-sections of the amplitude profiles shown in Fig. 4.35 for the on-axis point.

#### 4.2.7 Ultrashort pulse shaping using diffraction gratings

In this section the applications of the GPBD method for the wave optical propagation of pulses through pulse shaping systems containing diffraction gratings are demonstrated.

##### Single diffraction grating

Consider propagation of an ultrashort pulsed beam after a single diffraction grating with groove density of  $1.2\text{lines}/\mu\text{m}$  and diffraction order of  $m = -1$  as shown in Fig. 4.38. The input pulse considered has a Gaussian temporal profile with temporal amplitude width of  $50\text{fs}$ , a super-Gaussian spatial profile with diameter of  $5\text{mm}$  and an order of 20 and central wavelength of  $800\text{nm}$ . In the setup, the tilt angles of the

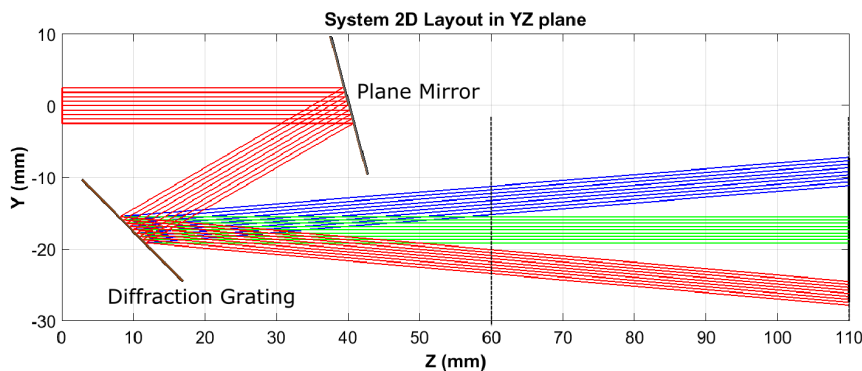


Figure 4.38: System layout and geometrical ray tracing through a single grating system. (Note that the coordinate origin is not at the center of the grating.)

first mirror and the diffraction grating are adjusted so that the diffraction angle at the

grating becomes  $\theta_D = 45^\circ$  and both the incoming and the outgoing beams are along the  $z$ -axis for the central wavelength. First the spatial profile of the input pulse is decomposed into a set of  $30 \times 30$  GBs and the spectral profile is decomposed into a set of 25 GPs. Combining the GBs with the GPs, a total of 22,500 GPBs are used for the decomposition of the input pulse. By using the GPBD method, the final spatial and spatio-spectral profiles of the propagated pulse after the diffraction grating have been computed. The spatial profiles of the propagated pulse computed at the moment in time when the central pulse group arrives at the transversal planes located at  $z = 60\text{mm}$  and  $z = 110\text{mm}$ , are shown in Fig. 4.39 (a and c), respectively. The spatio-spectral profiles, shown in Fig. 4.39 (b and d), are computed for the points along the  $y$ -axis (with  $x = 0$ ) on the corresponding transversal planes.

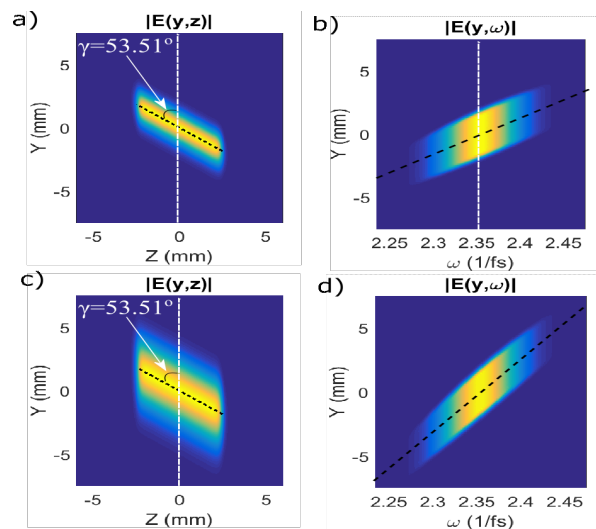


Figure 4.39: The spatial profile of the pulse at the moment when its peak arrives a transversal plane located at a)  $z = 60\text{mm}$  and c)  $z = 110\text{mm}$ . The spatio-spectral profiles on the  $y$ -cross section of the two transversal planes are shown in (b) and (d) respectively.

From Fig. 4.39a, it can be seen that the pulse front is strongly tilted due to the angular diffraction of the diffraction grating. The expected tilt angle of the outgoing pulse, computed using the analytical formula given in Eq. (4.55) in [4], is  $\gamma = 53.63^\circ$  which is very close to that obtained from the simulation result in Fig. 4.39a. The slight disagreement comes from the manual computation of the tilt angle by taking two points on the dotted line in the spatial profile in Fig. 4.39a. As it can be seen from the spatio-spectral profile in Fig. 4.39b, different spectral components have separated spatially along the  $y$ -axis resulting in large spatial chirp and hence tilted pulse front in the spatio-spectral profile.

For the longer propagation distance from the diffraction grating, the separation between different spectral components and the overall spatial size of the pulse increases due to the angular dispersion of the grating as shown in Fig. 4.39 (c and d). Since the spatial chirp increases, the tilt in the spatio-spectral profile also increases. However, the pulse front tilt in the spatial profile remains unchanged which is also expected as the pulse

front tilt given in Eq. (4.55) in [4] is independent of the propagation distance.

### Treacy grating pair compressor

One of the common pulse shaping system which employs the diffraction grating is the Treacy grating pair which is used to generate large anomalous dispersion and hence used as pulse compressor [76]. In the Treacy compressor a pair of diffraction gratings are arranged in tandem with their faces and rulings parallel to each other as shown in Fig. 4.40 [75,76]. The first diffraction grating adds a large angular dispersion to the incoming

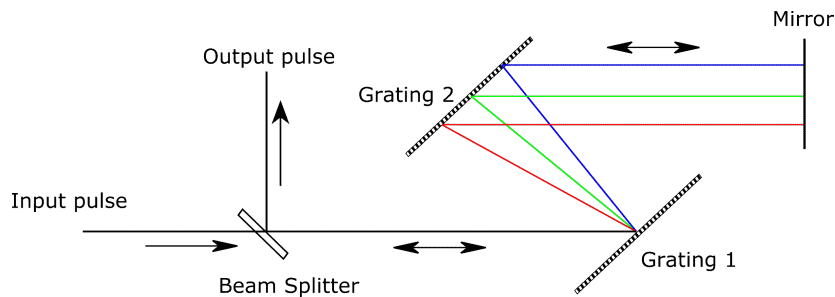


Figure 4.40: The schematic diagram of a Treacy compressor.

pulse so that different spectral components are reflected at different angles and hence follow different paths. This results in a large anomalous dispersion which depends on the propagation distance after the diffraction grating [4]. The second grating re-collimates the rays by removing the angular dispersion. At the end of the single pass of the Treacy grating pair, different spectral components of the pulse separate spatially resulting in large spatial chirp. This spatial chirp is usually removed by using the setup in double-pass mode by placing a mirror after the 2<sup>nd</sup> grating.

Consider a Treacy compressor that is constructed using diffraction grating with a groove density of  $1.2 \text{ lines}/\mu\text{m}$  with rulings parallel to the x-axis and used in the first diffraction order. The gratings are tilted in the  $yz$  plane so that the diffracted angle at the first grating becomes  $\theta_D = 45^\circ$  for the central wavelength and the distance from the 1<sup>st</sup> grating to the 2<sup>nd</sup> one along the central ray is set to  $d = 500 \text{ mm}$ . For double pass usage, a mirror is placed after the 2<sup>nd</sup> grating perpendicular to the outgoing rays. Using the analytical formula given in Table 1 in [99], the group delay dispersion (GDD) and the third-order dispersion (TOD) of the Treacy compressor become  $1.306 \times 10^6 \text{ fs}^2$  and  $-3.923 \times 10^6 \text{ fs}^3$ , respectively, for a wavelength of  $800 \text{ nm}$ . Hence, the Treacy compressor generates very large anomalous dispersion (negative GDD) in the order of  $10^6 \text{ fs}^2$ . However, the sign of the TOD of Treacy compressor is the same as that of normal dispersive materials [99]. Therefore, the compressor increases the TOD of the

pulse after a dispersive medium. This results in the compressed pulse with residual higher-order dispersion, which is mainly dominated by the TOD.

To model the GDD compensation and the residual TOD effects of the Treacy compressor, an initially chirped input pulse has been assumed with the following parameters: central wavelength of  $800nm$ , Gaussian spatial amplitude profile with a width of  $2mm$ , Gaussian spectral amplitude profile with a width of  $13.59nm$  (corresponding to the transform-limited temporal amplitude width of  $50fs$ ) and quadratic spectral phase with initial GDD which is equal in magnitude but opposite in sign to that of the Treacy compressor (i.e. for single and double-pass mode, the initial GDD of  $1.306 \times 10^6 fs^2$  and  $2.612 \times 10^6 fs^2$ , respectively, are used). Here an initially chirped-pulse has been used to demonstrate the application of the GPBD method in the propagation of such non-transform limited input pulse with large spectral phase coefficients and model dispersion compensation of the Treacy compressor.

First the input chirped pulse is decomposed into a set of 80 GPBs each with different central frequencies, group delays, and GDD corresponding to the slope and the quadratic factor of the local spectral phase respectively. From the comparison of the input spectral profile and that after the GPBD, shown in Fig. 4.41, it can be seen that the given input pulse is correctly represented by the GPBs with residual error below 0.1% in both spectral amplitude and phase.

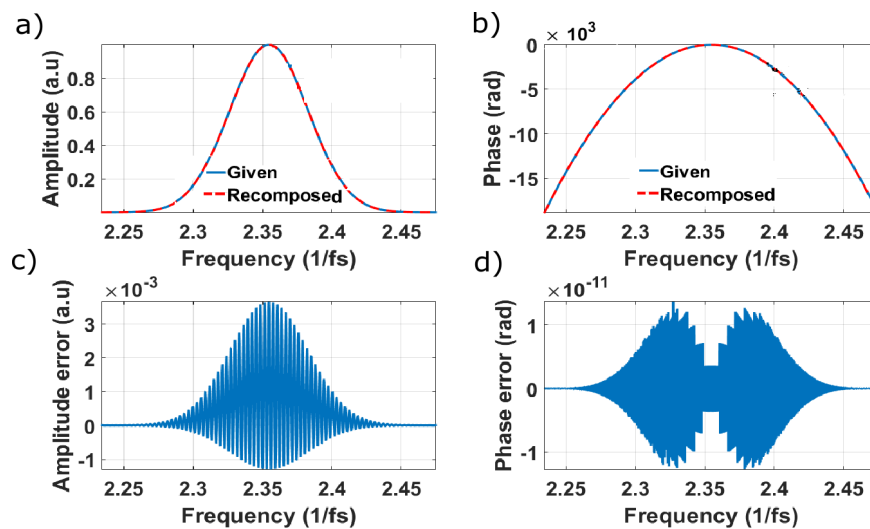


Figure 4.41: The spectral a) amplitude and b) phase of the chirped input pulse together with that obtained after the GPBD. The residual error of the spectral c) amplitude and d) phase of the decomposition. For results in (b) and (d) only small frequency range near the central frequency is shown for clear comparison.

Propagating the individual GPBs independently through the Treacy compressor, and performing phase correct superposition in the final plane, the spatio-temporal profile shown in Fig. 4.42 has been obtained for the output pulse after a single pass mode. From Fig. 4.42 it can be seen that, the output pulse has large pulse front curvature in

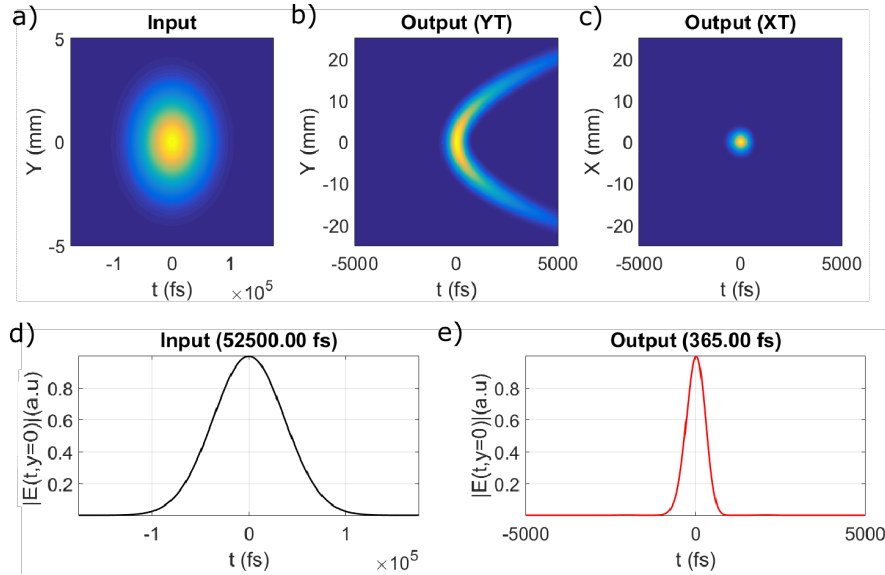


Figure 4.42: The spatio-temporal amplitude profile of a) the chirped input pulse b) the  $y$ -cross section and c) the  $x$ -cross section of the output pulse after a single pass through the Treacy compressor. The temporal amplitude profile at the center ( $x = y = 0$ ) of d) the input and e) the output pulse.

the  $yz$  plane which is due to the combination of the large spatial chirp and the residual TOD. The quadratic spectral phase factor due to the residual TOD is manifested in the output pulse by the curved pulse front as the spectral components are separated spatially along the  $y$ -axis due to the spatial chirp. Comparing the results in Fig. 4.42 (d and e), it can further be seen that the local temporal width of the output pulse at the center of the spatio-temporal profile is significantly reduced from initially chirped input pulse due to the GDD compensation. However, due to the large spatial chirp and residual TOD, the final on-axis temporal width is still very large compared to the transform-limited temporal width of the input pulse.

For Treacy compressor used in double-pass mode, the spatio-temporal profile of the output pulse is shown in Fig. 4.43. As can be seen from Fig. 4.43, the output pulse is mainly dominated by TOD which results in large and asymmetrical oscillation in the pulse amplitude profile. Since there is no spatial chirp, all spectral components overlap spatially and the TOD does not result in the curved pulse front as in the case of single-pass mode. The GPBD methods allow for the wave optical modeling of the system with

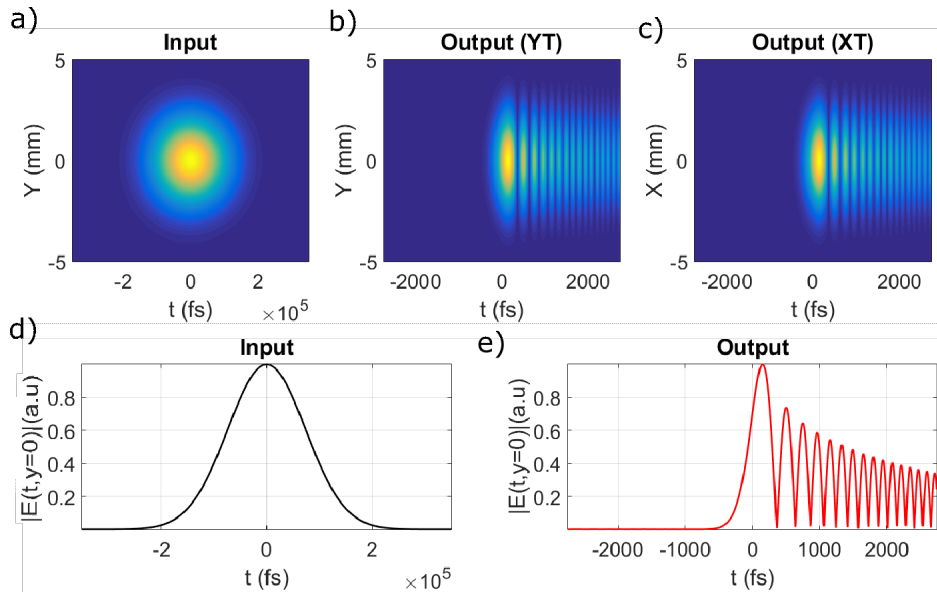


Figure 4.43: The same as in Fig. 4.42 but now computed for double pass usage of the Treacy compressor

such large residual dispersion using a fairly practical number of GPBs. This makes the GPBD method suitable for wave optical modeling of Treacy compressor systems to study for instance misalignment sensitivities.

#### A pulse stretcher-compressor setup

Now the wave optical modeling of a stretcher-compressor setups used in the chirped pulse amplification (CPA) system, which is the most commonly used technique of amplifying a given ultrashort pulse to high power level [100], is performed. In the CPA system the input pulse is first stretched by using a pulse stretcher before being amplified. Since the stretched pulse has reduced peak intensity, the pulse can be efficiently amplified to very large power without resulting in significant optical damage and non-linear effects during the amplification [100]. Finally, the amplified pulse is compressed by using a compressor, which is carefully designed with parameters matching to that of the stretcher to compensate dispersion introduced by the stretcher, to get the ultrashort pulse with extremely high peak intensity. The perfect dispersion compensation of the stretcher and compressor are very important for the quality of the amplified pulse. In practice Martinez stretcher and Treacy compressor are commonly used to construct such dispersion balanced systems.

A Martinez stretcher consists of a pair of anti-parallel diffraction gratings, which are tilted by the same angle but in the opposite direction, with two internal lenses arranged

in 4f setup as shown in Fig. 4.44. [4, 42, 101]. Unlike the Treacy grating pair, the Mar-

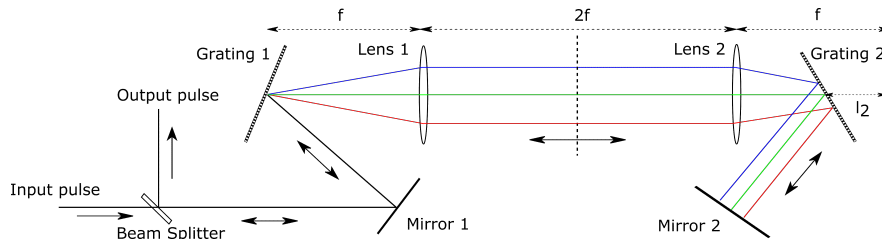


Figure 4.44: The schematic diagram of the Martinez stretcher.

tinez grating pair setup can be used to generate both normal and anomalous dispersion. If the first and the second diffraction gratings are placed exactly at the front and back focal planes of the first and second lens respectively, the system becomes dispersion-free. However, by moving the second grating towards or away from the focal plane of the second lens, the system can generate normal or anomalous dispersion, respectively. Like in the case of the Treacy compressors, a mirror is usually used in the Martinez stretcher in a double pass mode and removes the spatial chirp after the single pass.

Assuming an ideal telescope system, it is possible to make the Martinez grating pair to produce exactly equal dispersion of all orders but with opposite sign to that produced by the Treacy compressor. This requires matching of the incidence angles at the first gratings of the two systems and making the distance  $l_2$  equal to the distance measured along the ray direction between the two gratings in the Treacy compressor [4, 101].

Now consider the propagation of an ultrashort pulse which has a Gaussian temporal profile with a temporal width of  $50fs$  and a central wavelength of  $800nm$  through a pulse stretcher-compressor setup shown in Fig. 4.45. The system is built from a Martinez stretcher followed by a Treacy compressor, both used in the double-pass mode. As the study of the amplification process after the stretcher is beyond the scope of this study, any additional spectral phase and amplitude distortions coming from the amplification process in the real CPA system are ignored. The diffraction gratings used in both compressor and stretchers have a groove density of  $1.2lines/\mu m$  with rulings parallel to the x-axis and are used in the first diffraction order. The gratings are tilted in the  $yz$  plane so that the diffracted angle at the first grating becomes  $\theta_D = 45^\circ$  for the central wavelength. For the Treacy compressor, the distance from the 1<sup>st</sup> grating to the 2<sup>nd</sup> one along the central ray is set to  $d = 500mm$ . The ideal telescope used in the Martinez stretcher is constructed from two ideal cylindrical lenses with a focal length of  $700mm$  in the y-cross-sections. The 2<sup>nd</sup> grating in the Martinez stretcher is



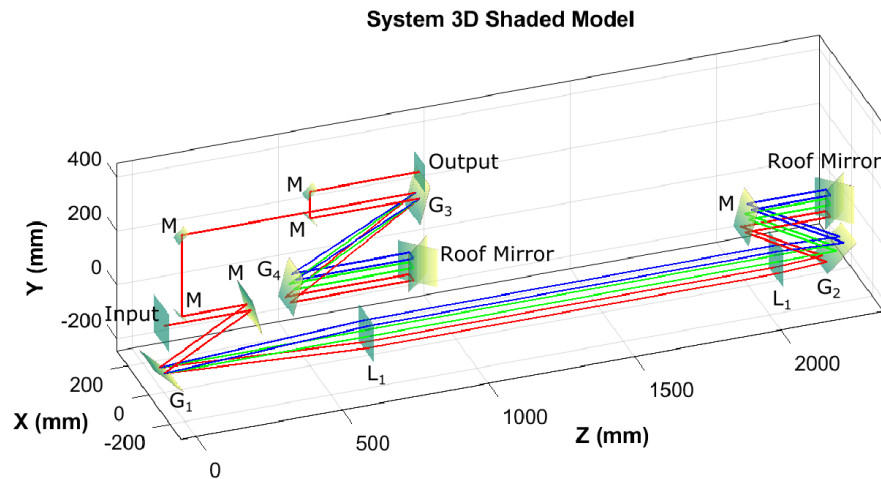


Figure 4.45: The system layout of the stretcher-compressor setup. The roof mirror reflectors are used to reflect the pulse back in a different path to enable separation of the input and output beams. Labels: G (grating), L (lens), M (plane mirror).

placed at  $l_2 = 500\text{mm}$  from the focal point of the  $2^{\text{nd}}$  lens. By applying the concept of group path length discussed in section 3.2.3 and 3.2.4, for the diffraction grating during the ray tracing and using the finite difference method to compute the derivatives, it is possible to compute all dispersion coefficients of the compressor and stretcher. In Fig. 4.46 and 4.47 the group delay dispersion (GDD) and the third-order dispersion (TOD) of the double pass Treacy grating pair and the Martinez stretcher are plotted, respectively. For comparison, the GDD and TOD computed using the geometric ray tracing are shown together with that computed using the analytical formulas given in the literature [4, 99]. For the Treacy stretcher, the dispersion computed using ray

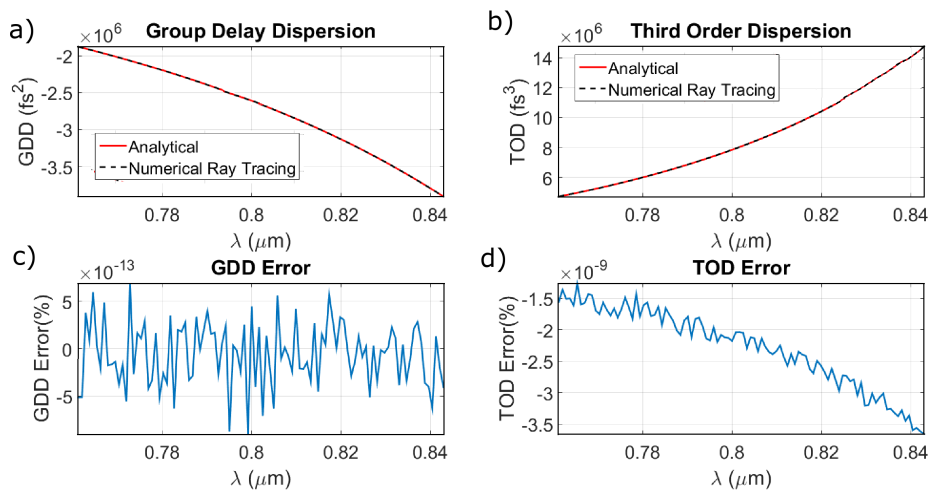


Figure 4.46: a) The GDD and b) the TOD of the Treacy compressor computed using geometrical ray tracing together with the result computed using analytical formula [4, 99]. The numerical difference between the two results is shown in (c) and (d) respectively.

tracing strongly agrees with the analytical result. However, for the Martinez stretcher the residual error is slightly larger for wavelengths different from the central wavelength due to the fact that the analytical formula assumes the ray direction is horizontal after the first grating which is only satisfied for the central wavelength. By comparing

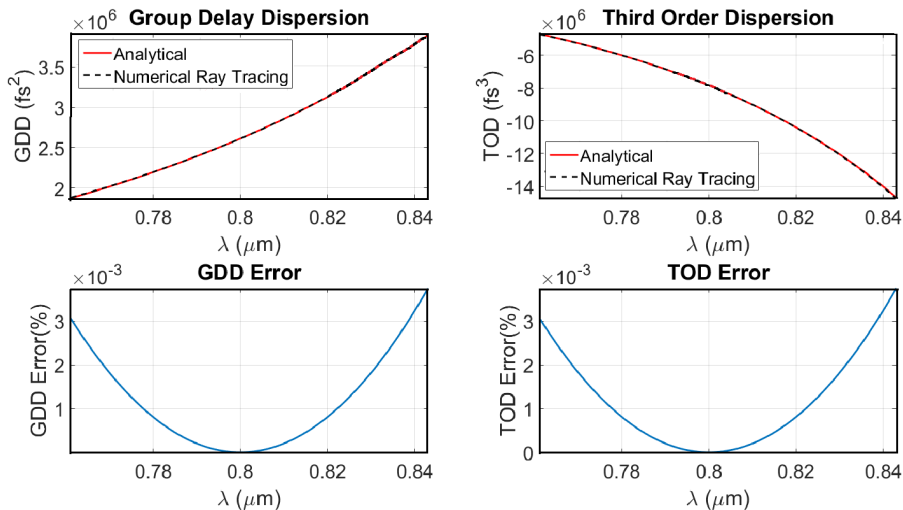


Figure 4.47: The same as in Fig. 4.46 but now computed for the Martinez grating pair with internal dispersion less telescope.

Fig. 4.47 and Fig. 4.46, it can be seen that the dispersion coefficients of the Treacy compressor are compensated by that of the Martinez stretcher for all wavelengths.

To study the first-order wave optical spatio-temporal property of the pulse stretcher-compressor setup, a single pilot GPB with a central wavelength of  $800\text{nm}$ , spatial width  $2\text{mm}$ , and temporal width of  $50\text{fs}$  has been propagated. The spatio-temporal profile of the input GPB together with that of the pulsed beam after the double pass of the stretcher and at the end of the complete setup is shown in Fig. 4.48. From Fig. 4.48, it can be seen that, the Martinez stretcher has stretched the GP from  $50\text{fs}$  to  $98752.88\text{fs}$  which reduces the peak amplitude to about 2% of the initial value. Hence the peak intensity is reduced by four orders of magnitude which allows an amplification to a high power without significant phase distortion and non-linearity effects in the amplifier medium. During the propagation of the stretched pulse through the Treacy compressor, all the dispersion effects of the Martinez stretcher are reversed and the pulse is compressed back to the original transform-limited temporal width of  $50\text{fs}$  as shown in Fig. 4.48d.

In real CPA systems, the dispersions in the stretcher-compressor pairs are not perfectly compensated due to the dispersion from a real telescope systems and misalignments of

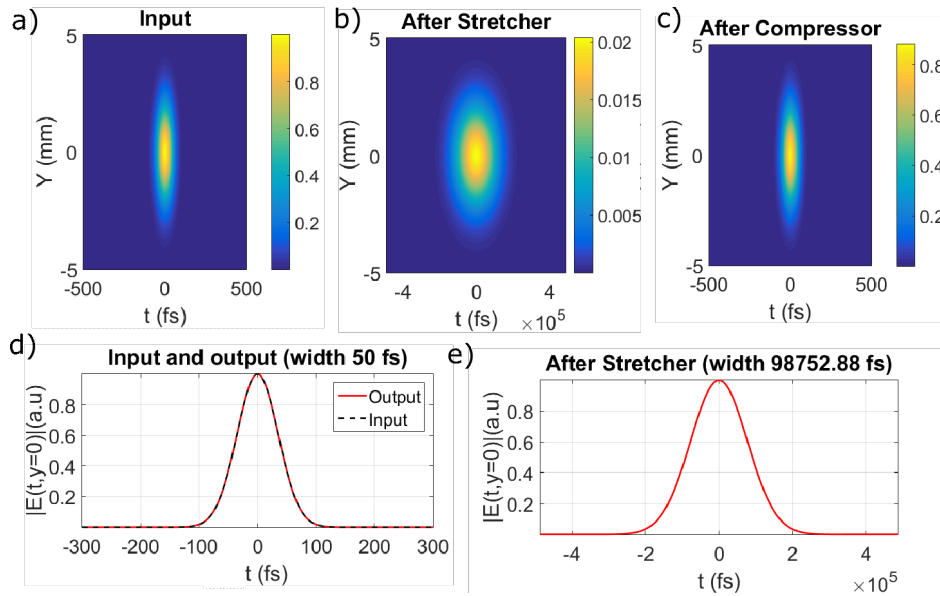


Figure 4.48: The spatio-temporal profile of the ultrashort pulse a) at the input plane, b) after the double pass through the stretcher and c) after the complete stretcher-compressor setup. The temporal amplitude profiles at the center ( $x=y=0$ ) at d) the input and the output planes and e) the intermediate plane after double pass through the stretcher.

different components. In this section the effect of using a real lens for the telescope in Martinez stretcher is studied by performing wave optical propagation using the GPBD method. The dispersion due to propagation through the glass disturbs the dispersion balance of the ideal stretcher-compressor setup. In addition to that, the aberrations on the focusing optics may also introduce phase errors since the spectral components are separated inside the stretcher [4]. For the refractive lens, a plano-convex cylindrical lens with  $R_{1x} = R_{1y} = \infty$ ,  $R_{2x} = \infty$  and  $R_{2y} = -357.54\text{mm}$ , glass of BK7 with central thickness of  $10\text{mm}$  (resulting in focal length of  $f = 700\text{mm}$  for central wavelength) has been used. After the real lenses are inserted, the thickness  $l_2$  from the second lens to the second grating of the stretcher has been readjusted so that the GDD (lower-order dispersion) of the stretcher is canceled by that of the compressor for the central wavelength. The resulting stretcher-compressor setup has no residual GDD for the central wavelength but has significant higher-order dispersions for all wavelengths and also residual GDD for wavelengths different from the central wavelength as shown in Fig. 4.49.

Now consider the propagation of an ultrashort pulsed beam which has a uniform spatial amplitude truncated by a circular aperture of radius  $2\text{mm}$  at the input plane and has a Gaussian temporal profile with the temporal width of  $50\text{fs}$  and the central wavelength

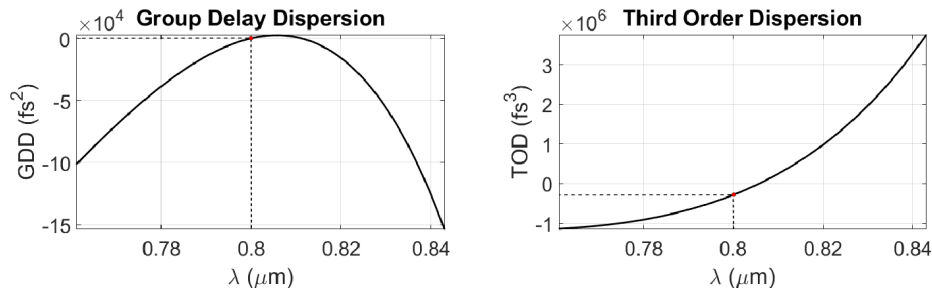


Figure 4.49: a) The GDD and b) the TOD of the complete CPA setup with real refractive lenses.

of  $800\text{nm}$  through a real stretcher-compressor pair. First the input pulse is decomposed into a set of 9000 GPBs (with  $20 \times 20$  full GBs and 50 truncated GBs in the spatial and 20 GPs in the spectral domain). By propagating all GPBs through the complete

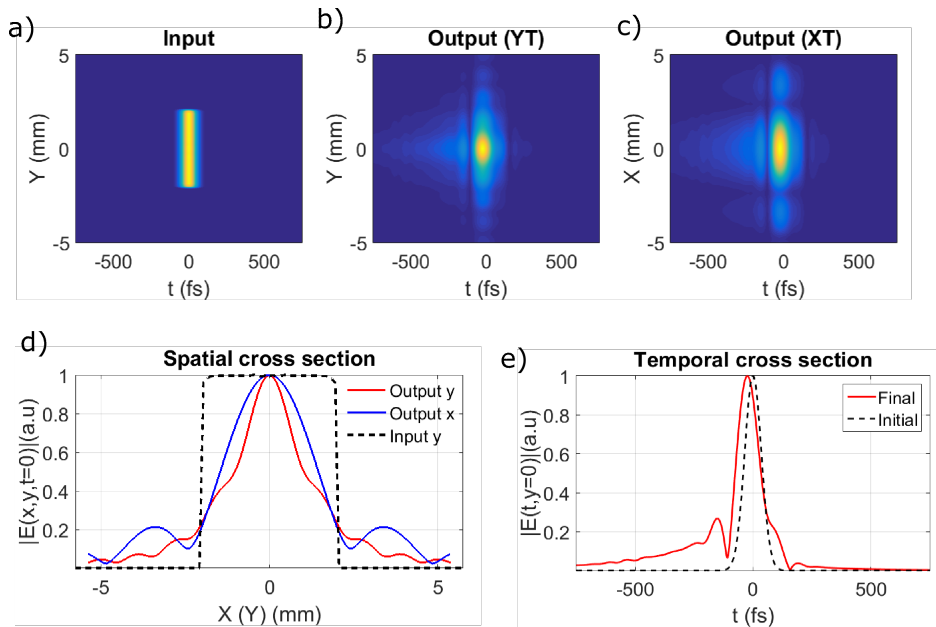


Figure 4.50: The spatio-temporal amplitude profiles of a) the input pulse b) the y-cross-section and c) the x-cross-section of the output pulse after the complete CPA setup with real lens. The comparison of d) the spatial and d) the temporal cross-sections of the input and output pulse amplitude profiles.

optical system independently and performing the phase correct superposition at the final output plane, the spatio-temporal profile of the output pulse whose cross-sectional plots are shown in Fig. 4.50 has been obtained. Due to the residual higher-order dispersion, the output pulse has a non-Gaussian temporal profile with a pulse width of about  $63.5\text{fs}$  which is greater than the transform-limited width. The asymmetrical temporal cross-section in Fig. 4.50c indicates that the output pulse is dominated by the residual TOD of the CPA system coming from the refractive lenses.

From Fig. 4.50 it can also be seen that the spatial amplitude profile of the input pulse has also been significantly altered due to the diffraction during the long-distance propagation of through the complete CPA system. The final spatial cross-section resembles the far-field diffraction of circular aperture. The slight difference in the x- and y-cross-section of the spatial amplitude profile, shown in Fig. 4.50d, comes from the fact that the lenses are used in the Martinez compressor are cylindrical which affect the two cross-sections differently. As the GPBD method uses real ray tracing for the propagation of individual GPBs, it can be used to model the effects of the misalignment (tilt and decenter in 3D) and mismatches in the stretcher and compressor components on the output pulse by the wave optical propagation.

### 4.3 Further discussions

#### Computation time of the GBD/GPBD methods

As the electric field values for the final field are computed independently for each analysis point by adding the individual contributions from all GBs/GPBs used, the speed of the overall algorithm is determined by the number of GBs/GPBs used and the number of spatial or temporal points used for the analysis. To improve the computation speed by full utilization of all available CPU cores in parallel, specialized Mex functions [102] for the GB/GPB superposition have been written using the C language with the OpenMP library [103] for the parallel computing in the Matlab implementation of the algorithms. Furthermore, by computing the distances of the analysis points from the corresponding GB/GPB center, the unnecessary computations for analysis points that are very far from the centers and hence have very negligible amplitudes are avoided. Table (4.1) shows the total computation time (for decomposition, propagation, and superposition) of the GBD and GPBD methods for some selected example results given in the previous subsections using a computer with an Intel Core-i7 CPU at 2.9 GHz and 16 GB RAM.

Example results	No. of GBs/GPBs	Analysis points	Time taken
Fig. 4.10	$45 \times 45$ GBs	2048 in 1D	3.8 sec
Fig. 4.13a	$50 \times 50$ GBs	$101 \times 101$	57.1 sec
Fig. 4.50b/c	9000 GPBs	$101 \times 101$	17.9 sec

Table 4.1: Computation time of the GBD and GPBD method for few selected examples.

As discussed in subsection (3.2.6), the time taken for computing the temporal profile is less than that required for computing the spatial profiles of a pulse for equal number

of analysis points and GPBs. This is the reason for the short computation time of the spatio-temporal (y-t) pulse profile in Fig. 4.50b/c even using 9000 GPBs.

### Pros and cons of the GBD and GPBD methods

Compared to the conventional field propagation methods based on the FTs, the GBD and GPBD methods have several advantages which make them attractive to different wave optical modeling problems. Some of these advantages include their abilities to :

- decompose and hence propagate initial fields with large aberration and large spectral phases. In the FTs based propagation methods, the number of samples required to fulfill the Nyquist sampling criteria for such initial fields is too large due to the fast oscillating wrapped phase in the complex field [12, 13, 104]. In addition to that, zero padding is usually applied to the initial field to get the finer sampling of the propagated field which further increases the number of samples required. Assuming that two sampling points are taken within a single period of the fast oscillating wrapped phase, which is the minimum requirement for the proper sampling, the minimum number of sampling points required for propagating the converging wavefront with the spherical aberration of  $100\lambda$  (discussed in subsection (4.1.3)) is  $28952 \times 28952$ . A similar argument applies for the decomposition of ultrashort pulses with large initial spectral phases [12, 13].
- perform the wave optical modeling of optical systems with large aberration, dispersions, and spatio-temporal distortions. Due to the strict sampling requirement, the FT based propagation methods are usually applicable for modeling optical systems with small phase distortions (both spatial and temporal).
- calculate the propagated field at analysis points on any arbitrarily tilted and curved surface without an additional effort. In the FT based methods, the computation of field values on a set of analysis points that are not in the same transversal plane, in general, require the computation of the entire 2D field on the transversal planes containing each analysis points. Although there is a quasi-fast FT based algorithm for propagating fields to tilted planes [16], the calculation of a field on generally curved surfaces is usually computationally intensive.
- perform accurate analytical modeling of the sharp edge diffraction of fields after a hard aperture. In the FT based field propagation methods, an accurate modeling of the sharp edge diffraction after a hard aperture, theoretically, requires an infinite number of sampling points to capture the infinite spatial frequency at the

sharp edge. Hence, using a finite number of sampling points limits the maximum spatial frequency that can be represented. However, in the GBD and GPBD methods, the field after hard aperture is represented with the spatially truncated GBs(GPBs) and the sharp edge diffraction is computed accurately using the analytical propagation equations.

Although the GBD and GPBD methods have advantages listed above, they has also certain drawbacks and limitations which restrict their application. The main drawbacks and limitations are discussed below.

- The decomposition of an input field into a set of GBs (GPBs) is not unique and there is no well-defined sampling rule equivalent to the Nyquist sampling theorem of the FT. This makes it difficult to determine the exact number of GBs (GPBs) required and sufficient for the wave optical modeling of a given system.
- The GBD and GPBD methods assume that the local paraxial and quadratic approximation is valid for each GB (GPB) as it propagates through the optical system. That is when the aberration seen by the individual GB and/or the spectral phase seen by the individual GPB is too large to be represented with quadratic approximation, then the standard propagation equations used for each GB (GPB) are no longer valid and hence, the results obtained from the GBD and GPBD methods become inaccurate.
- For optical systems with multiple apertures or when the elementary GBs/GPBs become non-paraxial during the propagation, the intermediate field has to be recomposed into a new set of full and truncated paraxial GBs/GPBs. This re-composition usually requires a large number of GBs/GPBs to be used due to the complicated amplitude and phase profiles of the intermediate fields.
- For simple wave optical modeling problems such as the propagation of input fields with non-curved phase profiles through optical systems with small phase distortion (both spatial and spectral) or the propagation of a spherical wavefront with small aberration to the focal plane, the field propagation methods based on the FTs are computationally faster than the GBD and GPBD methods.

## 5. Conclusion and Outlook

In this work several extensions of the conventional Gaussian beam decomposition methods are accomplished. First, an algorithm for decomposing an arbitrary field with a smooth wavefront into a set of Gaussian beams with different positions, directions, and non-zero initial curvatures is presented. In the proposed method, the Gaussian beam decomposition is performed directly on the wavefront surface unlike other conventional methods that decompose the complex field on a single plane. This avoids the problem associated with the fast oscillating phase in the complex field for strongly curved wavefronts. The different directions and the non-zero initial curvature of the Gaussian beam enable the quadratic approximation of the local wavefront which in turn reduces the number of Gaussian beams required for the decomposition. The decomposition algorithm directly gives the complex curvature matrix element of the Gaussian beams which can be used directly for the propagation of the Gaussian beams in both free space and through optical systems. Then a natural extension of the monochromatic Gaussian beam decomposition method to handle the propagation of ultrashort pulses through a general optical system is proposed. In the extended method, an input ultra-short pulse is propagated through an optical system by decomposing it into a set of Gaussian pulsed beams with different positions, directions, initial curvatures, group delays, and temporal chirps. The method of determining the initial Gaussian pulsed beam parameters from the given arbitrary spatial and spectral amplitude and phase profiles is described. Each Gaussian pulsed beam represents the local spatial and spectral phase of the input pulse in the quadratic approximation. Finally, methods of computing the spatio-temporal and spatio-spectral profiles of the propagated pulses from the phase correct superposition of the spatio-temporal and spatio-spectral of the individual Gaussian pulsed beams are discussed.

Furthermore, in this work a method to overcome one of the main limitations of the Gaussian beam decomposition method, its inability to accurately model sharp edge diffraction of field after hard apertures, is proposed. To this end a special kind of elementary beam, known as the truncated Gaussian beam which represents a Gaussian beam truncated by a semi-infinite hard aperture, is introduced. The analytical propagation equation for its propagation through a non-orthogonal paraxial optical system is derived from the Collin's integral. Using the truncated Gaussian beams, the conventional Gaussian beam decomposition method is extended to accurately model the



diffraction of monochromatic fields after hard apertures. Similarly, for pulsed beams, a spatially truncated Gaussian pulsed beam is introduced and its analytical propagation equation through a dispersive paraxial optical system is derived. With the help of the spatially truncated Gaussian pulsed beams, the application of the conventional Gaussian pulsed beam decomposition method is then extended to the modeling of the diffraction of an arbitrary ultrashort pulse after a hard aperture. Finally, the three-dimensional polarization ray-tracing calculus is combined with the Gaussian beam decomposition method to enable propagation of vectorial fields through optical systems, such as high numerical aperture focusing, which affect the polarization state of the light.

The validity and accuracy of the proposed methods are assessed by performing example diffraction calculations and comparing the results with that obtained from the independent calculation by using other field propagation methods and previously published results. The applications of the proposed algorithms are demonstrated by performing propagation of fields through optical systems which are rather complicated to handle with the conventional Fourier transform-based propagation methods. Some of the example calculations presented above employ the combination of two or more extension methods developed in this work. The following table summarizes the methods used for different examples presented.

	Subsections where the examples are given				
	(4.1.4)	(4.1.2) & (4.1.3)	(4.1.5)	(4.2.4) & (4.2.5)	(4.2.3) & (4.2.6)
GBD method (modified)	×	×	×	-	-
Truncated GB	-	×	×	-	-
GPBD method	-	-	-	×	×
Truncated GPB	-	-	-	-	×
Vectorial extension	-	-	×	-	-

Table 5.1: Summary of extended methods used in different example calculations presented in this work. The methods used for the example calculations are indicated with a cross sign.

Several extensions of the Gaussian beam decomposition and the Gaussian pulsed beam decomposition methods are possible. One extension would be to improve the decomposition algorithms of the spatial and spectral profiles by using adaptive sampling methods for generating a non-uniformly distributed Gaussian beams and Gaussian pulses depending on the complexity of the local field profile. This helps in reducing the

---

number of Gaussian beams and pulses required for decomposing a given input field. Another would be to define a spectrally truncated Gaussian pulsed beam for which the spectral profile is truncated instead of the spatial profile, which has been presented in this work. This enables the Gaussian pulsed beam decomposition method to model the propagation of ultrashort pulses with spectral hard edges. Finally, the application of the GBD and GPBD methods can be extended to optical systems containing diffractive optical elements (DOE) with variable groove densities and diffraction efficiencies. In this work, for simplicity, the groove width and the diffraction efficiency of the grating have been assumed to be constant across the whole grating surface. However, in principle, one can use different groove widths and diffraction efficiencies for the propagation of each GB or GPB depending on their intersection point with the given diffraction grating.

## Bibliography

- [1] M. Born and E. Wolf, *Principles of optics: electromagnetic theory of propagation, interference and diffraction of light*. Elsevier, 2013.
- [2] T. A. Edison, “Electric lamp (us patent 223,898),” 1880.
- [3] A. E. Siegman, “Linear pulse propagation,” in *Lasers*, pp. 331–361, University science books, 1986.
- [4] A. Weiner, *Ultrafast optics*, vol. 72. John Wiley & Sons, 2011.
- [5] B. E. Saleh and M. C. Teich, *Fundamentals of photonics*. John Wiley & Sons, 2019.
- [6] S. Nolte, M. Will, J. Burghoff, and A. Tünnermann, “Ultrafast laser processing: new options for three-dimensional photonic structures,” *Journal of Modern Optics*, vol. 51, no. 16-18, pp. 2533–2542, 2004.
- [7] A. April, “Ultrashort, strongly focused laser pulses in free space,” in *Coherence and Ultrashort Pulse Laser Emission*, pp. 355–382, IntechOpen, 2010.
- [8] U. Fuchs, U. D. Zeitner, and A. Tünnermann, “Ultra-short pulse propagation in complex optical systems,” *Optics Express*, vol. 13, no. 10, pp. 3852–3861, 2005.
- [9] F. Wyrowski, C. Hellmann, R. Krieg, and H. Schweitzer, “Modeling the propagation of ultrashort pulses through optical systems,” in *Frontiers in Ultrafast Optics*, vol. 7589, p. 758900, International Society for Optics and Photonics, 2010.
- [10] F. Wyrowski and M. Kuhn, “Unified optical modeling,” in *International Optical Design Conference*, p. IWC1, Optical Society of America, 2010.
- [11] B. Webb, M. Guardalben, C. Dorrer, S. Bucht, and J. Bromage, “Simulation of grating compressor misalignment tolerances and mitigation strategies for chirped-pulse-amplification systems of varying bandwidths and beam sizes,” *Applied optics*, vol. 58, no. 2, pp. 234–243, 2019.
- [12] S. P. Veetil, H. Schimmel, F. Wyrowski, and C. Vijayan, “Wave optical modelling of focusing of an ultra short pulse,” *Journal of Modern Optics*, vol. 53, no. 15, pp. 2187–2194, 2006.

- 
- [13] S. P. Veetil, C. Vijayan, D. Sharma, H. Schimmel, and F. Wyrowski, “Sampling rules in the frequency domain for numerical propagation of ultrashort pulses through linear dielectrics,” *JOSA B*, vol. 23, no. 10, pp. 2227–2236, 2006.
- [14] B. Stone and T. Bruegge, “Practical considerations for simulating beam propagation: a comparison of three approaches,” in *International Optical Design Conference*, p. IWA3, Optical Society of America, 2002.
- [15] S. Backus, C. G. Durfee III, M. M. Murnane, and H. C. Kapteyn, “High power ultrafast lasers,” *Review of scientific instruments*, vol. 69, no. 3, pp. 1207–1223, 1998.
- [16] J. Stock, N. G. Worku, and H. Gross, “Coherent field propagation between tilted planes,” *JOSA A*, vol. 34, no. 10, pp. 1849–1855, 2017.
- [17] K. Matsushima, H. Schimmel, and F. Wyrowski, “Fast calculation method for optical diffraction on tilted planes by use of the angular spectrum of plane waves,” *JOSA A*, vol. 20, no. 9, pp. 1755–1762, 2003.
- [18] S. Zhang, D. Asoubar, C. Hellmann, and F. Wyrowski, “Propagation of electromagnetic fields between non-parallel planes: a fully vectorial formulation and an efficient implementation,” *Applied optics*, vol. 55, no. 3, pp. 529–538, 2016.
- [19] A. W. Greynolds, “Propagation of generally astigmatic Gaussian beams along skew ray paths,” in *Diffraction Phenomena in Optical Engineering Applications*, vol. 560, pp. 33–52, International Society for Optics and Photonics, 1986.
- [20] J. E. Harvey, R. G. Irvin, and R. N. Pfisterer, “Modeling physical optics phenomena by complex ray tracing,” *Optical Engineering*, vol. 54, no. 3, p. 035105, 2015.
- [21] A. W. Greynolds, “Fat rays revisited: a synthesis of physical and geometrical optics with gaußlets,” in *International Optical Design Conference, Optical Society of America*, 2014.
- [22] Synopsys, Inc, “Code v beam synthesis propagation,” 2018.
- [23] Photon Engineering, LLC, “Physical optics modeling with FRED,” 2020.
- [24] Breault Research Organization, “Physical optics in ASAP,” 2015.

- [25] M. J. Bastiaans, "Gabor's signal expansion based on a nonorthogonal sampling geometry," in *Optical Processing and Computing: A Tribute to Adolf Lohmann*, vol. 4392, pp. 46–60, International Society for Optics and Photonics, 2001.
- [26] P. Einziger, S. Raz, and M. Shapira, "Gabor representation and aperture theory," *JOSA A*, vol. 3, no. 4, pp. 508–522, 1986.
- [27] A. Rohani, A. Shishegar, and S. Safavi-Naeini, "A fast gaussian beam tracing method for reflection and refraction of general vectorial astigmatic gaussian beams from general curved surfaces," *Optics communications*, vol. 232, no. 1-6, pp. 1–10, 2004.
- [28] M. May, J. F. Morhange, and C. Hirlimann, "Wave group decomposition of ultrashort light pulses," *Optics Letters*, vol. 18, no. 5, pp. 364–366, 1993.
- [29] M. Khelladi, O. Seddiki, and F. T. Bendimerad, "Time-frequency decomposition of an ultrashort pulse: wavelet decomposition," *Radioengineering*, vol. 17, no. 1, pp. 56–63, 2008.
- [30] J. C. Diels and W. Rudolph, *Ultrashort Laser Pulse Phenomena*. Elsevier Inc, 2 ed., 2006.
- [31] A. M. Weiner, *Ultrafast optics*. Wiley, 2009.
- [32] R. Trebino, *Frequency-Resolved Optical Gating: The Measurement of Ultrashort Laser Pulses*. 2002.
- [33] D. C. O'Shea, "Group velocity dispersion using commercial optical design programs," *Applied optics*, vol. 45, pp. 4740–4746, 2006.
- [34] S. Aktürk, X. Gu, P. Bowlan, and R. Trebino, "Spatio-temporal couplings in ultrashort laser pulses," *Journal of Optics*, vol. 12, p. 93001, 2010.
- [35] S. Aktürk, X. Gu, P. Gabolde, and R. Trebino, "The general theory of first-order spatio-temporal distortions of Gaussian pulses and beams," *Optics Express*, vol. 13, no. 21, pp. 8642–8661, 2005.
- [36] S. Aktürk, X. Gu, P. Gabolde, and R. Trebino, "First-order spatiotemporal distortions of gaussian pulses and beams," *Springer Series in Optical Sciences*, vol. 132, no. 21, pp. 233–239, 2007.

- [37] V. Chauhan, P. Bowlan, J. Cohen, and R. Trebino, "Single-diffraction-grating and grism pulse compressors," *Journal of the Optical Society of America*, vol. 27, no. 4, p. 619, 2010.
- [38] Y. Sutoh, Y. Yasuno, K. Harada, M. Itoh, T. Yatagai, and M. Mori, "Analysis of spatiotemporal coupling in a femtosecond pulse shaper by the Wigner distribution function," *Optical Engineering*, vol. 40, p. 1717, 2001.
- [39] G. Spencer and M. Murty, "General ray-tracing procedure," *JOSA*, vol. 52, no. 6, pp. 672–678, 1962.
- [40] F. Wyrowski and C. Hellmann, "Geometrical optics reloaded: Physical optics modeling with smart rays," *Optik & Photonik*, vol. 10, no. 5, pp. 43–47, 2015.
- [41] D. Malacara-Hernández and Z. Malacara-Hernández, *Handbook of optical design*. CRC Press, 2017.
- [42] J.-C. Diels and W. Rudolph, *Ultrashort laser pulse phenomena*. Elsevier, 2006.
- [43] S. P. Dijaili, A. Dienes, and J. S. Smith, "Abcd matrices for dispersive pulse propagation," *IEEE Journal of Quantum Electronics*, vol. 26, no. 6, pp. 1158–1164, 1990.
- [44] Q. Lin, S. Wang, J. Alda, and E. Bernabeu, "Spatial-temporal coupling in a grating-pair pulse compression system analysed by matrix optics," *Optical and Quantum Electronics*, vol. 27, no. 9, pp. 785–798, 1995.
- [45] J. Arnaud, "Nonorthogonal optical waveguides and resonators," *Bell System Technical Journal*, vol. 49, no. 9, pp. 2311–2348, 1970.
- [46] A. Kostenbauder, "Ray-pulse matrices: a rational treatment for dispersive optical systems," *IEEE Journal of Quantum Electronics*, vol. 26, no. 6, pp. 1148–1157, 1990.
- [47] G. Marcus, "Spatial and temporal pulse propagation for dispersive paraxial optical systems," *Optics Express*, vol. 24, no. 7, pp. 7752–7766, 2016.
- [48] Y. Cai and Q. Lin, "The elliptical Hermite–Gaussian beam and its propagation through paraxial systems," *Optics Communications*, vol. 207, no. 1-6, pp. 139–147, 2002.

- [49] Q. Lin and L. Wang, "Collins formula and tensor abcd law in spatial-frequency domain," *Optics Communications*, vol. 185, no. 4-6, pp. 263–269, 2000.
- [50] G. Kostenbauder, "Ray-pulse matrices - a simple formulation for dispersive optical systems," *Proceedings of SPIE*, vol. 1209, no. 6, pp. 136–139, 1990.
- [51] F. Wyrowski and M. Kuhn, "Introduction to field tracing," *Journal of Modern Optics*, vol. 58, no. 5-6, pp. 449–466, 2011.
- [52] Y. M. Engelberg and S. Ruschin, "Fast method for physical optics propagation of high-numerical-aperture beams," *JOSA A*, vol. 21, no. 11, pp. 2135–2145, 2004.
- [53] N. G. Worku, R. Hambach, and H. Gross, "Decomposition of a field with smooth wavefront into a set of Gaussian beams with non-zero curvatures," *JOSA A*, vol. 35, no. 7, pp. 1091–1102, 2018.
- [54] M. J. Bastiaans, "The expansion of an optical signal into a discrete set of gaussian beams," in *Erzeugung und Analyse von Bildern und Strukturen*, pp. 23–32, Springer, 1980.
- [55] G. E. Fasshauer, *Meshfree approximation methods with MATLAB*, vol. 6. World Scientific, 2007.
- [56] J. Arnaud, "Representation of gaussian beams by complex rays," *Applied optics*, vol. 24, no. 4, pp. 538–543, 1985.
- [57] R. Wilhelm, B. Koehler, U. Johann, M. Kersten, and R. Schwarz, "Beamwarrior: advanced optical analysis for integrated modeling," in *Integrated Modeling of Telescopes*, vol. 4757, pp. 113–123, International Society for Optics and Photonics, 2002.
- [58] G. Yun, K. Crabtree, and R. A. Chipman, "Properties of the polarization ray tracing matrix," in *Polarization Science and Remote Sensing III*, vol. 6682, p. 66820Z, International Society for Optics and Photonics, 2007.
- [59] G. Yun, K. Crabtree, and R. A. Chipman, "Three-dimensional polarization ray-tracing calculus i: definition and diattenuation," *Applied optics*, vol. 50, no. 18, pp. 2855–2865, 2011.
- [60] M. Leutenegger, R. Rao, R. A. Leitgeb, and T. Lasser, "Fast focus field calculations," *Optics express*, vol. 14, no. 23, pp. 11277–11291, 2006.

- 
- [61] W. Singer, M. Totzeck, and H. Gross, *Handbook of optical systems, volume 2: Physical image formation*. John Wiley & Sons, 2006.
- [62] N. Worku and H. Gross, “Vectorial field propagation through high na objectives using polarized gaussian beam decomposition,” in *Optical Trapping and Optical Micromanipulation XIV*, vol. 10347, p. 103470W, International Society for Optics and Photonics, 2017.
- [63] N. G. Worku and H. Gross, “Gaussian pulsed beam decomposition for propagation of ultrashort pulses through optical systems,” *JOSA A*, vol. 37, no. 1, pp. 98–107, 2020.
- [64] N. G. Worku and H. Gross, “Spatially truncated Gaussian pulsed beam and its application in modeling diffraction of ultrashort pulses from hard apertures,” *JOSA A*, vol. 37, no. 2, pp. 317–326, 2020.
- [65] N. G. Worku and H. Gross, “Propagation of truncated Gaussian beams and their application in modeling sharp-edge diffraction,” *JOSA A*, vol. 36, no. 5, pp. 859–868, 2019.
- [66] J. Stock, A. Broemel, J. Hartung, D. Ochse, and H. Gross, “Description and reimplementaion of real freeform surfaces,” *Applied optics*, vol. 56, no. 3, pp. 391–396, 2017.
- [67] M. Cywiak, D. Cywiak, and E. Yáñez, “Finite Gaussian wavelet superposition and fresnel diffraction integral for calculating the propagation of truncated, non-diffracting and accelerating beams,” *Optics Communications*, vol. 405, pp. 132–142, 2017.
- [68] Z. Bor, “Distortion of femtosecond laser pulses in lenses,” *Optics Letters*, vol. 14, no. 2, pp. 119–121, 1989.
- [69] D. C. O’Shea, T. J. Suleski, A. D. Kathman, and D. W. Prather, *Diffractive optics: design, fabrication, and test*, vol. 62. SPIE press, 2004.
- [70] J. Turunen and J. Tervo, “Fourier modal method and its applications to inverse diffraction, near-field imaging, and nonlinear optics,” in *Fringe 2013*, pp. 25–33, Springer, 2014.
- [71] H. Kim, J. Park, and B. Lee, *Fourier modal method and its applications in computational nanophotonics*. CRC Press, 2017.



- [72] W. Welford, "Tracing skew rays through concave diffraction gratings," *Optica Acta: International Journal of Optics*, vol. 9, no. 4, pp. 389–394, 1962.
- [73] M. Seesselberg, B. H. Kleemann, and J. Ruoff, "Validity of ray trace based performance predictions of optical systems with diffractive optical elements (doe)," in *Optical Modeling and Performance Predictions VIII*, vol. 9953, p. 995306, International Society for Optics and Photonics, 2016.
- [74] S. Wise, V. Quetschke, A. Deshpande, G. Mueller, D. Reitze, D. Tanner, B. Whiting, Y. Chen, A. Tünnermann, E. Kley, *et al.*, "Phase effects in the diffraction of light: beyond the grating equation," *Physical review letters*, vol. 95, no. 1, p. 013901, 2005.
- [75] J. J. Huang, L. Y. Zhang, and Y. Q. Yang, "Reinvestigation on the frequency dispersion of a grating-pair compressor," *Optics Express*, vol. 19, no. 2, pp. 814–819, 2011.
- [76] E. Treacy, "Optical pulse compression with diffraction gratings," *IEEE Journal of quantum Electronics*, vol. 5, no. 9, pp. 454–458, 1969.
- [77] Z. Wang, Z. Zhang, Z. Xu, and Q. Lin, "Space-time profiles of an ultrashort pulsed Gaussian beam," *IEEE Journal of Quantum Electronics*, vol. 33, no. 4, pp. 566–573, 1997.
- [78] M. A. Porras, "Ultrashort pulsed Gaussian light beams," *Physical Review E*, vol. 58, no. 1, p. 1086, 1998.
- [79] C. Caron and R. Potvliege, "Free-space propagation of ultrashort pulses: space-time couplings in Gaussian pulse beams," *Journal of Modern Optics*, vol. 46, no. 13, pp. 1881–1891, 1999.
- [80] S. Akturk, X. Gu, P. Bownan, and R. Trebino, "Spatio-temporal couplings in ultrashort laser pulses," *Journal of Optics*, vol. 12, no. 9, p. 093001, 2010.
- [81] S. A. Collins, "Lens-system diffraction integral written in terms of matrix optics," *JOSA*, vol. 60, no. 9, pp. 1168–1177, 1970.
- [82] Steven G. Johnson, "Faddeeva Package," 2012.

- [83] M. Cywiak, A. Morales, M. Servín, and R. Gómez-Medina, “A technique for calculating the amplitude distribution of propagated fields by Gaussian sampling,” *Optics Express*, vol. 18, no. 18, pp. 19141–19155, 2010.
- [84] V. Nourrit, P. Chanclou, *et al.*, “Propagation and diffraction of truncated gaussian beams,” *JOSA A*, vol. 18, no. 3, pp. 546–556, 2001.
- [85] M. Mansuripur, “Distribution of light at and near the focus of high-numerical-aperture objectives,” *JOSA A*, vol. 3, no. 12, pp. 2086–2093, 1986.
- [86] M. Mansuripur, “Distribution of light at and near the focus of high-numerical-aperture objectives: erratum certain computational aspects of vector diffraction problems: erratum,” *JOSA A*, vol. 10, no. 2, pp. 382–383, 1993.
- [87] Y. Li, “Dependence of the focal shift on fresnel number and f number,” *JOSA*, vol. 72, no. 6, pp. 770–774, 1982.
- [88] Y. Li and E. Wolf, “Focal shifts in diffracted converging spherical waves,” *Optics Communications*, vol. 39, no. 4, pp. 211–215, 1981.
- [89] Y. Li, “Focal shifts in diffracted converging electromagnetic waves. i. kirchhoff theory,” *JOSA A*, vol. 22, no. 1, pp. 68–76, 2005.
- [90] N. G. Worku and H. Gross, “Application of gaussian pulsed beam decomposition in modeling optical systems with diffraction grating,” *JOSA A*, vol. 37, no. 5, pp. 797–806, 2020.
- [91] Z. Horváth and Z. Bor, “Diffraction of short pulses with boundary diffraction wave theory,” *Physical Review E*, vol. 63, no. 2, p. 26601, 2001.
- [92] Z. Bor and Z. Horvath, “Distortion of femtosecond pulses in lenses. wave optical description,” *Optics communications*, vol. 94, no. 4, pp. 249–258, 1992.
- [93] Thorlabs, “Unmounted aspheric lens 354240-b - f = 8.00 mm, na = 0.5, arc: 600 - 1050 nm,” 2009.
- [94] Thorlabs, “Axicon ax252-b 2.0°, 650 - 1050 nm ar coated uvfs, ø1” (ø25.4 mm),” 2009.
- [95] H. Sõnajalg and P. Saari, “Suppression of temporal spread of ultrashort pulses in dispersive media by Bessel beam generators,” *Optics letters*, vol. 21, no. 15, pp. 1162–1164, 1996.

- [96] P. Saari and H. Sõnajalg, “Pulsed Bessel beams,” *Laser Physics*, vol. 7, no. 1, pp. 32–39, 1997.
- [97] P. Bowlan, H. Valtna-Lukner, M. Lõhmus, P. Piksarv, P. Saari, and R. Trebino, “Measuring the spatiotemporal field of ultrashort Bessel-X pulses,” *Optics Letters*, vol. 34, no. 15, pp. 2276–2278, 2009.
- [98] R. J. Mahon and J. A. Murphy, “Simulated propagation of ultrashort pulses modulated by low-fresnel-number lenses using truncated series expansions,” *Applied Optics*, vol. 53, no. 25, pp. 5701–5711, 2014.
- [99] R. L. Fork, C. B. Cruz, P. Becker, and C. V. Shank, “Compression of optical pulses to six femtoseconds by using cubic phase compensation,” *Optics letters*, vol. 12, no. 7, pp. 483–485, 1987.
- [100] C. Barty, C. Gordon, and B. Lemoff, “Multiterawatt 30-fs ti: sapphire laser system,” *Optics letters*, vol. 19, no. 18, pp. 1442–1444, 1994.
- [101] O. Martinez, “3000 times grating compressor with positive group velocity dispersion: Application to fiber compensation in 1.3-1.6  $\mu\text{m}$  region,” *IEEE Journal of Quantum Electronics*, vol. 23, no. 1, pp. 59–64, 1987.
- [102] MathsWorks, “MEX File Functions.”
- [103] O. A. R. Board, “Openmp application programming interface.”
- [104] J. D. Schmidt, *Numerical simulation of optical wave propagation with examples in MATLAB*. SPIE Bellingham, Washington, USA, 2010.
- [105] C. Zheng, “Propagation of elliptical gaussian beam passing through apertured paraxial optical systems,” *Optik-International Journal for Light and Electron Optics*, vol. 125, no. 1, pp. 264–267, 2014.
- [106] E. W. Ng and M. Geller, “A table of integrals of the error functions,” *Journal of Research of the National Bureau of Standards B*, vol. 73B, no. 1, pp. 1–20, 1969.
- [107] R. Navarro and J. Arines, “Complete modal representation with discrete zernike polynomials-critical sampling in non redundant grids,” *Numerical Simulations of Physical and Engineering Processes*, p. 221, 2011.
- [108] R. Swinbank and R. James Purser, “Fibonacci grids: A novel approach to global modelling,” *Quarterly Journal of the Royal Meteorological Society: A journal of*

*the atmospheric sciences, applied meteorology and physical oceanography*, vol. 132,  
no. 619, pp. 1769–1793, 2006.

## Appendix A: Derivation of the generalized paraxial wave equation

Here the derivation of the generalized paraxial wave equation given in Eq. (2.3.1) which governs the propagation of a pulsed beam in the spatio-temporal domain is shown. Consider the propagation of a given initial scalar field  $E_0(x, y, t)$  in a homogenous, isotropic medium using the angular spectrum method. The initial spectrum of the given electric field is computed by using the FT as

$$E_0(k_x, k_y, \omega) = \frac{1}{(2\pi)^3} \iiint E_0(x, y, t) \exp [i (k_x x + k_y y - \omega t)] dx dy dt, \quad (\text{A.1})$$

where  $k_x, k_y$  are the wave vector components along x and y axis. The propagation of the initial spectrum through a homogenous medium is given by

$$E(k_x, k_y, \omega; z) = E_0(k_x, k_y, \omega) \exp [-ik_z(k_x, k_y, \omega) z] \quad (\text{A.2})$$

where  $k_z(k_x, k_y, \omega) = \sqrt{k^2(\omega) - k_x^2 - k_y^2}$  is the component of the propagation constant along the propagation direction. Taking the first two terms in the Taylor expansion of the propagation factor for paraxial beam with small transversal component of the wavevector ( $k^2(\omega) \gg k_x^2 + k_y^2$ ) is approximated by

$$k_z(k_x, k_y, \omega) \approx k(\omega) - \frac{k_x^2 + k_y^2}{2k(\omega)}. \quad (\text{A.3})$$

Inserting Eq. (A.3) into Eq. (A.2), the propagated field in the spectral domain becomes

$$E(k_x, k_y, \omega; z) \approx E_0(k_x, k_y, \omega) \exp [-ik(\omega)z] \exp \left[ i \frac{k_x^2 + k_y^2}{2k(\omega)} z \right]. \quad (\text{A.4})$$

The Taylor expansion of the wavenumber  $k(\omega)$  about the central frequency  $\omega_0$  of the input field is given by

$$k(\omega) \approx k(\omega_0) + \left. \frac{\partial k}{\partial \omega} \right|_{\omega_0} (\omega - \omega_0) + \frac{1}{2} \left. \frac{\partial^2 k}{\partial \omega^2} \right|_{\omega_0} (\omega - \omega_0)^2 + \dots, \quad (\text{A.5})$$

where  $k(\omega_0)$  is the mean wavenumber,  $\left. \frac{\partial k}{\partial \omega} \right|_{\omega_0}$  is the inverse of the group velocity  $v_g$ , and  $\left. \frac{\partial^2 k}{\partial \omega^2} \right|_{\omega_0}$  is the group velocity dispersion  $D_0$  of the propagating field in the medium. For an input field whose spectral bandwidth is very narrow,  $(\omega - \omega_0) \ll \omega_0$ , the first three terms of the Taylor expansion in Eq. (A.5) can be used to approximate the wavenumber in Eq. (A.4). However, since the second exponent term in Eq. (A.4) is already small due to the paraxiality condition assumed above, just the constant term for wavenumber is used. With these approximations and replacing  $\bar{\omega} = \omega - \omega_0$ , Eq. (A.4) becomes

$$E(k_x, k_y, \omega; z) \approx E_0(k_x, k_y, \omega) \exp[-ik(\omega_0)z] \exp\left[-i\frac{1}{v_g}\bar{\omega}z\right] \tilde{H}_{FP}(k_x, k_y, \bar{\omega}; z), \quad (\text{A.6})$$

with  $\tilde{H}_{FP}(k_x, k_y, \bar{\omega}; z) = \exp\left[-iz\left(\frac{1}{2}D_0\bar{\omega}^2 - \frac{1}{2k(\omega_0)}(k_x^2 + k_y^2)\right)\right]$ . Now let's assume that the temporal envelope of the pulse is large compared to the optical cycle so that several optical cycles are enclosed inside an envelope. Hence, the slowly varying envelope approximation can be applied and the input field can be written as

$$E_0(x, y, t) = \psi_0(x, y, t) \exp(i\omega_0 t). \quad (\text{A.7})$$

From the properties of the FT, it can be seen that the spectrum of the slowly varying envelope is related to the total initial spectrum by

$$E_0(k_x, k_y, \omega) = \psi_0(k_x, k_y, \bar{\omega}). \quad (\text{A.8})$$

Inserting Eq. (A.8) into Eq. (A.6) and then taking the IFTs, both spatial and temporal, of Eq. (A.6), the propagated field in time domain is given by

$$\begin{aligned} E(x, y, t; z) &= \exp[-ik(\omega_0)z] \iiint \psi_0(k_x, k_y, \bar{\omega}) \tilde{H}_{FP}(k_x, k_y, \bar{\omega}; z) \exp\left[-i\frac{z}{v_g}\bar{\omega}\right] \\ &\quad \times \exp[-i(k_x x + k_y y - \omega t)] dk_x dk_y d\omega \\ &= \exp[-i(k(\omega_0)z - \omega_0 t)] \iiint \psi_0(k_x, k_y, \bar{\omega}) \tilde{H}_{FP}(k_x, k_y, \bar{\omega}; z) \\ &\quad \times \exp[-i(k_x x + k_y y - \bar{\omega} t)] dk_x dk_y d\bar{\omega} \\ &= \exp[-i(k(\omega_0)z - \omega_0 t)] \times \mathfrak{F}^{-1}\{\psi(k_x, k_y, \bar{\omega}, z)\} \end{aligned} \quad (\text{A.9})$$

where  $\bar{t} = t - \frac{z}{v_g}$  is the time in the reference frame which is co-moving with the wave group,  $\mathfrak{F}^{-1}\{\cdot\}$  is the triple IFT operation with  $(k_x, k_y, \bar{\omega})$  and  $(x, y, \bar{t})$  being its conjugate variables, and  $\psi(k_x, k_y, \bar{\omega}, z) = \psi_0(k_x, k_y, \bar{\omega})\tilde{H}_{FP}(k_x, k_y, \bar{\omega}; z)$  is the final propagated spectrum of the slowly varying envelope. Inserting the expression for the propagation kernel  $\tilde{H}_{FP}(k_x, k_y, \bar{\omega}; z)$  from Eq. (A.6), the propagation of the slowly varying envelope in the spectral domain is given by

$$\psi(k_x, k_y, \bar{\omega}; z) = \psi_0(k_x, k_y, \bar{\omega}) \exp \left[ -i \frac{z}{2} \left( D_0 \bar{\omega}^2 - \frac{1}{k(\omega_0)} (k_x^2 + k_y^2) \right) \right]. \quad (\text{A.10})$$

By taking the derivative of both sides of Eq. (A.10) with respect to  $z$ , the wave equation for the propagation of the slowly varying envelope in the co-moving frame is then obtained as

$$i \frac{\partial \psi(k_x, k_y, \bar{\omega}; z)}{\partial z} = -\frac{1}{2} \left( D_0 \bar{\omega}^2 - \frac{1}{k(\omega_0)} (k_x^2 + k_y^2) \right) \psi(k_x, k_y, \bar{\omega}; z). \quad (\text{A.11})$$

Finally, performing the three dimensional IFT, the wave equation in position-time domain is given by

$$i \frac{\partial \psi(x, y, \bar{t}; z)}{\partial z} + \left( \frac{1}{2k(\omega_0)} \Delta^{(2)} - \frac{D_0}{2} \frac{\partial^2}{\partial \bar{t}^2} \right) \psi(x, y, \bar{t}; z) = 0. \quad (\text{A.12})$$

## Appendix B: Derivation of the generalized spatio-temporal Huygens integral

Here the derivation of the generalized spatio-temporal Huygens integral given in Eq. (2.3.19) which governs the propagation of a pulsed beam in the spatio-temporal domain is shown in detail. From the Kirchhoff integral equation, the pulsed beam field component with given frequency  $\omega$  at the output plane,  $\psi_2(\mathbf{r}_2, \omega)$ , is related to that at the input plane,  $\psi_1(\mathbf{r}_1, \omega)$ , by [1, 44]

$$\psi_2(\mathbf{r}_2, \omega) = \zeta' \iint \psi_1(\mathbf{r}_1, \omega) \exp\{i\Phi(\mathbf{r}_1, \mathbf{r}_2, \omega)\} d\mathbf{r}_1, \quad (\text{B.1})$$

where  $\zeta'$  is a constant,  $\mathbf{r}_1$  and  $\mathbf{r}_2$  are the transversal coordinate vectors in the input and output planes respectively and  $\Phi(\mathbf{r}_1, \mathbf{r}_2, \omega)$  is an eikonal between the input plane and output plane for the field component with frequency  $\omega$ . Taking the inverse temporal FT of Eq. (B.1) and replacing the  $\psi_1(\mathbf{r}_1, \omega)$  with the FT (using Eq. (2.1.3)) of its temporal field  $\psi_1(\mathbf{r}_2, t_1)$ , the output pulsed field in the temporal domain can be written as

$$\psi_2(\mathbf{r}_2, t_2) = \zeta \iiint \psi_1(\mathbf{r}_1, t_1) \exp\{i\Phi(\mathbf{r}_1, \mathbf{r}_2, t_1, t_2)\} d\mathbf{r}_1 dt_1, \quad (\text{B.2})$$

where  $\zeta \exp\{i\Phi(\mathbf{r}_1, \mathbf{r}_2, t_1, t_2)\} = \frac{\zeta'}{2\pi} \int \exp\{i\Phi(\mathbf{r}_1, \mathbf{r}_2, \omega)\} \exp\{i\omega(t_2 - t_1)\} d\omega$ , with  $\Phi(\mathbf{r}_1, \mathbf{r}_2, t_1, t_2)$  being the spatio-temporal eikonal function for the pulsed beam. In the paraxial approximation, the spatial eikonal function for paraxial beam propagation is obtained from the spatial or lateral phase delay which is given by [1, 3, 81]

$$\begin{aligned} \Phi_r &= -\frac{k_0}{2} [n_2 (x_2\theta_{x2} + y_2\theta_{y2}) - [n_1 (x_1\theta_{x1} + y_1\theta_{y1})]] \\ &= -\frac{k_0}{2} (n_2 \boldsymbol{\theta}_2^T \mathbf{r}_2 - n_1 \boldsymbol{\theta}_1^T \mathbf{r}_1), \end{aligned} \quad (\text{B.3})$$

where  $k_0$  is the propagation constant of the reference ray at central frequency  $\omega_0$ . Analogously, the temporal (longitudinal) eikonal can be obtained from the longitudinal phase delay which is given by

$$\Phi_t = \Delta\phi_2 - \Delta\phi_1, \quad (\text{B.4})$$



where  $\Delta\phi_1$  and  $\Delta\phi_2$  are the temporal phase differences between the reference ray with the central frequency  $\omega_0$  and that with slightly shifted frequency  $\omega_c$  in the input and output planes respectively. For a linear chirped pulse, the instantaneous frequency  $\omega_c$  is a linear function of the time  $t$ ,

$$\omega_c - \omega_0 = S(t - t_0), \quad (\text{B.5})$$

where  $S$  is the frequency sweep rate and  $t_0$  is the arrival time of the reference ray with frequency  $\omega_0$ . Hence, the temporal phase differences are given by

$$\begin{aligned} \Delta\phi_1 &= \int (\omega_{c1} - \omega_0) d(t_1 - t_0) = \frac{1}{2} S (t_1 - t_0)^2 = \frac{1}{2} \bar{\omega}_1 \bar{t}_1, \\ \Delta\phi_2 &= \int (\omega_{c2} - \omega_0) d(t_2 - t_0) = \frac{1}{2} S (t_2 - t_0)^2 = \frac{1}{2} \bar{\omega}_2 \bar{t}_2. \end{aligned} \quad (\text{B.6})$$

with  $\bar{\omega}_1 = (\omega_{c1} - \omega_0)$ ,  $\bar{\omega}_2 = (\omega_{c2} - \omega_0)$ ,  $\bar{t}_1 = (t_1 - t_0)$  and  $\bar{t}_2 = (t_2 - t_0)$ . Inserting Eq. (B.6) into Eq. (B.6), and using the equation  $\omega_0 = ck_0$ , the longitudinal phase delay becomes

$$\Phi_t = \frac{k_0}{2} \left( \frac{\bar{\omega}_2}{\omega_0} c \bar{t}_2 - \frac{\bar{\omega}_1}{\omega_0} c \bar{t}_1 \right). \quad (\text{B.7})$$

The whole phase delay corresponding to the spatio-temporal eikonal function is computed by adding the spatial (lateral) and the temporal (longitudinal) phase delays given in Eq. (B.3) and Eq. (B.7) respectively as

$$\Phi(\mathbf{r}_1, \mathbf{r}_2, t_1, t_2) = \Phi_r + \Phi_t = -\frac{k_0}{2} \left( n_2 \boldsymbol{\theta}_2^T \mathbf{r}_2 - n_1 \boldsymbol{\theta}_1^T \mathbf{r}_1 - \frac{\bar{f}_2}{f_0} c \bar{t}_2 + \frac{\bar{f}_1}{f_0} c \bar{t}_1 \right), \quad (\text{B.8})$$

where the ratio of herzian frequencies  $\frac{\bar{f}_1}{f_0}$  and  $\frac{\bar{f}_2}{f_0}$  are used which are equivalent to the ratios of the corresponding angular frequencies. Inserting Eq. (B.8) into Eq. (B.2), the generalized spatio-temporal Huygens integral in paraxial approximation in optical system with linear chirp becomes

$$\psi_2(\mathbf{r}_2, t_2) = \zeta \iiint \psi_1(\mathbf{r}_1, t_1) \exp \left[ -i \frac{k_0}{2} \left( n_2 \boldsymbol{\theta}_2^T \mathbf{r}_2 - n_1 \boldsymbol{\theta}_1^T \mathbf{r}_1 - \frac{\bar{f}_2}{f_0} c \bar{t}_2 + \frac{\bar{f}_1}{f_0} c \bar{t}_1 \right) \right] d\mathbf{r}_1 dt_1. \quad (\text{B.9})$$

## Appendix C: Propagation equations for full Gaussian (pulsed) beam

In this Appendix the detailed derivation of the propagation equations for the monochromatic GB and the GPB through a paraxial optical system using the matrix method is given. Although the derivations of these equations can also be found in the literature [44, 49], they are given here as they serve as the basis for the further derivations developed in this work for truncated Gaussian (pulsed) beams which will be presented in Appendix A.5.

### C.1 Derivation of propagation formula for a monochromatic Gaussian beam

The analytical propagation equation, given in Eq. (2.3.29), for a monochromatic GB is derived by solving the Collins integral with a GB input field. Substituting the general astigmatic monochromatic GB in Eq. (2.3.4) into the general Collins integral in Eq. (2.3.28) and performing simple algebraic manipulations the reduced field of the propagated GB becomes

$$\psi_2(\mathbf{r}_2) = \frac{i}{\lambda|\mathbf{B}|^{1/2}} \iint \exp \left[ -\frac{ik_0}{2} (\mathbf{r}_1^T \mathbf{P} \mathbf{r}_1 - 2\mathbf{r}_1^T \mathbf{B}^{-1} \mathbf{r}_2 + \mathbf{r}_2^T \mathbf{D} \mathbf{B}^{-1} \mathbf{r}_2) \right] d\mathbf{r}_1, \quad (\text{C.1.1})$$

where  $\mathbf{P} = \mathbf{Q}_1^{-1} + \mathbf{B}^{-1} \mathbf{A}$ . The expression inside the exponential function in Eq. (C.1.1) can be written as

$$\begin{aligned} & \mathbf{r}_1^T \mathbf{P} \mathbf{r}_1 - 2\mathbf{r}_1^T \mathbf{B}^{-1} \mathbf{r}_2 + \mathbf{r}_2^T \mathbf{D} \mathbf{B}^{-1} \mathbf{r}_2 \\ &= \left| \mathbf{P}^{1/2} \mathbf{r}_1 - \mathbf{P}^{-1/2} \mathbf{B}^{-1} \mathbf{r}_2 \right|^2 + \mathbf{r}_2^T (\mathbf{D} \mathbf{B}^{-1} - \mathbf{B}^{-1T} \mathbf{P}^{-1} \mathbf{B}^{-1}) \mathbf{r}_2 \end{aligned} \quad (\text{C.1.2})$$

Using the properties of the paraxial system matrices [49],  $-\mathbf{B}^{-1T} = \mathbf{C} - \mathbf{D} \mathbf{B}^{-1} \mathbf{A}$ , the second term of Eq. (C.1.2) is simplified by

$$\begin{aligned} \mathbf{D} \mathbf{B}^{-1} - \mathbf{B}^{-1T} \mathbf{P}^{-1} \mathbf{B}^{-1} &= (\mathbf{C} + \mathbf{D} \mathbf{Q}_1^{-1}) (\mathbf{A} + \mathbf{B} \mathbf{Q}_1^{-1})^{-1} \\ &= \mathbf{Q}_2^{-1} \end{aligned} \quad (\text{C.1.3})$$

Substituting Eq. (C.1.3) into Eq. (C.1.2) and then back into Eq. (C.1.1) and taking out terms which are independent of  $\mathbf{r}_1$  to the right side of the double integral, the reduced field of output GB becomes

$$\psi_2(\mathbf{r}_2) = \frac{i}{\lambda|\mathbf{B}|^{1/2}} \exp \left[ -\frac{ik_0}{2} (\mathbf{r}_2^T \mathbf{Q}_2^{-1} \mathbf{r}_2) \right] \iint \exp \left[ -\frac{ik_0}{2} (|\mathbf{P}^{1/2} \mathbf{r}_1 - \mathbf{P}^{-1/2} \mathbf{B}^{-1} \mathbf{r}_2|^2) \right] d\mathbf{r}_1. \quad (\text{C.1.4})$$

To simplify the remaining double integral in Eq.(C.1.4), an auxiliary vector  $\mathbf{\Gamma} = \mathbf{P}^{1/2} \mathbf{r}_1 - \mathbf{P}^{-1/2} \mathbf{B}^{-1} \mathbf{r}_2$  is introduced as the integration variable. Using the following vectorial integration formula

$$\begin{aligned} \iint \exp[-a\mathbf{r}^2] d\mathbf{r} &= \int_{-\infty}^{\infty} \int_{-\infty}^{\infty} \exp -a(x^2 + y^2) dx dy \\ &= \frac{\pi}{a}, \end{aligned} \quad (\text{C.1.5})$$

and performing the algebraic manipulation, Eq. (C.1.4) is finally simplified to

$$\psi_2(\mathbf{r}_2) = \frac{\psi_0}{\sqrt{|\mathbf{A} + \mathbf{B}\mathbf{Q}_1^{-1}|}} \exp \left( -\frac{ik_0}{2} \mathbf{r}_2^T \mathbf{Q}_2^{-1} \mathbf{r}_2 \right), \quad (\text{C.1.6})$$

which is the well known equation for the propagation of an astigmatic GB through a paraxial optical system [48, 49, 105].

## C.2 Derivation of the propagation formula of a Gaussian pulsed beam

The analytical propagation equation, given in Eq. (2.3.27), for a GPB is derived by solving the generalized spatio-temporal Huygen's integral with a GPB input pulse field. The derivation procedure is completely analogous with that of the monochromatic GB discussed in Appendix C.1. Here the important differences in the derivation are simply highlighted. The main difference is that for GPB case, the  $3 \times 1$  spatio-temporal coordinate vectors, ( $\tilde{\mathbf{r}}_1$  and  $\tilde{\mathbf{r}}_2$ ) are used instead of their spatial counterparts  $\mathbf{r}_1$  and  $\mathbf{r}_2$ , which are  $2 \times 1$ . Similarly, the  $3 \times 3$  spatio-temporal sub-matrices ( $\tilde{\mathbf{A}}, \tilde{\mathbf{B}}, \tilde{\mathbf{C}}$  and  $\tilde{\mathbf{D}}$ ), of the  $6 \times 6$  Lin matrix are used instead of the  $2 \times 2$  sub-matrices ( $\mathbf{A}, \mathbf{B}, \mathbf{C}$  and  $\mathbf{D}$ ), of the  $4 \times 4$  spatial ABCD matrix.

The derivation is started by substituting the Gaussian pulsed beam in Eq. (2.3.10) as

an input field to the spatio-temporal Huygens integral in Eq. (2.3.24). Performing algebraic manipulations similar to that discussed in Appendix C.1 and using triple vectorial integral identity

$$\iiint \exp[-a\tilde{\mathbf{r}}^2] d\tilde{\mathbf{r}} = \left(\frac{\pi}{a}\right)^{3/2}, \quad (\text{C.2.1})$$

finally the complex envelope of the propagated GPB is obtained to be

$$\psi_2(\tilde{\mathbf{r}}_2) = \frac{\psi_0}{\sqrt{|\tilde{\mathbf{A}} + \tilde{\mathbf{B}}\tilde{\mathbf{Q}}_1^{-1}|}} \exp\left(-\frac{ik_0}{2}\tilde{\mathbf{r}}_2^T \tilde{\mathbf{Q}}_2^{-1} \tilde{\mathbf{r}}_2\right), \quad (\text{C.2.2})$$

where  $\tilde{\mathbf{Q}}_2^{-1} = (\tilde{\mathbf{C}} + \tilde{\mathbf{D}}\tilde{\mathbf{Q}}_1^{-1})(\tilde{\mathbf{A}} + \tilde{\mathbf{B}}\tilde{\mathbf{Q}}_1^{-1})^{-1}$  is the  $3 \times 3$  complex spatio-temporal curvature matrix of the final GPB.

## Appendix D: Propagation equations for the truncated Gaussian (pulsed) beam

In this section the detailed derivation of the analytical formulae for the propagation of truncated GB and spatially truncated GPB is presented. The derivations are the original contributions of this work and have also been published in peer reviewed journals [64, 65].

### D.1 Derivation of the propagation formula of a truncated Gaussian beam

To derive propagation formula for generally non-symmetric truncated GB, the truncated GB in Eq. (3.3.1) is first inserted into the Collins integral in Eq. (2.3.28). This gives an expression similar to Eq. (C.1.1) but with the integration limit in the x-changed from  $[-\infty, \infty]$  to  $[c_x, \infty]$ . The resulting vector integral written in terms of x- and y becomes

$$\psi_{2,t}(\mathbf{r}_2) = \frac{i}{\lambda|\mathbf{B}|^{1/2}} \int_{c_x}^{\infty} \int_{-\infty}^{\infty} \exp \left[ -\frac{ik_0}{2} (\mathbf{r}_1^T \mathbf{P} \mathbf{r}_1 - 2\mathbf{r}_1^T \mathbf{B}^{-1} \mathbf{r}_2 + \mathbf{r}_2^T \mathbf{D} \mathbf{B}^{-1} \mathbf{r}_2) \right] dy_1 dx_1, \quad (\text{D.1.1})$$

where  $\mathbf{P} = \mathbf{Q}_1^{-1} + \mathbf{B}^{-1} \mathbf{A}$ ,  $\mathbf{r}_1 = [x_1, y_1]^T$ ,  $\mathbf{r}_2 = [x_2, y_2]^T$ ,  $\mathbf{Q}_1^{-1}$  is the  $2 \times 2$  complex curvature matrix of the input GB and  $\mathbf{A}, \mathbf{B}, \mathbf{C}, \mathbf{D}$  are the  $2 \times 2$  submatrices of the paraxial system matrix.

By taking the constant terms out of the double integrals and expanding the vectors inside the exponential function, Eq. (D.1.1) can be written as

$$\psi_{2,t}(\mathbf{r}_2) = G \int_{c_x}^{\infty} \int_{-\infty}^{\infty} \exp [g_{yy}y_1^2 + g_{xy}x_1y_1 + g_{xx}x_1^2 + g_x x_1 + g_y y_1] dy_1 dx_1, \quad (\text{D.1.2})$$

where

$$G = \frac{i}{\lambda|\mathbf{B}|^{1/2}} \exp \left( -\frac{ik_0}{2} \mathbf{r}_2^T \mathbf{D} \mathbf{B}^{-1} \mathbf{r}_2 \right), \quad g_{xx} = -\frac{ik_0}{2} P_{xx}, \quad g_{yy} = -\frac{ik_0}{2} P_{yy}, \\ g_{xy} = -\frac{ik_0}{2} (P_{xy} + P_{yx}), \quad g_x = ik_0 (B_{xx}^{-1} x_2 + B_{xy}^{-1} y_2), \quad g_y = ik_0 (B_{yx}^{-1} x_2 + B_{yy}^{-1} y_2) \quad (\text{D.1.3})$$

To systematically solve the double integral in Eq. (D.1.2), it is rewritten as

$$\psi_{2,t}(\mathbf{r}_2) = G \int_{c_x}^{\infty} \int_{-\infty}^{\infty} \exp [g_{yy}(y_1 + hx_1)^2 + g_y y_1 + (g_{xx} - h^2 g_{yy})x_1^2 + g_x x_1] dy_1 dx_1, \quad (\text{D.1.4})$$

where  $h = \frac{g_{xy}}{2g_{yy}}$  is chosen so that the term  $x_1 y_1$  is included in the  $(y_1 + hx_1)^2$  expression. Moving all terms independent of  $y_1$  to the left side of the inner integral, Eq. (D.1.4) becomes

$$\psi_{2,t}(\mathbf{r}_2) = G \int_{c_x}^{\infty} \left\{ \exp [(g_{xx} - h^2 g_{yy})x_1^2 + g_x x_1] \int_{-\infty}^{\infty} \exp [g_{yy}(y_1 + hx_1)^2 + g_y y_1] dy_1 \right\} dx_1, \quad (\text{D.1.5})$$

By substituting  $u = y_1 + hx_1$  for the inner integral of Eq. (D.1.5), it can be shown that

$$\int_{-\infty}^{\infty} \exp [g_{yy}(y_1 + hx_1)^2 + g_y y_1] dy_1 = \exp [-g_y hx_1] \int_{-\infty}^{\infty} \exp [g_{yy}y_1^2 + g_y y_1] dy_1, \quad (\text{D.1.6})$$

Substituting Eq. (D.1.6) into Eq. (D.1.5), it can be written as a product of two separate integrals as

$$\begin{aligned} \psi_{2,t}(\mathbf{r}_2) = & G \int_{c_x}^{\infty} \exp [(g_{xx} - h^2 g_{yy})x_1^2 + (g_x - hg_y)x_1] dx_1 \\ & \times \int_{-\infty}^{\infty} \exp [g_{yy}(y_1 + hx_1)^2 + g_y y_1] dy_1, \end{aligned} \quad (\text{D.1.7})$$

Using the following integration formula

$$\begin{aligned} \int_c^{\infty} \exp (-ax^2 - 2bx) dx &= \frac{1}{2} \sqrt{\frac{\pi}{a}} \exp \left( \frac{b^2}{a} \right) \operatorname{erfc} \left( \frac{b + ac}{\sqrt{a}} \right) \\ &= \frac{1}{2} \operatorname{erfc} \left( \frac{b + ac}{\sqrt{a}} \right) \int_{-\infty}^{\infty} \exp (-ax^2 - 2bx) dx, \end{aligned} \quad (\text{D.1.8})$$

Eq. (D.1.7) can be written as

$$\begin{aligned} \psi_{2,t}(\mathbf{r}_2) &= \frac{1}{2} \operatorname{erfc} \left( \frac{b_x + a_x c_x}{\sqrt{a}} \right) G \int_{-\infty}^{\infty} \exp [(g_{xx} - h^2 g_{yy})x_1^2 + (g_x - hg_y)x_1] dx_1 \\ &\quad \times \int_{-\infty}^{\infty} \exp [g_{yy}(y_1 + hx_1)^2 + g_y y_1] dy_1, \end{aligned} \quad (\text{D.1.9})$$

where

$$a_x = -(g_{xx} - h^2 g_{yy}), \quad b_x = -\frac{1}{2}(g_x - h g_y). \quad (\text{D.1.10})$$

The last two expressions in Eq. (D.1.9) are equivalent to the expression the propagation of a full GB given in Eq. (C.1.6). Hence, the propagation of the truncated GB is written as

$$\psi_{2,t}(\mathbf{r}_2) = \frac{1}{2} \operatorname{erfc} \left( \frac{b_x + a_x c_x}{\sqrt{a_x}} \right) \psi_2(\mathbf{r}_2), \quad (\text{D.1.11})$$

where  $\psi_2(\mathbf{r}_2)$  is the reduced field of the full GB after the propagation.

For the special case of a symmetrical truncated half GB ( $c_x = 0$ ) propagation through an orthogonal optical system with the final coordinate system rotated so that the matrix  $\mathbf{P} = \mathbf{Q}_1^{-1} + \mathbf{B}^{-1}\mathbf{A}$  becomes pure diagonal, the parameters of the erfc function become

$$a_x = \frac{ik_0}{2} (Q_{xx}^{-1} + B_{xx}^{-1} A_{xx}), \quad b_x = -\frac{ik_0}{2} B_{xx}^{-1} x_2, \quad c_x = 0, \quad (\text{D.1.12})$$

and hence Eq. (D.1.11) simplifies to

$$E_{2,h}(\mathbf{r}_2) = \frac{1}{2} \operatorname{erfc} \left( -\sqrt{\frac{ik_0}{2B_{xx}(A_{xx} + B_{xx}Q_{1,xx}^{-1})}} x_2 \right) E_2(\mathbf{r}_2). \quad (\text{D.1.13})$$

For such special case, it is possible to derive the propagation equation for a truncated GB, shown in Fig. D.1, where the GB is truncated along both x- and y-axis. In such case the integration limits of both  $x$  and  $y$  in Eq. (D.1.1) are changed to  $[c_x, \infty]$  and  $[c_y, \infty]$  respectively. Since it has been assumed that  $\mathbf{P}$  is a diagonal matrix, in this case,  $P_{xy} = P_{yx} = 0$  and the expression in Eq. D.1.2 simplifies to

$$E_{2,q}(\mathbf{r}_2) = G \int_{c_x}^{\infty} \int_{c_y}^{\infty} \exp [g_{yy}y_1^2 + g_{xx}x_1^2 + g_x x_1 + g_y y_1] dy_1 dx_1, \quad (\text{D.1.14})$$

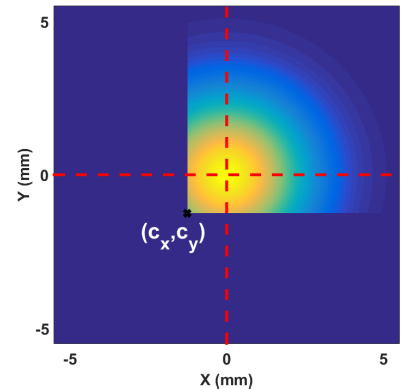


Figure D.1: A GB truncated in both x- and y- dimensions.

where  $G, g_x, g_y, g_{xx}$  and  $g_{yy}$  are as given in Eq. D.1.3.

Separating the integration variables in Eq. D.1.14 and using integration formulas given in Eq. D.1.8, the propagation of quarter GB through an orthogonal optical system becomes

$$E_{2,q}(\mathbf{r}_2) = \frac{1}{4} \operatorname{erfc} \left( \frac{b_x + a_x c_x}{\sqrt{a_x}} \right) \operatorname{erfc} \left( \frac{b_y + a_y c_y}{\sqrt{a_y}} \right) E_2(\mathbf{r}_2), \quad (\text{D.1.15})$$

where  $a_x, b_x, a_y$  and  $b_y$  are given by expressions in Eq. D.1.12 for the corresponding components. For special case of simple quarter GB with  $c_x = c_y = 0$ , the propagation equation in Eq. D.1.15 simplifies to

$$E_{2,q}(\mathbf{r}_2) = \frac{1}{4} \operatorname{erfc} \left( -\sqrt{\frac{ik_0}{2B_{xx}(A_{xx} + B_{xx}Q_{1,xx}^{-1})}} x_2 \right) \operatorname{erfc} \left( -\sqrt{\frac{ik_0}{2B_{yy}(A_{yy} + B_{yy}Q_{1,yy}^{-1})}} y_2 \right) E_2(\mathbf{r}_2). \quad (\text{D.1.16})$$

## D.2 Derivation of the propagation formula of a spatially truncated Gaussian pulsed beam

To derive the propagation formula for a spatially truncated GPB, the complex amplitude of the spatially truncated GPB in Eq. (3.3.5) is first inserted into the generalized spatio-temporal Huygens diffraction integral given in Eq. (2.3.19). Due to the Heaviside function in Eq. (3.3.5), the integration limits for the x-axis is changed from  $[-\infty, \infty]$  to  $[c_x, \infty]$  and the resulting diffraction integral becomes

$$U_{2,t}(\tilde{\mathbf{r}}_2) = \left( \frac{i}{\lambda_0} \right)^{3/2} \frac{1}{\sqrt{\det(\tilde{\mathbf{B}})}} \int_{c_x}^{\infty} \int_{-\infty}^{\infty} \int_{-\infty}^{\infty} dx_1 dy_1 d\tau_1 \exp \left[ -\frac{ik_0}{2} \left( \tilde{\mathbf{r}}_1^T \tilde{\mathbf{P}} \tilde{\mathbf{r}}_1 - 2\tilde{\mathbf{r}}_1^T \tilde{\mathbf{B}}^{-1} \tilde{\mathbf{r}}_2 + \tilde{\mathbf{r}}_2^T \tilde{\mathbf{D}} \tilde{\mathbf{B}}^{-1} \tilde{\mathbf{r}}_2 \right) \right], \quad (\text{D.2.1})$$

where  $\tilde{\mathbf{P}} = \tilde{\mathbf{Q}}_1^1 + \tilde{\mathbf{B}}^{-1} \tilde{\mathbf{A}}$ .

Due to the different integration limit, the x-components are treated differently than the  $y$  and  $\tau$  components in the integral. In order to facilitate the following derivation, the  $3 \times 1$  vectors ( $\tilde{\mathbf{r}}_1$  and  $\tilde{\mathbf{r}}_2$ ) and the  $3 \times 3$  matrices are separated into the  $x$  and  $y - \tau$  or  $\mathbf{w}$  components using expressions similar to that given in Eq. (3.3.6) and (3.3.7).



Taking the constant terms out of the integrals and expanding the vectors inside the exponential function in Eq. (D.2.1) into  $x$  and  $\mathbf{w}$  components the diffraction integral becomes

$$U_{2,t}(\tilde{\mathbf{r}}_2) = G \int_{c_x}^{\infty} \int_{-\infty}^{\infty} \exp \left[ \mathbf{g}_{\mathbf{w}\mathbf{w}} \mathbf{w}_1^2 + \mathbf{g}_{x\mathbf{w}} x_1 \mathbf{w}_1 + g_{xx} x_1^2 + g_x x_1 + \mathbf{g}_w^T \mathbf{w}_1 \right] d\mathbf{w}_1 dx_1, \quad (\text{D.2.2})$$

where

$$G = \left( \frac{i}{\lambda_0} \right)^{3/2} \frac{1}{\sqrt{\det(\tilde{\mathbf{B}})}} \exp \left( -\frac{ik_0}{2} \tilde{\mathbf{r}}_2^T \tilde{\mathbf{D}} \tilde{\mathbf{B}}^{-1} \tilde{\mathbf{r}}_2 \right), \quad (\text{D.2.3})$$

$$g_{xx} = -\frac{ik_0}{2} \tilde{\mathbf{P}}_{xx}, \quad \mathbf{g}_{\mathbf{w}\mathbf{w}} = -\frac{ik_0}{2} \tilde{\mathbf{P}}_{\mathbf{w}\mathbf{w}}, \quad \mathbf{g}_{x\mathbf{w}} = -\frac{ik_0}{2} (\tilde{\mathbf{P}}_{x\mathbf{w}} + \tilde{\mathbf{P}}_{\mathbf{w}x}),$$

$$g_x = ik_0 (\tilde{\mathbf{B}}_{xx}^{-1} x_2 + \tilde{\mathbf{B}}_{x\mathbf{w}}^{-1} \mathbf{w}_2), \quad \mathbf{g}_w = ik_0 (\tilde{\mathbf{B}}_{\mathbf{w}x}^{-1} x_2 + \tilde{\mathbf{B}}_{\mathbf{w}\mathbf{w}}^{-1} \mathbf{w}_2).$$

In order to systematically solve the integrals in Eq. (D.2.2), it is rewritten as

$$U_{2,t}(\tilde{\mathbf{r}}_2) = G \int_{c_x}^{\infty} \int_{-\infty}^{\infty} \exp \left[ (\mathbf{w}_1 + \mathbf{h}x_1)^T \mathbf{g}_{\mathbf{w}\mathbf{w}} (\mathbf{w}_1 + \mathbf{h}x_1) + \mathbf{g}_w^T \mathbf{w}_1 + (g_{xx} - \mathbf{h}^T \mathbf{g}_{\mathbf{w}\mathbf{w}} \mathbf{h}) x_1^2 + g_x x_1 \right] d\mathbf{w}_1 dx_1, \quad (\text{D.2.4})$$

where  $\mathbf{h} = \mathbf{g}_{x\mathbf{w}} (\mathbf{g}_{\mathbf{w}\mathbf{w}} + \mathbf{g}_{\mathbf{w}\mathbf{w}}^T)^{-1}$  is  $2 \times 1$  complex vector. The value of  $\mathbf{h}$  is chosen to make sure that the  $\mathbf{g}_{x\mathbf{w}} x_1 \mathbf{w}_1$  term is included in the matrix product  $(\mathbf{w}_1 + \mathbf{h}x_1)^T \mathbf{g}_{\mathbf{w}\mathbf{w}} (\mathbf{w}_1 + \mathbf{h}x_1)$  in Eq. (D.2.4).

Moving all terms independent of  $\mathbf{w}_1$  to the left side of the inner integral, Eq. (D.2.4) becomes

$$U_{2,t}(\tilde{\mathbf{r}}_2) = G \int_{c_x}^{\infty} \left\{ \exp \left[ (g_{xx} - \mathbf{h}^T \mathbf{g}_{\mathbf{w}\mathbf{w}} \mathbf{h}) x_1^2 + g_x x_1 \right] \int_{-\infty}^{\infty} \exp \left[ (\mathbf{w}_1 + \mathbf{h}x_1)^T \mathbf{g}_{\mathbf{w}\mathbf{w}} (\mathbf{w}_1 + \mathbf{h}x_1) + \mathbf{g}_w^T \mathbf{w}_1 \right] d\mathbf{w}_1 \right\} dx_1, \quad (\text{D.2.5})$$

Substituting  $\mathbf{u} = \mathbf{w}_1 + \mathbf{h}x_1$  for the inner integral of Eq. (D.2.5), and performing straight forward vector integration, it can be seen that

$$\int_{-\infty}^{\infty} \exp \left[ (\mathbf{w}_1 + \mathbf{h}x_1)^T \mathbf{g}_{\mathbf{w}\mathbf{w}} (\mathbf{w}_1 + \mathbf{h}x_1) + \mathbf{g}_w^T \mathbf{w}_1 \right] d\mathbf{w}_1$$

$$= \exp \left[ -\mathbf{g}_w^T \mathbf{h}x_1 \right] \int_{-\infty}^{\infty} \exp \left[ \mathbf{w}_1^T \mathbf{g}_{\mathbf{w}\mathbf{w}} \mathbf{w}_1 + \mathbf{g}_w^T \mathbf{w}_1 \right] d\mathbf{w}_1, \quad (\text{D.2.6})$$

Inserting Eq. (D.2.6) back into Eq. (D.2.5), the expression inside the double integral can be separated into  $x$  and  $\mathbf{w}$  dependant terms as

$$U_{2,t}(\tilde{\mathbf{r}}_2) = G \int_{c_x}^{\infty} \exp \left[ (g_{xx} - \mathbf{h}^T \mathbf{g}_{\mathbf{w}\mathbf{w}} \mathbf{h}) x_1^2 + (g_x - \mathbf{g}_{\mathbf{w}}^T \mathbf{h}) x_1 \right] dx_1 \quad (\text{D.2.7})$$

$$\times \int_{-\infty}^{\infty} \exp \left[ \mathbf{w}_1^T \mathbf{g}_{\mathbf{w}\mathbf{w}} \mathbf{w}_1 + \mathbf{g}_{\mathbf{w}}^T \mathbf{w}_1 \right] d\mathbf{w}_1,$$

Using the following integration formula [106]

$$\int_c^{\infty} \exp(-ax^2 - 2bx) dx = \frac{1}{2} \operatorname{erfc} \left( \frac{b+ac}{\sqrt{a}} \right) \int_{-\infty}^{\infty} \exp(-ax^2 - 2bx) dx, \quad (\text{D.2.8})$$

Eq. (D.2.7) is rewritten in terms of integrals with the same integration limits of  $[-\infty, \infty]$  as

$$U_{2,t}(\tilde{\mathbf{r}}_2) = \frac{1}{2} \operatorname{erfc} \left( \frac{b_x + a_x c_x}{\sqrt{a_x}} \right) \int_{-\infty}^{\infty} \exp \left[ \mathbf{w}_1^T \mathbf{g}_{\mathbf{w}\mathbf{w}} \mathbf{w}_1 + \mathbf{g}_{\mathbf{w}}^T \mathbf{w}_1 \right] d\mathbf{w}_1 \quad (\text{D.2.9})$$

$$\times G \int_{-\infty}^{\infty} \exp \left[ (g_{xx} - \mathbf{h}^T \mathbf{g}_{\mathbf{w}\mathbf{w}} \mathbf{h}) x_1^2 + (g_x - \mathbf{g}_{\mathbf{w}}^T \mathbf{h}) x_1 \right] dx_1,$$

where  $a_x = -(g_{xx} - \mathbf{h}^T \mathbf{g}_{\mathbf{w}\mathbf{w}} \mathbf{h})$  and  $b_x = -\frac{1}{2} (g_x - \mathbf{g}_{\mathbf{w}}^T \mathbf{h})$ .

Going backward with the new integration limit, it can be easily seen that the last two terms in Eq. (D.2.9) are equivalent to the propagation of the full GPB. Hence, the electric field of spatially truncated GPB after propagation is given by

$$U_{2,t}(\tilde{\mathbf{r}}_2) = \frac{1}{2} \operatorname{erfc} \left( \frac{b_x + a_x c_x}{\sqrt{a_x}} \right) U_{2,f}(\tilde{\mathbf{r}}_2), \quad (\text{D.2.10})$$

where  $U_{2,f}(\tilde{\mathbf{r}}_2)$  is the reduced complex amplitude of the full GPB after propagation. For the special case of propagating of a symmetrically truncated ( $c_x = 0$ ) orthogonal GPB (purely diagonal  $\tilde{\mathbf{Q}}_1^{-1}$ ) through a homogeneous medium, Eq. (D.2.10) simplifies to

$$U_{2,t}(\tilde{\mathbf{r}}_2) = \frac{1}{2} \operatorname{erfc} \left( -\sqrt{\frac{ik_0}{2(\tilde{\mathbf{Q}}_{1,xx}^{-1} + \tilde{\mathbf{B}}_{xx}^{-1})}} \tilde{\mathbf{B}}_{xx}^{-1} x_2 \right) U_{2,f}(\tilde{\mathbf{r}}_2), \quad (\text{D.2.11})$$

where  $\tilde{\mathbf{Q}}_{1,xx}^{-1}$  is the complex curvature of the initial GPB in the x-direction,  $\tilde{\mathbf{B}}_{xx}^{-1} = n/L$ ,  $n$  is the refractive index of the medium and  $L$  is the propagation distance.

## Appendix E: Sampling schemes for the Gaussian beam centers

The centers of GBs which are used to decompose a given field are distributed in the input transversal plane using a given sampling scheme. Among a lot of different sampling schemes found in the literature [107,108], the three schemes shown in Fig. E.1 are used for the GBD method described in this work. The cartesian sampling, shown in Fig.

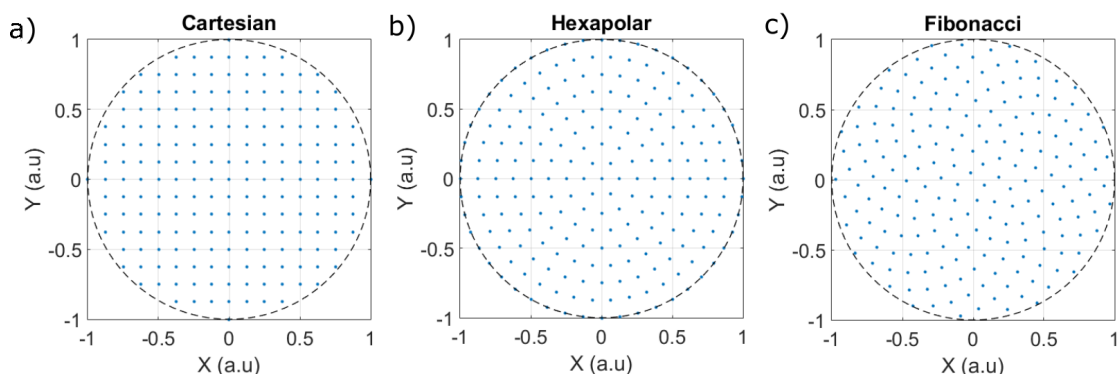


Figure E.1: The dot diagram of 200 sampling points inside a unit circle distributed using a) the cartesian, b) the hexapolar, and c) the Fibonacci sampling scheme.

E.1a, is the simplest distribution which is generated by taking a 2-D grid coordinates formed from uniformly sampled points along the x- and the y-axis. However, for field with circular-shaped amplitude profiles, the cartesian sampling usually results in large residual error, especially near the boundary. In such cases, the hexapolar sampling scheme, shown in Fig. E.1b, gives better decomposition result. The hexapolar grid is generated by taking the center point together with additional points distributed in several rings around the center. In the first ring, 6 points which are uniformly distributed in azimuthal direction are taken and for each subsequent rings the number of sampling points taken increases by 6. As the hexapolar sampling is more suitable for amplitude profiles with rotational symmetry, for the case of a general amplitude profile shape the Fibonacci sampling scheme, shown in Fig. E.1c, is used. For a total of  $N$  points distributed within a unit circle in a Fibonacci spiral pattern, the polar coordinates of each point is obtained by using [108]:

$$\theta_k = \frac{4\pi}{1 + \sqrt{5}}k \text{ and } r_k = \sqrt{\frac{k}{N}}, \quad (\text{E.0.1})$$

where  $k = 1, 2, 3, \dots$  is the index of the sampling point.

# List of Figures

2.1	a) The amplitude envelope, the oscillating real field, and the phase profile of a Gaussian pulse with quadratic phase. b) The corresponding intensity profile. . . . .	8
2.2	Demonstration of angular dispersion, spatial chirp and pulse front tilts of a pulse propagating through prism pair followed by dispersive medium.	11
2.3	Schematic diagram showing the ray pulse parameters of a given optical system. . . . .	17
2.4	The schematic diagram showing the hybrid diffraction model . . . . .	23
2.5	The schematic diagram showing the GBD method . . . . .	25
2.6	The effect of the overlap factor on a) the peak-valley error of the ripple on the top-hat amplitude profile oscillation, b) the number of GB required to fill the same window. The amplitudes of each GB together with the total superposed amplitude are shown for c) $\varepsilon_{OF} = 1.0$ and d) $\varepsilon_{OF} = 1.67$ . The width of individual GB is kept constant. . . . .	26
2.7	The local coordinate systems for the ray reflected and refracted from a plane interface. . . . .	30
2.8	The geometry of a high NA focusing. . . . .	31
3.1	a) The footprint of overlapping GBs projected on the transversal X-Y plane. b) The directions (shown in blue arrows) of all GBs used for decomposition of a given curved wavefront. c) The local surface patch of a single GB d) Sketch showing different parameters of the rays representing a single GB computed by the decomposition algorithm. Here only the YZ-cross section is shown for simplicity and the size of the GB is exaggerated. . . . .	34
3.2	a) Parabolic approximations of a spherical wavefront, with a radius of $4mm$ , by using the curvature at the center (in approx. 1) and by forcing the parabolic wavefront to coincide with the given one at a finite width $x = 3mm$ (in approx. 2). b) The residual error of the two approximations shown in (a). . . . .	35

3.3	The weighted RMS values of the residual wavefront error for the quadratic approximation of spherical wavefront with different radius of curvature $R$ using a single GB with different $1/e$ beam width $w_0$ . The logarithm value of the calculated result is shown in the plot. . . . .	36
3.4	The schematic diagram showing the spectral decomposition of an ultra-short pulse with an arbitrary spectral amplitude and phase profile into set of Gaussian pulses. . . . .	38
3.5	Schematic diagram of a ray reflected from a grating. . . . .	43
3.6	Schematic diagram showing the curved pulse front due to the spatio-temporal coupling in free space. . . . .	44
3.7	A simple 2D geometric construction for computation of the complex amplitude of the GPB on a given target pixel $P$ at a given flight time. .	46
3.8	Schematic sketch showing the spatial profile of a truncated GB with truncation parameter $c_x$ . . . . .	49
3.9	The amplitude profile of a symmetrical half GB shown in a) one and b) two-dimensional space. . . . .	50
3.10	a) Extraction of the sharp edges from rectangular amplitude profile in 1D using half GBs. b) The GBD result of the rectangular amplitude without sharp edge extraction. The residual amplitude error for GBD of c) the smooth central amplitude after sharp edge extraction, and d) the rectangular amplitude without sharp edge extraction. . . . .	51
3.11	a) A single half GB with shifted and rotated local axis. The footprint diagrams of a set of (b)10 non-astigmatic (c) 25 non-astigmatic and (d) 25 astigmatic half GBs used to represent a circular aperture. . . . .	52
4.1	(a-b) A single GB divided into two asymmetrical half GBs with sharp edges. (c-d) The amplitude profiles after the propagation of the half GBs shown in a and b respectively by a distance of $z = 0.1Z_R$ . . . . .	58
4.2	a) The cross-sectional amplitude of the propagated field in Fig. 4.1d together with that computed using the SPW method, b) The difference in the final amplitude propagated using the two methods. . . . .	58
4.3	The x-cross-sectional plots of the amplitude profiles of the subfields shown in Fig. 4.1 (a and b) respectively for different propagation distances.	59

- 
- 4.4 The comparison of the x-cross-section of the amplitude profile of the final propagated GB obtained as a coherent superposition of the two asymmetrical half GBs after propagation with the analytical result for propagation distances of a)  $z = 0.5Z_R$  and b)  $z = 3Z_R$ . . . . . 59
- 4.5 Sharp edge extraction using truncated GBs in 2D. a) The input uniform amplitude after the hard aperture, b) the footprint of the truncated GBs, c) the extracted sharp edge amplitude profile, and d) the remaining central amplitude profile with smooth edges. The red line plots over the amplitude profiles show the x-cross-sectional view. . . . . 60
- 4.6 The amplitude profiles of the a) outer sharp edge subfield b) the inner smooth subfield after propagating a distance of  $z = 10m$  in free space. . . . . 61
- 4.7 The amplitude profiles of the final propagated field using a) the modified GBD method b) the angular spectrum method. c) The y-cross-sectional view of the final propagated amplitude profiles. . . . . 61
- 4.8 The dependance of a) the residual amplitude error and b) the residual phase on the number of GBs and the beam overalp factor used for the decomposition. . . . . 62
- 4.9 The recomposed amplitudes and the corresponding residual amplitude and phase errors after the decomposition of spherical wavefront with radius of curvature  $R = 30mm$  after circular aperture with a semidiameter  $a = 18mm$  using three decomposition approaches. The results shown in (a)-(c) are obtained by using a set of GBs with zero initial curvatures; those shown in (d)-(f) are obtained by using a set of GBs with non-zero initial curvatures; and for the results shown in (g)-(i), truncated GBs are used to handle the sharp edge of the field after the hard aperture. . . . . 64
- 4.10 Point spread function comparison for a perfect lens with a circular clipping aperture (Airy pattern) . . . . . 65
- 4.11 a) The on-axis intensity of converging spherical wave with Fresnel number of  $N_F = 1$ . b) The relative focal shift of a converging spherical wave using focusing setups with different small Fresnel numbers. . . . . 66

4.12	a) The amplitude profile on the wavefront surface, and b) the wavefront profile of the input field. The cross sectional plots along the black dotted lines are shown using the red line with the values indicated in the right axis. c) The amplitude error and, d) the residual phase error after the GBD. . . . .	66
4.13	(a) The YZ-cross section of the intensity profile computed in the focal region of the converging wavefront with spherical aberration $c_9 = 100\lambda$ , (b) the geometric rays traced from the wavefront to the focal region. . .	67
4.14	The same as Fig. 4.12 but now for the case of the input field with a cone shaped wavefront. . . . .	68
4.15	The normalized intensity plots calculated by propagating the cone shaped wavefront with uniform ring illumination using the GBD method in free space : a) The YZ cross section, b) the axial profile for $x = y = 0$ and c) the transversal profile at $z = 8mm$ . . . . .	69
4.16	The vectorial field components at the focal plane computed by the polarized GBD method. . . . .	69
4.17	The vectorial field components at the focal plane computed by the vectorial Debye integral. . . . .	70
4.18	(a) The y- and (b) the x- cross-sectional plots of the total intensities shown in Fig. 4.16d and Fig. 4.17d in logarithmic scale. (c,d) The difference between the intensity values computed using the polarized GBD method and the vectorial Debye integral method for the corresponding cross-sections. . . . .	71
4.19	The spatio-temporal amplitude profiles of an ultrashort pulse propagating different distances in free space. . . . .	71
4.20	a) The same as in Fig. 4.19c but now computed using the conventional FT based method, b) The numerical difference between the amplitude profiles in (a) and in Fig. 4.19c. . . . .	72
4.21	The $x$ cross-section ( $y = 0$ ) spatio-temporal amplitude profile of spatially truncated GPB propagated by a distance of a) 0, b) $0.5Z_R$ and c) $4Z_R$ through fused silica with $Z_R = 39.27mm$ being the Rayleigh length computed using the central frequency. The vertical axis and color bar scales of the three plots are not the same whereas that of the horizontal axis are the same. . . . .	73

- 4.22 The cross sectional view of the spatio-temporal amplitude profile in Fig. 4.21b along a)  $t = 0$  and b)  $x = 0$  together with the corresponding result obtained using the conventional ultrashort pulse propagation method based on the temporal FT. The numerical error  $\Delta|E(x, t)| = |E(x, t)|_{GPBD} - |E(x, t)|_{FFT}$  for the amplitude profiles shown in (a) and (b) are plotted in (c) and (d) respectively. . . . . 74
- 4.23 a)The spectral phase of the given pulse together with the quadratic spectral phases (shown for only two sampling points , at  $2(1/fs)$  and  $2.7(1/fs)$  , for clarity), b)the group delays and the group delay dispersion of the GPs used for the decomposition. Every black dot corresponds to the center of one GP used. . . . . 75
- 4.24 The spectral a) amplitude and b) phase profiles of the given pulse together with that obtained by superposition of the elementary GPs each with different delay and chirp parameters. The residual error of the spectral c) amplitude and d) phase after GPD. . . . . 75
- 4.25 The temporal amplitude profile of the given pulse with large TOD computed by superposition of the elementary GPs. . . . . 76
- 4.26 The same as in Fig. 4.24 but now computed using zero initial delay and chirp parameters of the individual GPs. . . . . 76
- 4.27 The spatial amplitude profile of a) the outer sub-field with sharp edge, b) the inner sub-field and c) the total field for plane wave pulse truncated by circular aperture with radius  $r = a$  after propagating for  $t = 600ps$ . 77
- 4.28 The spatial amplitude profile of the converging wave pulse truncated by circular aperture at time a)  $t = -30fs$ , b)  $t = 0fs$  and c)  $t = 30fs$ . The arrival time of the pulse peak at the focal plane is taken as  $t = 0$ . 78
- 4.29 The same as in Fig. Fig. 4.28 but showing the central part between the dotted lines in zoomed version by using equal scaling for both axis to clearly show the change in the shape of the boundary wave pulse as it propagates. . . . . 79
- 4.30 a) The 2D system layout, and b) the geometric pulse and phase front in the focal region of the Geltech Aspheric Lens used for focusing ultrashort pulse. . . . . 79



4.31	The $y - z$ cross-sectional view of the spatial intensity profile of the ultrashort pulse near the focal plane of the aspheric lens for different times. The time is chosen in such a way that $t = 0$ refers to the pulse intensity maximum reaches at the focus. . . . .	80
4.32	a) The $y$ cross-section of the pulse intensity profile at the focal plane computed using the GPBD and the FT based methods. b) the difference in the pulse intensities obtained using the two methods. . . . .	81
4.33	The spatial profile of the pulse in the focal region of the lens at $t = -200fs$ for an input plane wave pulse truncated by a circular aperture. . . . .	81
4.34	The 2D layout of an axicon used to generate a Bessel-X pulse (different scales are used for $z$ and $y$ -axis to make the rays more visible). The dotted lines indicate the locations of the transversal planes where the pulse intensities are computed. . . . .	82
4.35	The $y - t$ cross-section of the amplitude profile of the Bessel-X pulse on the transversal planes which are located at a) $55mm$ , b) $95mm$ and c) $135mm$ from the axicon. The white dotted lines indicate the location of $t = 0$ and the red dotted lines indicate the location of the pulse peak. . . . .	83
4.36	a) The 1D cross section of the Bessel X-pulse on the transversal plane located at $z = 95mm$ from the axicon computed by using the GPBD method together with that obtained using the analytical propagation formula. b) The numerical difference of the magnitudes of the amplitude profiles shown in (a). . . . .	83
4.37	The temporal cross-sections of the amplitude profiles shown in Fig . 4.35 for the on-axis point. . . . .	84
4.38	System layout and geometrical ray tracing through a single grating system. (Note that the coordinate origin is not at the center of the grating.) . . . . .	84
4.39	The spatial profile of the pulse at the moment when its peak arrives a transversal plane located at a) $z = 60mm$ and c) $z = 110mm$ . The spatio-spectral profiles on the $y$ -cross section of the two transversal planes are shown in (b) and (d) respectively. . . . .	85
4.40	The schematic diagram of a Treacy compressor. . . . .	86

4.41	The spectral a) amplitude and b) phase of the chirped input pulse together with that obtained after the GPBD. The residual error of the spectral c) amplitude and d) phase of the decomposition. For results in (b) and (d) only small frequency range near the central frequency is shown for clear comparison. . . . .	87
4.42	The spatio-temporal amplitude profile of a) the chirped input pulse b) the y-cross section and c) the x-cross section of the output pulse after a single pass through the Treacy compressor. The temporal amplitude profile at the center ( $x = y = 0$ ) of d) the input and e) the output pulse.	88
4.43	The same as in Fig. 4.42 but now computed for double pass usage of the Treacy compressor . . . . .	89
4.44	The schematic diagram of the Martinez stretcher. . . . .	90
4.45	The system layout of the stretcher-compressor setup. The roof mirror reflectors are used to reflect the pulse back in a different path to enable separation of the input and output beams. Labels: G (grating), L (lens), M (plane mirror). . . . .	91
4.46	a) The GDD and b) the TOD of the Treacy compressor computed using geometrical ray tracing together with the result computed using analytical formula [4, 99]. The numerical difference between the two results is shown in (c) and (d) respectively. . . . .	91
4.47	The same as in Fig. 4.46 but now computed for the Martinez grating pair with internal dispersion less telescope. . . . .	92
4.48	The spatio-temporal profile of the ultrashort pulse a) at the input plane, b) after the double pass through the stretcher and c) after the complete stretcher-compressor setup. The temporal amplitude profiles at the center ( $x=y=0$ ) at d) the input and the output planes and e) the intermediate plane after double pass through the stretcher. . . . .	93
4.49	a) The GDD and b) the TOD of the complete CPA setup with real refractive lenses. . . . .	94
4.50	The spatio-temporal amplitude profiles of a) the input pulse b) the y-cross-section and c) the x-cross-section of the output pulse after the complete CPA setup with real lens. The comparison of d) the spatial and d) the temporal cross-sections of the input and output pulse amplitude profiles. . . . .	94

---

D.1	A GB truncated in both x- and y- dimensions. . . . .	121
E.1	The dot diagram of 200 sampling points inside a unit circle distributed using a) the cartesian, b) the hexapolar, and c) the Fibonacci sampling scheme. . . . .	125

## List of Abbreviations

<b>Abbreviation</b>	<b>Description</b>
FT	Fourier transform
GB(s)	Gaussian Beam(s)
GBD	Gaussian Beam Decomposition
GDD	Group delay dispersion
GP(s)	Gaussian Pulse(s)
GPD	Gaussian Pulse Decomposition
GPB(s)	Gaussian Pulsed Beam(s)
GPBD	Gaussian Pulsed Beam Decomposition
IFT	Inverse Fourier transform
RMS	Root mean square
TOD	Third order dispersion

## Acknowledgment

First and foremost, I would like to express my deep sense of gratitude and respect to my supervisor Prof. Dr. Herbert Gross. Since I have joined his research group in 2013, as a master student, he was consistently providing me his excellent guidance, endless support, and sharing his years of expertise. I am very grateful for his trust and confidence in me and for his incredible ability to motivate, inspire, and think positively. I am very much grateful to have studied under him, and I could not have wished for a better supervisor for my Ph.D. study.

I would also like to thank my colleagues in the Optical System Design group for being very friendly and kind to me. They have created a happy atmosphere and a great working environment the entire time. I greatly appreciate the colleagues who have offered constructive comments and suggestions during our discussions over the years.

Besides, I am grateful to all my other friends in Jena. When I have faced any troubles and worries, they were always there to listen and encourage me. They have helped me get used to the new living environment in Germany and survive all the stress from those years during my study.

Finally, my deepest gratitude goes to my families and relatives, back in Ethiopia, for their continued encouragement during my entire stay here. Although they were thousands of kilometers away, their enormous love and unconditional support was always present and felt. Without their help and encouragement, I would not have finished this work.

This page is left blank intentionally.

## Ehrenwörtliche Erklärung

Ich erkläre hiermit ehrenwörtlich, dass ich die vorliegende Arbeit selbständig, ohne unzulässige Hilfe Dritter und ohne Benutzung anderer als der angegebenen Hilfsmittel und Literatur angefertigt habe. Die aus anderen Quellen direkt oder indirekt übernommenen Daten und Konzepte sind unter Angabe der Quelle gekennzeichnet.

Bei der Auswahl und Auswertung folgenden Materials haben mir die nachstehend aufgeführten Personen in der jeweils beschriebenen Weise ~~entgeltlich~~/unentgeltlich geholfen:

- Herbert Gross, Betreuer.

Weitere Personen waren an der inhaltlich-materiellen Erstellung der vorliegenden Arbeit nicht beteiligt. Insbesondere habe ich hierfür nicht die entgeltliche Hilfe von Vermittlungs- bzw. Beratungsdiensten (Promotionsberater oder andere Personen) in Anspruch genommen. Niemand hat von mir unmittelbar oder mittelbar geldwerte Leistungen für Arbeiten erhalten, die im Zusammenhang mit dem Inhalt der vorgelegten Dissertation stehen.

Die Arbeit wurde bisher weder im In- noch im Ausland in gleicher oder ähnlicher Form einer anderen Prüfungsbehörde vorgelegt. Die geltende Promotionsordnung der Physikalisch-Astronomischen Fakultät ist mir bekannt.

Ich versichere ehrenwörtlich, dass ich nach bestem Wissen die reine Wahrheit gesagt und nichts verschwiegen habe

Jena,  
Ort, Datum

Unterschrift d. Verfassers

This page is left blank intentionally.



## Curriculum Vitae

**Name :** Worku, Norman Girma  
**Date of birth :** 12.10.1989 in Waka, Ethiopia  
**Sex :** Male  
**Nationality :** Ethiopian  
**Education :**  
10.2012 - 04.2015 M.Sc. in Photonics  
Friedrich-Schiller University of Jena, Germany  
10.2006 - 07.2010 B.Sc. in Electrical Engineering  
Hawassa University, Ethiopia  
09.2004 - 06.2006 College preparatory school  
Waka College Preparatory School, Ethiopia  
10.2000 - 07.2004 Secondary school  
Waka Secondary School, Ethiopia  
10.1994 - 07.2000 Primary school  
Waka Model Primary School, Ethiopia, Ethiopia  
**Working experience :**  
06.2015 - Now Research assistant and doctoral candidate  
Group: Optical System Design (Prof. Dr. Herbert  
Gross)  
Institute of Applied Physics  
Friedrich-Schiller University of Jena, Germany

Jena, 25.06.2020

Signature

This page is left blank intentionally.

# Publications

## Journal articles

- **Worku, N.G.**, and Gross, H. "Application of Gaussian pulsed beam decomposition in modeling optical systems with diffraction grating." JOSA A 37.5 (2020): 797-806.
- **Worku, N.G.**, and Gross, H. "Spatially truncated Gaussian pulsed beam and its application in modeling diffraction of ultrashort pulses from hard apertures." JOSA A 37.2 (2020): 317-326.
- **Worku, N.G.**, and Gross, H. "Gaussian pulsed beam decomposition for propagation of ultrashort pulses through optical systems." JOSA A 37.1 (2020): 98-107.
- **Worku, N.G.**, and Gross, H. "Propagation of truncated Gaussian beams and their application in modeling sharp-edge diffraction." JOSA A 36.5 (2019): 859-868.
- **Worku, N.G.**, Hambach,R., and Gross, H. "Decomposition of a field with smooth wavefront into a set of Gaussian beams with non-zero curvatures." JOSA A 35.7 (2018): 1091-1102.

## Journal articles not directly related to this thesis

- Bösel, C., **Worku, N.G.**, and Gross, H. "Ray-mapping approach in double freeform surface design for collimated beam shaping beyond the paraxial approximation." Applied optics 56.13 (2017): 3679-3688.
- Stock, J., **Worku, N.G.**, and Gross,H. "Coherent field propagation between tilted planes." JOSA A 34.10 (2017): 1849-1855.

## Conference proceeding and talks

- **Worku, N.G.**, and Gross, H. "Vectorial field propagation through high NA objectives using polarized Gaussian beam decomposition.", SPIE Proceedings Vol. 10347, p. 103470W, Aug 2017, San Diego, USA.
- **Worku, N.G.**, and Gross, H. "Diffraction propagation of a field with smooth wavefront using modified Gaussian beam decomposition." Oral presentation, DoK-DoK, 7<sup>th</sup> doctoral conference in optics, Sep 2018, Friedrichroda, Germany.